Growth and characterization of $Cu_2BaSn(S_{1-x}Se_x)_4$ thin films for solar cell application

A Thesis

Submitted by
Jyoti
(Regd. No. 901812001)

Under the supervision of
Dr. Bhaskar Chandra Mohanty
(Professor)

For the award of the degree
of
Doctor of Philosophy

THAPAR INSTITUTE
OF ENGINEERING & TECHNOLOGY
(Deemed to be University)

Department of Physics and Materials Science
Thapar Institute of Engineering & Technology, Patiala 147004, India
April 2026

DEDICATED

TO

MY LOVING GRAND PARENTS AND PARENTS

THESIS CERTIFICATE

I hereby certify that work presented in this thesis entitled “**Growth and characterization of $Cu_2BaSn(S_{1-x}Se_x)_4$ thin films for solar cell application**” in partial fulfilment of the requirement of the award of degree of DOCTOR OF PHILOSOPHY in the Department of Physics and Materials Science, Thapar Institute of Engineering and Technology, Patiala is an authentic record of my own work carried out under supervision of Dr. Bhaskar Chandra Mohanty. The matter embodied in this thesis has not been submitted in part or full to any other university or institute for the award of any degree.

Jyoti

Jyoti

This is to certify that the above statement made by the candidate is true to the best of my knowledge.

Research Guide

BMohanty

(Dr. Bhaskar Chandra Mohanty)
Professor
Department of Physics and Material Sciences
Thapar Institute of Engineering and Technology
Patiala

ACKNOWLEDGEMENT

Prima facie, I am grateful to the God for the good health and wellbeing that were necessary to complete this thesis.

I would like to express my sincere gratitude to my advisor, Prof. Bhaskar Chandra Mohanty for introducing me to the diverse and dynamic field of photovoltaics. Experimenting with this material calls for multidisciplinary approach, combining chemistry, physics and material science. I am grateful for his support and assistance during my thesis.

Furthermore, I would like to thank, Dr. Bhupendra N. Chudasama, Dr. Loveleen Kaur Brar, Dr. Puneet Sharma and Dr. Bonamali Pal for being part of my thesis committee, as well as for all the fruitful discussions.

I express my gratitude to Dr. Bhupendra N. Chudasama, Professor and Head of Department of physics and Materials Science.

I am very grateful to Dr. Bhupendra N. Chudasama from Nano medicine Lab, School of Physics and Material Sciences for allowing me to use their equipment for optical measurements and Dr. Poonam Uniyal and Dr. D. P. Singh for letting me use their equipment for electrical measurements.

I am especially grateful to my laboratory colleagues, Dr. Indu Gupta, Dr Kaushlendra Pandey, Dr. Neetu Bansal, Samarjit Mandal, Neha Saini and Ritika Sharma for their support and assistance to my work.

I thank my friends Dr. Taranveer Kaur, Dr. Vimi Dua and all other friends for their great support throughout the tough times, for being so positive, supportive and helpful.

Lastly, I offer sincere thanks to parents (Shri. Parmjit Singh and Smt. Urmila Devi), my husband, Abhinav, my son Manraj Singh and other family members and relatives for their love, motivation, encouragement, and unlimited patience throughout my education.

Jyoti

ABSTRACT

In recent years, Cu_2ZnSnS_4 (CZTS) has been focus of study as a promising absorber layer in thin film solar cells due to its high absorption coefficient, appropriate bandgap, and environment-friendly earth-abundant constituents. Despite global efforts the efficiency of the CZTS based devices is stagnated at 12.6% since 2014. This stagnated performance is attributed to a large V_{oc} deficit caused by recombinations due to charged point defects and defect clusters. The dominant defect in CZTS is Cu_{Zn} antisite defect, formed due to similar ionic radii of Cu and Zn (0.74 Å) ions. A potential approach to curb the formation of these antisite defects is isoelectronic substitution of one of the cation by cation of larger or smaller ionic radii. Among various substitutions proposed in literature (e.g. Ag for Cu, Cd for Zn, Ge for Sn, etc.), substitution of Zn by Ba is considered to significantly change the cationic disorder in CZTS. In Cu_2BaSnS_4 (CBTS), Ba has a larger ionic radii (1.56 Å) and the dominant defect in CBTS is V_{Cu} which results in p-type conductivity of CBTS, similar to the more matured absorber material $CuInGaS_2$. Owing to the large size difference, significant structural changes in CBTS, and hence, opto-electronic properties compared to CZTS are expected. This work deals with the growth and characterization of CBTS and Se-alloyed CBTS (CBTSSe) thin films.

In view of the differences in the optical and electrical properties of CBTS films with those of CZTS, we have numerically investigated and compared the performance of both devices using the SCAPS software. Simulations were carried out by considering the typical solar cell structure of glass/Mo/CZTS/CdS/i-ZnO/ITO. For a more realistic approach, a thin MoS_2 layer is considered between Mo and CZTS. Simulations revealed an efficiency of about 17.68%, which is much higher than the experimentally obtained record efficiency of 11%. This suggest that the simulation should include an appropriate amount of defects in the bulk and at interfaces (i.e., back interface MoS_2/CZTS and front interface CZTS/CdS). The experimental champion device parameters could be successfully simulated only when bulk defect density of 5.5×10^{15} cm^{-3}, defect density of $\sim 1 \times 10^{15}$ cm^{-2} and $\sim 1 \times 10^{14}$ cm^{-2} at back and front interfaces was introduced. A possible route – by inserting a back surface field (BSF) layer - to improve the efficiency of the devices with CBTS films having these amounts of defect density has been demonstrated. It is shown that the CZTS solar cell efficiency can be increased up to 14.7% and 15.7% by optimizing Cu_2O and SnS films as BSF layers, respectively. On the other hand, for CBTS films with similar defect density that resulted 11% efficiency for CZTS (experimentally obtained champion cell) simulations yielded an efficiency of only 4.55%. This is because of larger bandgap (2.0 eV for CBTS vs 1.5 eV for CZTS) and different nature of defects.

Performance of the CBTS devices could be increased to 6.9% (reported experimental value) only when the defect densities were considerably reduced (interface defect density $N_{MoS2/CBTS} \sim 10^{15}$ cm^{-2}, $N_{CdS/CBTS} \sim 10^{10}$ cm^{-2} and bulk density $N_{CBTS} \sim 10^{14}$ cm^{-3}). The results suggest that the performance improvement of CBTS solar cells is more challenging than that for CZTS cells and hence, experimental conditions for the fabrication of CBTS films are expected to be more stringent.

The CBTS films were synthesized by a solution based approach. A precursor film was prepared by spin coating of a non-toxic 2-methoxy ethanol based molecular precursor solution and was heat treated in presence of sulphur powder to obtain the eventual film. Since the formation of the secondary phases must be suppressed during the growth of the films as they degrade the performance of the solar cells, the process parameters were carefully optimized and the reaction pathway leading to the formation of single phase CBTS was established. We have systematically varied the molar concentration ratio in the solution and the sulfurization parameters (temperature, dwelling time and sulphur amount) and studied the impact thereof on the evolution of single phase CBTS. It was found that ideal molar concentration ratio [Ba]/[Sn] =1.0 always yielded secondary phases in spite of a large variation in the sulfurization parameters. Single phase CBTS thin films are obtained only for [Ba]/[Sn] = 1.4 in the precursor solution and sulfurization at 575 °C for 45 min with 1.0 g of powder S. UV–visible and room temperature PL measurements revealed a band gap of ~2.0 eV for these films. A symmetric PL peaks suggests reduced cationic disorder in the films compared to CZTS. The films showed white light sensitivity (~30%) for illumination of 24 mW/cm^2. Detailed electrical and electro-impedance measurements showed p-type conductivity with a carrier concentration of 1.7×10^{14} cm^{-3} for the films.

The CBTSSe films were obtained by heat treating the as-prepared precursor films in the presence of 1.0 g of sulphur (that yielded CBTS films) and varying amounts of selenium. It was found that the process parameters that produced CBTS films yielded various secondary phases that necessitated further optimization of the parameters including Ba/Sn ratio in the precursor solution, sulpho-selenization temperature and dwelling time, etc. Phase pure CBTSSe thin films were obtained for Ba/Sn=1.7 and annealing at 550 °C for 45 min with 1.0 g of S and 0.1 g of Se. By placing varying amounts of Se in the furnace during the sulpho-selenization process step, the concentration of Se in the films was systematically varied and the impact thereof was investigated. It was observed that by varying the Se amount from 0.1 to 0.4 g during sulpho-selenization, the Se/(Se+S) ratio in the resulted films increased from 0.05 to 0.22. With increase in the Se amount in the films, the bandgap of the films decreased

gradually from 1.93 to 1.55 eV. The electro-impedance spectroscopy measurements on the film grown with 0.4 g of Se during sulpho-selenization revealed its p-type conductivity with an acceptor concentration of 1.58×10^{17} cm^{-3}. The results indicate that these films can be potentially used as photocathode for hydrogen evolution.

CONTENTS

CHAPTER 3 Analysis of CZTS and CBTS thin film solar cells by numerical simulations

CHAPTER 4 Growth and characterization of Cu_2BaSnS_4 (CBTS) thin films

CHAPTER 5 Growth and characterization of Se-alloyed Cu_2BaSnS_4 (CBTSSe) thin films

LIST OF TABLES

LIST OF FIGURES

LIST OF SYMBOLS & ABBREVIATIONS USED

WMO	World Meteorological Organization
UN	United Nation
CZTS	Cu_2ZnSnS_4
CZTSSe	Se-alloyed Cu_2ZnSnS_4
CBTS	Cu_2BaSnS_4
CBTSSe	Se-alloyed Cu_2BaSnS_4
CdTe	Cadmium Telluride
CIGS	$CuInGaS_2$
DMSO	Dimethyl Sulphoxide
FTO	Flourine doped Tin Oxide
V_{oc}	Open circuit voltage
E_g	Band Gap
J_{sc}	Short-Circuit current density
η	Efficiency
EQE	External quantum efficiency
FF	Fill Factor
SQ	Shockley-Queisser
SCAPS-1D	one dimensional solar cell capacitance simulator
BSF	back surface field
SEM	Scanning electron microscope
XRD	X-ray diffraction
TGA	Thermogravimetric analysis
EIS	Electrochemical impedance spectroscopy
N_{i1}	defect density at MoS_2/CZTS interface
N_{i2}	defect density at CZTS/CdS interface
N_b	Bulk defect density
N_{A+}	acceptor concentration
χ	Electron affinity
VBO	Valence band offset
CBO	Conduction band offset
α	absorption coefficient

LIST OF PUBLICATIONS

1. Jyoti and BC Mohanty, Improving performance of Cu_2ZnSnS_4 solar cell via back contact interface engineering, ***Solar Energy 230 (2021) 986–995.***
2. Jyoti and BC Mohanty, Revealing performance limiting factors in Cu_2BaSnS_4 thin film solar cells, ***Optik 295 (2023) 171504***.
3. Jyoti and BC Mohanty, Barium concentration controlled phase evolution in molecular solution processing of Cu_2BaSnS_4 thin films for solar cells with improved optical and electrical properties, ***Journal of Alloys and Compounds 986 (2024) 174105.***
4. Kaushlendra Pandey, Jyoti, Indu Gupta, BC Mohanty, Ramalinga Viswanathan Mangalaraja, and Arunachalam Arulra, Substrate temperature-driven growth of phase-pure Cu_2ZnSnS_4 thin films by RF magnetron sputtering using compound target for solar cell applications, ***J Mater Sci: Mater Electron (2026) 37:661***.*
5. Jyoti and BC Mohanty, Overcoming the challenges of phase formation and bandgap tuning in solution processed $Cu_2BaSn(S,Se)_4$ thin films with favourable band alignment for H_2 evolution (Accepted in ***The Journal of Physical Chemistry C***)

*** not part of this thesis**

LIST OF CONFERENCE PRESENTATIONS

1. Jyoti, BC Mohanty, Impact of p+ back surface field (BSF) layer thickness on the performance of Cu_2ZnSnS_4 thin film solar cells, Poster presented at ***FMT 2020 - Frontiers in Manufacturing Technology***, KIIT University, Odisha, India, October 13-14, 2020.
2. Jyoti, BC Mohanty, Formation of Cu_2BaSnS_4 thin films for thin film solar cell application, Poster presented at ***IC-AMDFA 2021 - International Conference in Advanced Materials and Devices for Futuristic Applications***, Chandigarh University, Chandigarh, November 23-24, 2021.
3. Jyoti, BC Mohanty, Role of Ba composition in precursor solution while fabricating Cu_2BaSnS_4 thin films by solution approach, Poster presented at ***ICAMMM 2022 - International Conference on Advanced Materials, Metallurgy & Manufacturing***, PEC Chandigarh, November 1-2, 2022.
4. Jyoti, BC Mohanty, Formation of Cu_2BaSnS_4 thin films for thin film solar cell application, Poster presented at ***I-MAT 24 Conference on Innovations in Materials Science & Workshop on Characterization Techniques***, IIT Roorkee, March 24–27, 2024.
5. Attended "***A Two day workshop on Structural Analysis (X-Ray Diffraction, Rietveld Refinement, HRTEM & SAED-2025***" organised by Centre for Nanoscience and nanotechnology, International Research centre & Advanced Characterization Facility, Satyabhama institute of science and technology, Chennai. (Online mode)

CHAPTER 1
Introduction

1.1 Introduction

In recent times, the global energy demand has increased significantly due to the urbanization of human lifestyles, technology adaptation, and a rising population. So far, most of this energy demand has been fulfilled from fossil fuels such as coal, and gas. However, utilization of these fossil fuels has caused serious environment issues in the form of emission of greenhouse gases. According to a recent report by the World Meteorological Organization (WMO), consumption of the fossil fuel at the current level may cause to raise the temperature that may breach the UN's resolution to limit it to 1.5 °C (un.org). In the quest for energy sources that can meet the increasing global energy demand and are clean and sustainable, photovoltaic technology offers potential cost-effective options. Solar panels made of highly pure crystalline silicon (1st generation solar cells) are the most popular ones in the solar cell market. However, the high cost involved in processing to achieve such highly pure crystalline silicon has been a disadvantage. The 2nd - generation solar cells employ absorber layers in the form of thin films of only 1-2 µm thickness, thereby reducing the material cost significantly. The current global research focus in photovoltaics has been to develop thin absorber layers with suitable properties using cost-effective synthesis routes.

1.2 Cu_2ZnSnS_4 (CZTS) based thin films

Among the thin film solar cells available, CIGS ($CuInGaS_2$) and CdTe-based solar cells have been very popular, with demonstrated efficiencies better than 20%. However, the use of In and Ga (scarce elements) in CIGS and Cd (a toxic element) in CdTe has limited their global acceptability as a possible energy solution. In the last two decades, the quaternary semiconductor Cu_2ZnSnS_4 (CZTS) and related alloys have been studied as an alternate absorber candidates due to its abundant in earth, benign, and economical constituents in addition to high coefficient of absorption $\sim10^4$ cm^{-1} and a tuneable bandgap (from 1 to 1.5 eV due to Se alloying) (Wei et al., 2024; Mitzi et al., 2011; Walsh et al., 2012). The intensified research on CZTS and Se-alloyed CZTS (CZTSSe) has led to rapid progress in conversion efficiency from ~6.8% in 2008 to beyond 12% in 2014 (Wang et al., 2014 a). Since then, however, the efficiency of CZTSSe-based solar cells is pinned at 12.6%, despite concerted global research efforts. For the pure sulphide analogue, i.e., CZTS, the record best efficiency is only 11% (Yan et al., 2018). The reported efficiencies, nevertheless, are inferior to those desired for scalable production at an industrial level. The difference between the historical evolution of power conversion efficiencies of CZTS and CIGS over certain periods of time is quite large, considering that their energy bandgap is very similar. Therefore, it has been of great interest for researchers to address the reasons behind the low performance of CZTS as compared to CIGS.

The various proposed reasons for the inferior performance of CZTSSe solar cells as compared to CIGS solar cells converge on the low open circuit voltage (V_{oc}) deficit (i.e., $E_g/q - V_{oc}$), which is less than 60% of the maximum V_{OC} predicted from the Shockley-Queisser limit (Polizzotti et al., 2013). The presence of point defects, clusters of these point defects (cationic disordering), and associated band tailing in the CZTS(Se) films has been referred to as a plausible mechanism of this V_{oc} deficit (Chen et al., 2010). Among various possible point defects in CZTS (Cu_{Zn}, Sn_{Zn}, Zn_{Cu}, V_{Cu}+Zn_{Cu}, Cu_{Zn}+Zn_{Cu}, etc), Cu_{Zn} is the most dominating defect in CZTS. Cu_{Zn} antisite defect is easily formed due to small ionic size difference in Cu^{+1} and Zn^{+2}. The presence of such defects (and the defect pairs) induces the energy level formation in the electronic bandgap from the localization of electron wave functions in the disordered lattice. For a higher lattice disorder (due to high density of defects/ defect clusters), the tail states at the valence band top and the conduction band bottom, stretch into the bands, causing narrowing of the bandgap (Nagoya et al., 2010; Gokmen et al., 2013; Miller et al., 2012; Islam et al., 2015). While the processing of CZTS films can be manipulated to reduce some other antisite defects (for example, growing films in typical Cu-poor and Zn-rich conditions can reduce Cu_{Sn} and Sn_{Zn}, which otherwise behave as deep traps within the electronic bandgap (Kobayashi et al., 2005; Todorov et al., 2010; Tanaka et al., 2009)), it has been very difficult to reliably control the Cu-Zn cationic disorder.

1.2.1 Cation Substitution in CZTS(Se) Thin films

More recently, several approaches have been reported to improve the cationic ordering, and hence, to mitigate the V_{oc} deficit. For instance, annealing for several hours after the heat treatment in a chalcogen environment has been shown to partially reduce the cationic disorder. However, isoelectronic cation substitution in CZTSSe by larger or smaller-sized cations is considered a promising technique to suppress Cu_{Zn} antisite defects (Su et al., 2015; Kumar et al., 2018). In the past few years, there have been attempts to substitute Cu (by Ag, Li) or Zn (by Cd or Ba) (Kumar et al., 2017) with cations having larger or smaller ionic radius. Table 1.1 highlights a few studies based on isoelectronic substitutions in CZTSSe thin films to improve device efficiency. For instance, replacing Cu^{+} (0.74Å) by Ag^{+} (1.14 Å) can effectively reduce the antisite defect formation. However, the type of conductivity is reportedly changed (i.e., from p to n-type) in $Cu_{1-x}Ag_x ZnSnS_4$ (ACZTS) when the x value exceeds 0.6. Therefore, it is very critical to control cation stoichiometry in ACZTS to get optimum device performance without affecting the conductivity type (Liang et al., 2018). On the other hand, Cd (0.92 Å) with a greater ionic radius can also help to avoid the formation of antisite defects (Yan et al., 2017). However, Cd, due to its high toxicity, poses environmental threats. In further attempts to reduce cation disordering in CZTSSe, Xiao et al. presented the distant ion mutation concept to use Ba (Group II), which lies far from elements of Group I, Cu and Group IV, Sn in the periodic table, to substitute Zn. This could be a promising substitution due to the large radius of Ba^{2+} (1.56 Å) and the high difference in electronic properties of Ba from Cu and Sn (Xiao et al., 2017). Interestingly, many isoelectronic cation substitutions with larger/smaller ionic radius (for example, Ag for Cu, Ge for Sn, Cd for Zn, etc.) deal with materials inherently in the zinc blende-derived kesterite phase, where tetrahedral coordination forms the structural motif. On the other hand, Ba substitution in the place of Zn (i.e., in the compound Cu_2BaSnS_4 (CBTS)) offers a different coordination environment that may have wide-ranging implications on film properties. This warrants further research and forms the basis of this thesis.

Table 1.1: Highlights of studies on cation substitution in CZTS(Se) thin films.

Substitution	**Deposition technique**	**Cell Parameters/Remarks**	**Reference**
Ag in CZTS	Solution method	Solar cell with total area efficiency η:14.1%	Zhou et al., 2023
Ag in CZTS	Sol-gel method	Optimal photodetection for 4% Ag-doping in CZTS	Kangsabanik et al., 2025
Ag in CZTS	thermal co-evaporation	η: 10.2%, V_{oc}: 422.5 mV, J_{sc}: 38.4 mA/cm^2	Chagarov et al., 2016
Ag in CZTSSe	Solution method	η: 10.2%, V_{oc}: 448 mV, J_{sc}: 35.1 mA/cm^2	Yafang et al., 2017
Ag in CZTSSe	Solution method	η: 7.12%, V_{oc}: 373 mV, J_{sc}: 34.1 mA/cm^2	Zhao et al.,2017
Ag in CZTS	Spray pyrolysis	η: 7.14%, V_{oc}: 669 mV, J_{sc}: 18.5 mA/cm^2	Nguyen et al., 2018
Ag in CZTS	Co evaporation	η: 5.2%, V_{oc} :504 mV, J_{sc}: 21 mA/cm^2	Gershon et al., 2016
Ba in CZTSSe	Sputtering method	η: 1.57%, V_{oc}: 0.613 V, J_{sc}: 6.78 mA/cm^2	Je et al., 2016
Ba in CZTS	Sputtering method	η: 1.62%, V_{oc}: 713 mV, J_{sc}: 4.11 mA/cm^2	Shin et al., 2016
Ba in CZTS	Sputtering method	η: 2.03%, V_{oc}: 0.93 V, J_{sc}: 5.08 mA/cm^2	Ge et al., 2017 b
Ba in CZTSSe	Sputtering method	η: 5.2%, V_{oc}: 611 mV, J_{sc}: 17.4 mA/cm^2	Shin et al., 2017
Cu_2-II-Sn-VI_4 II = Ba, Sr, VI = S, Se	Theoretical Calculation	Cation-on-cation antisite defects do not form easily.	Hong et al., 2016

Ba in CZTSe	Theoretical study	Due to high ionicity, Ba-related defects create only shallow defect levels. Hence, CBTSe solar cells may have smaller V_{oc} deficits.	Xiao et al., 2017
Cd in CZTS	Solution method	Cd-doped CZTS with a bandgap of 1.56 eV and low band tailing is fabricated	Gupta et al., 2023
Cd in CZTS	Solution method	η: 1.2%, V_{oc}: 333.2 mV, J_{sc}: 7.95 mA/cm^2	Xiao et al., 2013
Cd in CZTS	Solution method	η: 8.11%, V_{oc}: 460 mV, J_{sc}: 29.66 mA/cm^2	Fu et al., 2016
Cd in CZTS	Chemical Bath deposition	η: 11.5%, V_{oc}: 651 mV, J_{sc}: 26.7 mA/cm^2	Yan et al., 2017
Ge in CZTS	Solution method	η: 5.12%, V_{oc}: 599.9 mV, J_{sc}: 21.8 mA/cm^2	Zhang et al., 2024
Ge in CZTSe	e-beam evaporation	η: 6%, V_{oc}: 487 mV, J_{sc}: 28.1 mA/cm^2	Scaffidi et al., 2023
Ge in CZTSe	Co evaporation	η: 10.03%, V_{oc}: 0.543 V, J_{sc}: 29.5 mA/cm^2	Kim et al., 2016
Ge in CZTSe	Solution method	η: 8.4%, V_{oc}: 0.464 V, J_{sc}: 29.2 mA/cm^2	Guo et al., 2012
Na	Solution method	η: 8.3%, V_{oc}: 450 m V, J_{sc}: 30.77 mA/cm^2	Werner et al., 2015
Na:Sb-doping	Solution method	η: 5.7%, V_{oc}: 610 mV, J_{sc}: 14.9 mA/cm^2	Tiwari et al., 2016
Na,Li,Rb-substitution	Electrostatic Spray Assisted Vapor Deposition	η For Rb:6.35%, η For Na:6.2%, η For Li:6.0%	Altamura et al., 2016 (b)
K-substitution	Solution method	η: 3.34%, V_{oc}: 498 mV, J_{sc} : 12.18 mA/cm^2	Tong et al., 2014

Li-Substitution	Solution method	η: 11.6%, V_{oc}: 531 mV, J_{sc}: 33.7 mA/cm^2	Vidani et al., 2018
Li-Substitution	Solution method	η: 6.7%, V_{oc}: 459 mV, J_{sc}: 14.9 mA/cm^2	Yanchun et al., 2016
In-Substitution	Co Electroplating	η: 3.4%, V_{oc}: 461.1 mV, J_{sc}: 18.8 mA/cm^2	Ge et al., 2014
Si-doping	Magnetron Sputtering	η: 2.53%, V_{oc}: 0.401 V, J_{sc}: 15.86 mA/cm^2	Guo et al., 2018
Fe-Substitution	successive ionic layer adsorption and reaction	η: 2.95%, V_{oc}: 0.61 V, J_{sc}: 9.3 mA/cm^2	Chatterjee et al., 2017
Mn-Substitution	chemical spray pyrolysis	η: 7.59%, V_{oc}: 0.43 m V, J_{sc}: 28.9 mA/cm^2	Lie et al., 2018
Mg-Substitution	Pulsed layer deposition technique	The bandgap of CZMTS film was found to be 1.4 eV. Mg-substitution enhances the grain size and crystallinity and also increases carrier concentration.	Agawane et al., 2018
Sb-Deposited	Pulsed spray deposition	Antimony salt was used to displace organic ligands from the CZTS nanoparticles surface, Sb enhanced crystal growth.	Carrete et al., 2013

1.3 Literature survey on Cu_2BaSnS_4 (CBTS) and Se-alloyed CBTS (CBTSSe) thin films

Recently, CBTS material has been presented as an effective replacement for CZTS. Using DFT calculations, Hong et al. revealed that CBTS has optical and electrical properties very similar to those of CZTS and hence, it can be used for photovoltaic applications (Hong et al., 2016). Moreover, defect properties of CBTS are more favourable for photovoltaic applications as compared to CZTS. For instance, the dominant defect in CBTS is V_{Cu} instead of the Cu_{Ba} and Ba_{Cu} antisite defects. This is because the formation energy of Cu_{Ba} and Ba_{Cu} is high owing to the large size mismatch between Ba and Cu ions. Xiao et al. also predicted that due to the high ionic nature of Ba, the Ba-related antisite defects create shallow defect levels and do not create high cation-cation disorder (Xiao et al., 2017). They also mentioned that CBTS under Cu-poor and moderate Se conditions will result in p-type conductivity and may reduce V_{oc} deficit as compared to CZTS.

Wang et al. have predicted that CBTS is a highly ionic compound and is not stable thermodynamically in kesterite structure (CZTS has the kesterite structure) as it can easily break down in competing secondary binary or ternary phases. A separate study using DFT has found a chemical region stable for CBTS with trigonal structure without formation of the secondary phases (Wang et al., 2014 b). A schematic diagram of the trigonal structure is shown in Fig. 1.1.

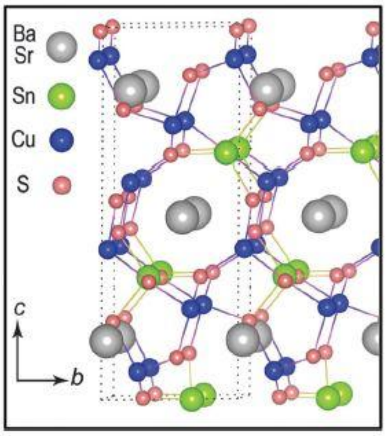

Fig. 1.1: Trigonal Crystal structure of Cu_2BaSnS_4 (Hong et al., 2016)

The reason for the stability of CBTS in a trigonal structure rather than a kesterite structure is primarily due to the large ionic radius of Ba and its electropositive nature and, that leads to non-tetrahedral coordination in the unit cell. In the trigonal structure, each Cu and Sn atom is tetrahedrally coordinated to four Sulfur atoms (as in kesterite and stannite for CZTS) whereas the Ba atom forms an eight-fold coordination with S atoms, which is very different from the Zn in kesterite and stannite coordination environment. This, in turn, is expected to affect the formation of antisite point defects and the corresponding band tailing. For selenium analogue, it has been predicted by Xiao et al. that CBTSe has a larger chemical potential window for stabilization in orthorhombic structure, signifying that single-phase CBTSe can be formed with ease. Also, the CBTSe has a larger chemical potential range as compared to CZTSe, indicating higher thermodynamic stability of CBTSe. This suggests that both CBTS and CBTSe can be potential candidates for harvesting solar energy.

Amidst the venture to obtain the high power conversion efficiencies of kesterite solar cells, replacement of S atoms by Se atoms partially has shown significant improvement in PCE. This has helped to tune the bandgap of the absorber layer and enhance grain size, which minimizes grain boundary recombinations, resulting in better charge transport properties of the absorber layer.

In addition to the importance of appropriate intrinsic properties, high defect resistance, and eventual high device performance, manufacturing cost of the absorber layers should remain cost-competitive. Considering the peculiarities of this class of materials, the deposition processes which are simple and economical, yet yield films of intended properties has been a big challenge. The CBTS-based materials have been prepared by vacuum and non-vacuum-based processes, such as solid-state synthesis (Teske et al., 1976), co-sputtering (Shin et al., 2017; Shin et al., 2016; Ge et al., 2017a; Ge et al., 2017b), and solution processes (McCarthy et al., 2018; Teymur et al., 2018; Chen et al., 2018). While most of the reported efficient CBTS-based solar cell devices and photoelctrochemical cells were manufactured by vacuum requiring sputtering technique, we find only few reports of films prepared by solution methods.

Compared to the vacuum- requiring techniques, solution methods poses less-cost scalable routes of synthesis of ternary semiconducting thin films. However, the challenges such as poor solubility of the Ba salts, requirement of post-deposition annealing to remove organic component/solvent and for grain growth, reactivity of the components, difficulty in control of composition, etc., must be overcome first (Teymur et al., 2018; Teymur et al., 2021; Teymur et al., 2022; Chen et al., 2018). Especially, maintaining the elemental composition in the films, which may differ from that in the precursor solution as a consequence of processing, is critical. The elemental composition in this category of materials impacts phase evolution, antisite defect formation, grain growth, etc., and hence, the output performance (Teymur et al., 2022; Chen et al., 2018). This is supported by the fact that poor Cu and high Zn content composition has always been required for the best-performing CIGS and CZTSSe thin film solar cells. For the CBTS thin films, Chen et al. have found critical dependence of composition (i.e., [Cu]/[Sn] and [Ba]/[Sn]) on obtaining phase pure of the films grown by a molecular solution approach (Chen et al., 2018). They could prepare single phase trigonal Cu_2BaSnS_4 only with [Cu]/[Sn] ~ 1.935 and [Ba]/[Sn] ~1.30. Shin et al. have increased Se content (i.e., $Cu_2BaSnS_{4-x}Se_x$ (x = 3, CBTSSe)) by additional selenization at 570 °C for 5 min after sulfurization. They observed from UV-Vis spectra that CBTSSe exhibits a tunable bandgap from 1.6 to 2 eV (Shin et al., 2017). More recently, Teymur et al. prepared CBTSSe thin films at different [Cu]/([Ba]+[Sn]) ratios by reducing Cu content from its ideal stoichiometric values up to 12% by keeping the

[Ba]/[Sn] ratio of 1.5 in a DMSO-based precursor solution (Teymur et al., 2018). It was observed that the [Cu]/([Ba]+[Sn]) ratio in the films varied from 1.08 to 0.86 when Cu content was reduced from 0% to 12%, whereas [Ba]/[Sn] ratio in films changed from 1.12 to 1.34 as compared to 1.5 in the precursor solution due to loss of BaS_3 during the postdeposition heat treatment with sulfur process. The composition fluctuation affected the phase purity: single-phase CBTSSe was obtained only for moderate Cu-poor precursor solutions (- 4 to -7%). The first report of solution-processed CBTSSe material is based on the spin coating of mixture containing thiol−amine solvent by McCarthy and Brutchey (McCarthy et al., 2018). In their approach, the precursor solution (or the so-called "alkahest solvent") was prepared by dissolution of BaS, Cu_2S and oxide SnO in an ethanedithiol (EDT)-ethylenediamine (EN) at 50˚ C for 11 days, followed by heating using a heat gun. Although phase-pure films were obtained, the films showed a rough structure having voids. However, no device application of these films was reported. Teymur et al. also fabricated CBTSSe absorbers using a solution process by mixing copper acetate, anhydrous SnI_2, barium nitrate, and thiourea in dimethyl sulphoxide (DMSO). The bandgap of the CBTSSe absorber layer was calculated to be 1.68 eV, and a CBTSSe PEC device exhibited a photocurrent of 10 mA/cm^2 (Teymur et al., 2018). Teymur et al. annealed CBTS thin films under Se vapours at 610°C for 5 min and prepared CBTSSe thin films with bandgap of 1.56 eV for x=3 (Teymur et al., 2021). Another report was based on spin coating of films from a molecular precursor solution prepared by dissolving copper acetate, tin chloride, thiourea, and barium acetate in 2-methoxy ethanol. They have obtained 1.72% efficiency with the device configuration of Mo /CBTS/CdS/i-ZnO/ITO. Cui et al. prepared CBTS thin films by solution process and selenized the films at 400°C, and obtained orthorhombic CBTSSe thin films with a good photoresponse behaviour. (Cui et al., 2019).

A trigonal CBTS-based device has been successfully fabricated with the device structure: ITO/i-ZnO/CdS/absorber/Mo/glass, and an efficiency of 1.6% obtained for the first time by Shin et al (Shin et al., 2016). They prepared the films by RF sputtering, followed by a post-sulfurization method. Ge et al. also achieved 1.57% efficiency for $Cu_2BaSn(S_{0.83},Se_{0.17})_4$ solar cell on FTO substrate (Ge et al., 2017a). Later, the same group used oxygenated CdS to act as buffer layer and improved the efficiency to 2.03% with a V_{oc} of 1.1 V (Ge et al., 2017b). From the analysis of their previous report, Shin et al. have prepared $Cu_2BaSnS_{4-x}Se_x$ thin films, and a device efficiency of 5.2% has been obtained (Shin et al., 2017). The relatively low efficiency is possibly due to interface recombination caused by undesirable conduction band offset at the CdS/CBTSSe interface, as revealed from the low EQE response at the short wavelength region. In the photo-electrochemical cell application, the CBTS device shows a 7.8

mA cm^{-2} saturated photocurrent using one sun illumination, which is comparable to Cu_2O photo-electrochemical cells which are the best-performing ones (Ge et al., 2017c). The reported highest efficiency for CBTSSe solar cells, so far is 6.2% by using $Zn_{1-x}Cd_xS$ buffer layer and $Zn_{1-x}Mg_xO$/Al-doped ZnO window layer. The progress in efficiency in CBTS based solar cells has been shown in Table 1.2.

Table 1.2: Progress in efficiency of CBTSSe thin film solar cells over the years.

Year	**η (%)**	**V_{oc} (mV)**	**J_{sc} (mA/cm^2)**	**FF (%)**	**Deposition method**	**Reference**
2016	1.62	713	4.11	55.32	Sputtered	Shin et al., 2016
2016	1.57	613	6.78	37.7	Sputtered	Ge et al., 2016
017	2.03	933	5.08	43	Sputtered	Ge et al., 2017 b
2017	1.6	551	5.95	48.9	Sputtered	Ge et al., 2017 a
2018	1.72	697.8	5.25	46.9	Solution based	Chen et al., 2018
2019	1.21	562	4.17	38	Sputtered	Guo et al., 2019
2020	1.99	510	6.50	60.13	Solution based	Luo et al., 2020
2022	6.17	681	16.16	56.1	Solution based	Teymur et al., 2022

1.4 Numerical study of potential of CBTS thin film solar cells

Numerical study plays a momentous role in understanding the limiting influence of material properties on performance of solar cells. In particular, such studies in the form of simulations can provide insight to the role of defects in performance of the solar cells (i.e., V_{oc}, J_{sc} , FF and η) and hence, are instrumental in designing better solar cells (Basak et al., 2021; Garain et al., 2021; Padhi et al., 2021). According to the Shockley-Queisser (SQ), limit single junction CBTS solar cell can show about 22% efficiency. In contrast, the best conversion efficiency reported for CBTSSe is only 6.2% (the highest efficiency for CBTS is 2.03%). This inferior performance as compared to the SQ limit may be due to possible bulk and interface recombination losses. These recombinations can be controlled by optimizing the bulk material and improving the interface between materials. Although there have been a number of numerical investigation of the CZTS based thin film solar cell, such elucidation of CBTS devices is very limited, although it is of high importance and can assist experimentalists greatly. Khattak et al. have studied numerically the CBTS solar cells and suggested performance enhancement by optimizing thickness and carrier concentration of the CBTS layer (Khattak et al., 2019). Luo et al., optimized parameters of CdS, CBTS and MoS_2 intermediate layer to maximize the efficiency of CBTS solar cells using numerical simulations (Luo et al., 2021). These studies however lacks in discussion about defect tolerance of CBTS as compared to CZTS, which can help to enhance the CBTS solar cells output performance. Therefore, it is of huge interest to examine the resulting scenario in the CBTS-based device with the defect densities, which have yielded the best performance in CZTS devices, and lays the foundation of this work.

In this work, we have used the one dimensional solar cell capacitance simulator SCAPS-1D simulation software for both CZTS and CBTS thin film solar cells. Mainly, we have considered defect densities in the CZTS layer and at front and back interfaces. We have varied the concentration of these defect densities to simulate the performance of the experimentally obtained champion CZTS cells. Further, we used the same value of defect densities to predict the performance of the CBTS solar cell. We show that in a similar device architecture, CBTS has poor defect tolerance compared to CZTS, i.e., for the same level of defect densities, CBTS yields inferior performance than CZTS, and hence, requires more intuitive optimization of parameters.

In literature, it is reported that a thin p+ layer inserted between the absorber layer and the back contact can improve the performance of the cells (Dsouza et al., 2023). The approach of using this layer – known as back surface field (BSF) layer - relies on the creation of a built-in field in the direction same as that in the p-CZTS/n- CdS junction of the solar cell. This electric field, in turn, would provide a conductive path to the holes and act as a potential barrier to the minority carrier electrons, thus minimizing the recombination occurring at the rear contact interface. Since the width of the depletion region, wherein the built-in field is operational, is extended into the regions with lower carrier concentration, an effective BSF layer is required to be heavily doped (p+ type) compared to the CZTS layer. While the approach of using the BSF to manipulate the carrier collection and cell efficiency appears attractive, there are only a couple of studies of the same in the CZTS or CZTSSe-based solar cells (Khattak et al., 2018; Benzetta et al., 2020; Giraldo et al., 2021). Khattak et al. used $Cu_2ZnSnSe_4$ (CZTSe) as a BSF layer in CZTS solar cells and numerically found an increase in efficiency from 9.61 to 12.92% with the introduction of the BSF layer (Khattak et al., 2018). It may be noted that experimentally realizing a junction of phase-pure CZTSe and CZTS will be very challenging due to the inherent material peculiarities of these materials (Just et al., 2016). In a more recent report, Song et al. have shown performance improvement in the CZTSSe solar cells by growing a p-type $MoSe_2$: N_b layer (Song et al., 2020). Nevertheless, a more detailed investigation of the effect of the BSF layer, including the analysis of the band offsets at the BSF layer/CZTS interface (Scheer, 2009), is required. We have numerically investigated the impact of a BSF layer in the form of Cu_2O, which has not been explored in the CZTS solar cells previously. It may be noted that the fabrication of Cu_2O is relatively straightforward and may be easily implemented experimentally (Drobny and Pulfrey, 1979; Herion et al., 1980; Golden et al., 1996).

1.5 Motivation and Objectives

Discussions on the preceding sections suggest that the photovoltaic performance of the CBTS based solar cells has been inferior compared to the CZTS devices, although significant reduction in antisite defects has been theoretically predicted. The potential of these thin films has not been fully brought forward because of the inherent material peculiarities and challenges in fabrication of single-phase thin films with appropriate properties. Till date, only a handful of results with the highest efficiency of just above 6.2% have been achieved, suggesting a larger scope of improvement. The solution approach - which otherwise is considered as the most cost-effective approach for scalable production of thin films - has not been explored much. In particular, understanding the process parameter dependent composition, phase formation and evolution of properties that forms a critical part in designing the CBTS thin film deposition route is far from complete. This work give out a detailed examination of growth mechanism of phase pure CBTS(Se) thin films by a molecular precursor solution approach using 2-methoxy ethanol based precursor solutions of commonly available salts of $(CH_3COO)_2Cu$, $SnCl_2.2\ H_2O$, $(CH_3COO)_2Ba$ and thiourea. We show how by intuitively optimizing the composition ratio in the cationic solution and the sulfurization/selenization ambience single-phase CBTS(Se) films can be obtained. In particular, the formation pathway of CBTS that includes in-situ formation of obstinate secondary phases such as $BaSO_4$ and Cu_2SnS_3, discouraging the formation of CBTS has been elucidated. Optical and electrical characterization of the resulting films revealed properties suitable for photovoltaic applications.

The main objectives of this thesis are

- Preparation of Cu_2BaSnS_4 (CBTS) based thin films using a solution-based approach such as spin coating.

- Study of phase evolution as a function of process parameters such as solution composition, post-deposition heat treatment, etc.
- Elucidation of the role of Se alloying with S in the parent CBTS system and examination of its effect on structural, electrical, and optical properties of the films.

1.6 Outline of the thesis

Chapter 1 involves the basic introduction of the materials and literature review. It underlines the key challenges in the material CZTS and the reason for its stagnated performance at 12.6%. Substitution of Zn in CZTS by a large ionic radius Ba, resulting in the formation of CBTS, has been studied. The experimental methods adapted by researchers for the fabrication of CBTS have been discussed in detail. This chapter provides a pathway for the formation of CBTS films by surveying from literature, which assists and paves the way to achieve the objectives.

Chapter 2 describes the experimental details of the fabrication of a precursor solution and CBTS(Se) thin films. It also highlights the deposition of Al contacts used for the various electrical measurements. This chapter includes details of the analytical methods and tools (for instance, XRD, Raman spectroscopy, SEM, EDS, I-V characteristics, impedance spectroscopy, etc.) used to characterize and analyse the obtained films.

Chapter 3 deals with the numerical simulation carried out in CZTS and CBTS solar cells in order to understand the defect tolerance of the CBTS as compared to CZTS. The role of defect densities at the MoS_2/CZTS, CZTS/CdS, and bulk CZTS has been studied to simulate the champion CZTS solar cell device. Introduction of the BSF layer at the rear contact of the device has been suggested and analysed by simulation. Further, the same values of the defect densities optimized in CZTS have been used for the simulation of the CBTS thin film solar cells. In addition, these defect densities were further tuned for simulating CBTS thin film solar cells.

Chapter 4 establishes the growth of CBTS films by using a molecular precursor solution, intuitively manipulating the Ba concentration in the solution, and the influencing methods of the post-sulfurization process. The output of post-deposition heat treatment were elucidated from methodical variation in the dwell time, temperature, and sulfur amount. High composition of Ba resulted in phase-pure CBTS thin film by sulfurization at a particular temperature, dwell time, and sulfur amount. This chapter highlights the optical and electrical properties of the phase-pure thin films. The obtained phase-pure CBTS films have shown ~30% white light photosensitivity.

Chapter 5 deals with the details of Se-alloying to make CBTSSe thin films. Selenium alloying is expected to help tune the bandgap of the film to make it suitable for solar spectrum absorption. A method of sulpho-selenization, meaning annealing of as-deposited films with S and Se both, has been adapted to make CBTSSe thin films. The role of dwell time, temperature, and sulfur amount on the evolution of single-phase CBTSSe was studied. Phase pure film was obtained for Ba/Sn=1.7 in the solution and film sulfurized at 550 °C for 45 minutes with 1.0 g of S and 0.1g of Se. Further, the amount of Se was varied from 0.1-0.4g during sulpho-selenization, and CBTSSe phase was obtained for all Se amounts. These films with different amounts of Se were further characterized for bandgap, surface morphology, and composition analysis.

Chapter 6 summarizes the results of the research carried out and presented in the earlier chapters. It also discusses the scope for future work.

CHAPTER 2

Experimental details

This chapter deals with the details of experimental methods used for synthesis of the Cu_2BaSnS_4 (CBTS) and Se-alloyed Cu_2BaSnS_4 (CBTSSe) thin films. This chapter also includes the details of the characterization techniques used to analyze the synthesized thin films and devices.

2.1 Deposition of CBTS/CBTSSe thin films

Among the various approaches to synthesize thin films, solution based approaches appear attractive because of the ability to deposit on large area substrate and low cost of the process. Molecular precursor solution based process offers various advantages such as control of composition, low temperature processing and less consumption of energy (Tumbul et al., 2019). However, in the case of solution processing of CBTS(Se) thin films, poor solubility of salts of Ba and formation of secondary phases pose major challenges (Teymur et al., 2018). In this work, 2-methoxy ethanol based molecular solutions are used to prepare the CBTS thin film by spin coating process. The precursor solution was formed by mixing two solutions. First a solution (sol A) was prepared by dissolving 1.545 g of cupric acetate $(CH_3COO)_2Cu{\cdot}H_2O$ (99%, AR/ACS Loba Chemie), 0.902 g of stannous chloride dihydrate $SnCl_2.2H_2O$ (98%, AR/ACS Loba Chemie) and 2.4358 g of thiourea NH_2CSNH_2 (99%, AR Loba Chemie) in 10 ml of 2-methoxyethanol (99.5%, AR/ACS Loba Chemie) separately under constant magnetic stirring at 60 °C for 1 hour. The solution thus obtained is clear solution of transparent yellow colour. Second solution (sol B) was prepared by mixing barium acetate $(CH_3COO)_2Ba$ (99%, ACS reagent Sigma-Aldrich) in 5 ml of 2-methoxyethanol with a few drops of lactic acid (92%, AR Spectrochem) with magnetic stirring at 70 °C for 30 min. In certain cases, the Ba/Sn ratio in the final precursor solution was changed by varying the amount of barium acetate in solution B. Solution A & B were mixed under constant magnetic stirring at 30 °C for 15 min to get a clear pale yellow precursor solution.

This precursor solution was deposited in form of the films on soda lime glass substrates by the spin coating technique. The precursor solution was put on the substrate dropwise using a dropper and spun at 1400 rpm for 20 s and the film was subsequently dried at 270 °C on hot plate for 2 min. This process was repeated five times in order to get an as-deposited film of sufficient thickness. This as-deposited film was sulfurized in a tubular furnace wherein the film was placed horizontally facing down the sulfur-powder (99.5% AR Loba Chemie) in an alumina crucible with lid on in flowing argon gas. Elemental Sulfur powder is used in this work instead of H_2S gas to avoid the toxicity and highly corrosive nature of H_2S gas as reported in CZTS preparation reports earlier (Xie et al., 2013). The temperature, time and the amount of sulfur powder during the sulfurization were varied in order to study the reaction process for the formation of CBTS phase. In all cases, samples were cooled down naturally to room temperature in Ar atmosphere. A schematic diagram of the film deposition process is depicted in **Fig. 2.1**.

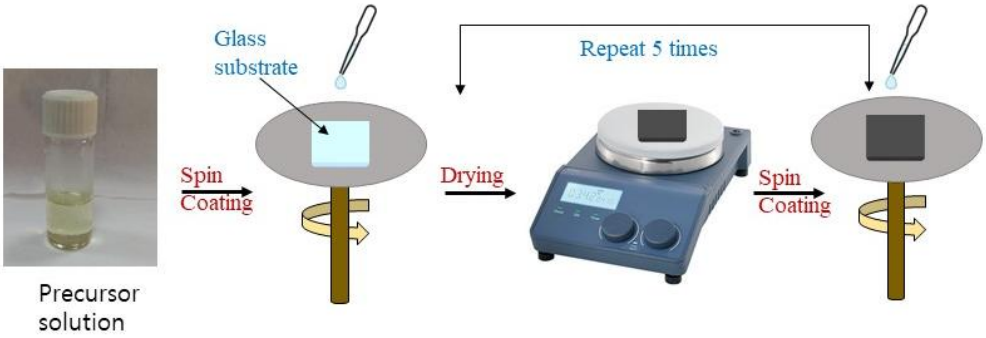

Fig. 2.1: Schematic diagram to depict the various steps used for the deposition of CBTS(Se) thin films using spin coating method.

Further, to prepare the selenium analogue of CBTS films i.e CBTSSe, we prepared the as-deposited films by the same process and the as-deposited films were then annealed in the tubular furnace same way as for CBTS but in the presence of both S-powder and Se-ingots (99.99% selenium shot, amorphous, 1-5 mm, Alfa Aesar). This process is referred as sulpho-selenization. Different amount of selenium (0.1 – 0.4 g) was used to vary the Se content in the films. The temperature and duration were optimized to get the phase pure CBTSSe thin films.

2.2 Deposition of Al-contacts

For electrical measurements such as photosensitivity, resistivity and Hall coefficient etc., aluminium contacts were prepared by thermal evaporation. Masks with two/four circular points of 3 mm diameter each were fabricated. Al-ingots were used for the thermal deposition in a vacuum chamber at the base pressure of 5×10^{-6} mbar. The thickness of Al contacts was about 250 nm.

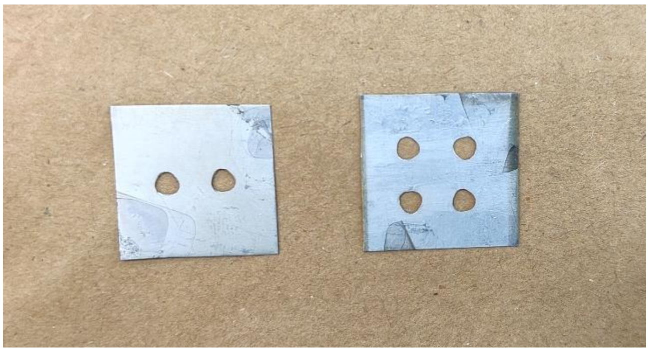

Fig. 2.2: Masks used during the deposition of the Al-contacts

2.3 Characterization techniques

Several characterization techniques were employed to analyse the formation of phase, microstructure, electrical and optical properties of the films. This section of the chapter gives brief information about those techniques.

2.3.1 Thermogravimetric analysis (TGA)

TGA is a technique which monitors the effect of temperature on the weight of the substance in a controlled atmosphere. This technique helps to quantitatively analyse the water loss, solvent loss, oxidation and decomposition in the material. In this work we first dried the precursor solution at 90°C for 12 hours in an oven and resultant powder is used for the TGA analysis. A NETZSCH system (STS 449 F3 Jupiter) system was used to obtain the TGA curve in nitrogen atmosphere.

Fig. 2.3: Actual photograph of the experimental setup used for TGA measurements

2.3.2 X-Ray Diffraction (XRD) measurements

XRD technique is the most widely used technique for the identification of the crystal structures An beam X-rays of wavelength λ is incident onto the atomic planes (separated by distance d from each other) at an angle θ. When the Bragg Equation is satisfied by X-rays entering the samples, an intense peak is obtained due to the phenomenon of the interference. The X-ray signal is recorded and converted the signal into a count rate by the detector. In order to calculate crystallites size of the films, the Debye-Scherrer equation, given below, was used (Cullity et al., 2014),

$$D = \frac{k\lambda}{\beta \cos\theta} \tag{2.1}$$

Where k represents Scherrer constant and denotes particle shape and its value commonly used is 0.9. Here, β is full width hall maxima (FWHM) of the peak and 2θ is Bragg's angle.

Fig. 2.4: Actual photograph of the experimental setup used for XRD measurements

In this work, the XRD measurements were performed on the sulfurized films to analyse phase formation using a Rigaku SmartLab SE diffractometer using Cu-Kα radiation.

2.3.3 Raman spectroscopy

Raman Spectroscopy relies on scattering of incident light to determine the chemical structure. Along with the identification of chemical structure, it helps to determine phase, intrinsic strain/stress and contamination/impurity if present in the material (Szymanski et al., 1967). Typically, a laser of particular wavelength is used as excitation source. Photons of the incident light induce polarization in the electron cloud of the molecule and transfer their energy to the molecule. This energy is re-emitted immediately as scattered light photons. These scattered photons can have different frequency than the incident photon and the shift in frequency is called Raman Shift. Raman shift projects information about the rotational and vibrational modes, and are characteristics of the molecules of the samples. Raman spectra creates a unique fingerprint of the samples that helps to identify it.

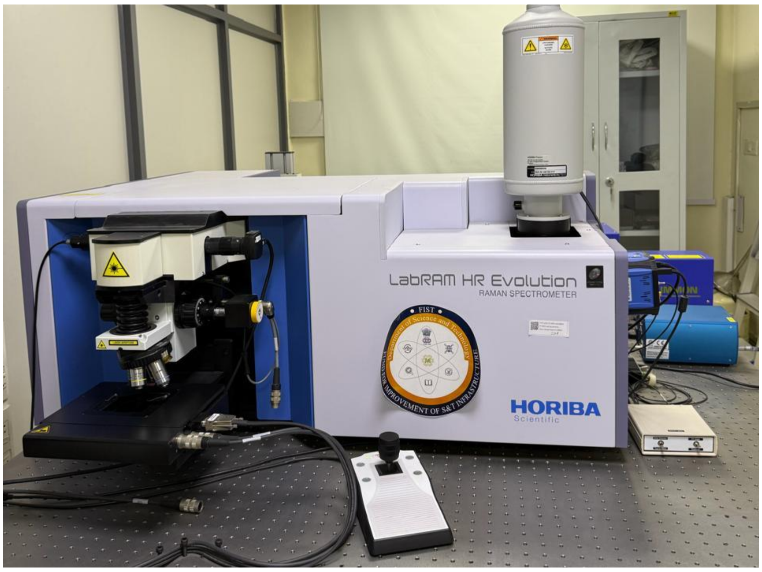

Fig. 2.5: Actual photograph of the experimental setup used for RAMAN measurements

In this work, we have used a LabRam HR Horiba Raman-spectrometer with a 532 nm laser.

2.3.4 Scanning electron microscope (SEM) and Energy dispersive X-ray spectroscopy (EDS)

The surface and cross section microstructure of the films was examined by the field emission scanning electron microscope (FESEM). It is based on the principle of capturing the image of the surface by interaction of electron beam with the surface. Electron beam in FESEM is created by potential gradient between cathode and anode using a field emission gun. Field emission gun uses a very sharp tipped single filament of tungsten to create electron beam and this beam is focused using an electromagnetic lens system (Goldstein et al., 2003). When a focused electron beam is incident on surface of the sample there is ejection of secondary and back-scattered (BS) electrons, and X-rays. Secondary and BS electrons are generated due to inelastic and elastic interactions, respectively. In this work, we have used a Carl Zeiss Sigma 500 microscope for capturing the surface and cross-sectional images.

For the elemental analysis of the films, EDS was employed using a Bruker QUANTAX 200 system at different points on the sample surface. In the EDS technique, the composition of the sample is obtained from the energy of the X-rays generated by electron irradiation. These incident electrons create a vacancy in the inner shell of the orbital of the constituent atom, thus the electrons from outer shells with higher energy are transferred to the vacancies emitting characteristic X-rays. These emitted X-rays have particular energy for every element and thus element can be identified by measuring the energy of the emitted X-rays.

2.3.5 UV-Vis spectroscopy

UV-Vis spectroscopy records the amount of light transmitted, absorbed and reflected by the sample in comparison to a given reference (glass in our case). The coefficient of absorption (α) was determined by using the following formula (Dolgonos et al., 2014),

$$\alpha = \frac{1}{t}\ln\left[\frac{(1-R)^2}{T}\right] \tag{2.2}$$

where, R is reflectance, T is transmittance and t represents sample thickness. With the help of absorption coefficient, we can calculate the bandgap of the material using the tauc plot using the following equation,

$$\alpha h\nu = A(\alpha h\nu - E_g)^{1/m} \tag{2.3}$$

where, h is Planck's constant, ν is incident photon frequency and A is a constant. Further, m is a constant that depend upon the nature of transition. Its value could be 1/2 for direct-allowed, 3/2 for direct forbidden and 2 for indirect-allowed transitions. In our case we have taken its value to be 1/2 considering direct allowed transitions (Chen el al., 2018).

Fig. 2.6: Actual photograph of the experimental setup used for UV measurements

We have used a Shimadzu spectrophotometer (UV-2600) for measuring the transmittance and reflectance of the sample in wavelength range of 300 - 1400 nm.

2.3.6 Photoluminescence measurements

Photoluminescence (PL) spectroscopy helps to study luminescence properties of the material. It can help to identify impurity levels present and recombination mechanism. It is based on the process of photoexcitation of the electrons to the excited state and then emission of the light when electron get relaxed from excited state to the ground state. First, the absorbance spectrum is evaluated for different wavelengths at fixed emission wavelength. Then, information from absorbance spectrum is used to fix the excitation wavelength for recording the emission spectrum. The emission spectra is then recorded for different wavelengths. The data recorded contains peak emission intensity vs wavelength, which helps to determine the bandgap. In this work, we have used an Agilent Cary Eclipse Fluorescence spectrophotometer to record emission spectra at an excitation wavelength of 440 nm.

2.3.7 Resistivity and Hall measurements

Resistivity of the film was measured using the four-probe Van der Pauw method. According to this method, four ohmic contacts are placed at the periphery of the sample. Current is passed through two terminals and voltage is measured across the opposite two terminals as shown in **Fig. 2.3.** Then, the terminals were reversed in polarity, and both horizontal and vertical arrangements were considered. Thus, the same measurement is repeated eight times. These eight values used to find the resistance by employing ohm’s law R= V/I.

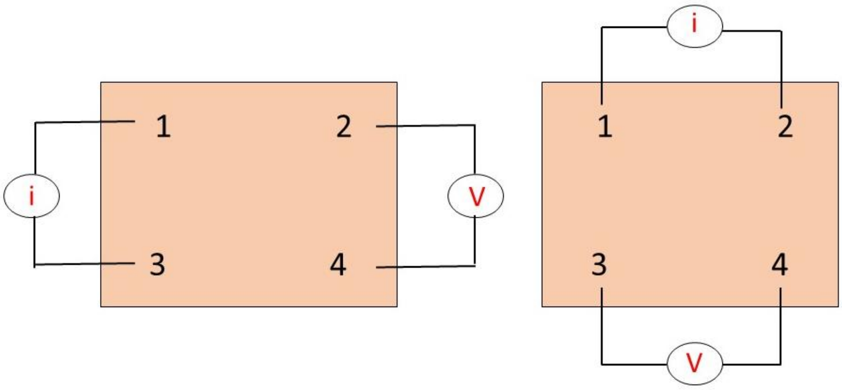

Fig. 2.7: Vertical and horizontal arrangements used for resistivity measurements

The sheet resistance (R_s) of the film can be found by using the thus measured resistance R from the following formula,

$$R_s = \frac{\pi R}{\ln 2} \tag{2.4}$$

Where t is thickness of the film and R is average of the horizontal and vertical resistances of the sample. Resistivity can be calculated by (Van der Pauw 1958 (a & b)),

$$\rho = R_s t \tag{2.5}$$

In this work, we have used a Keithley 2450 source measure unit for the I-V measurement.

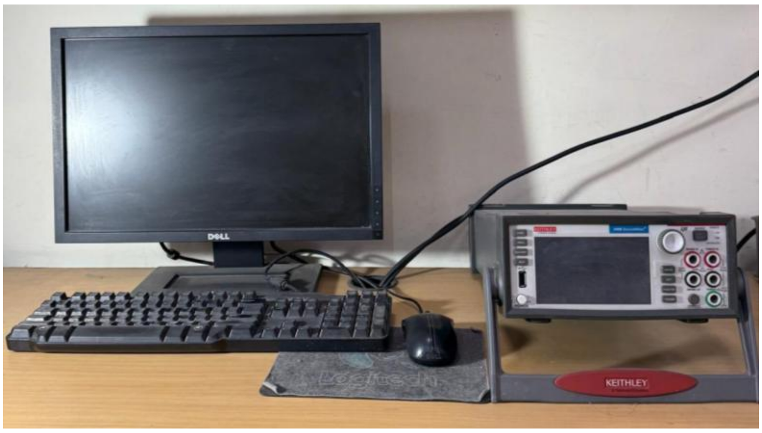

Fig. 2.8: Actual photograph of the experimental setup used for resistivity and Hall measurements

Hall measurements were taken using an in house developed setup. In Hall measurement, current is passed through the diagonal contacts and voltage is recoded in the other diagonal. Samples are placed between the electromagnets and measurements were done in presence of magnetic field of 0.4 T at room temperature.

2.3.8 Photosensitivity measurements

Photosensitivity of the films was calculated by measuring current through the sample in dark and light conditions. Two aluminium contacts (circles of 3 mm dia) were deposited on the films by thermal evaporation using shadow masks (Section 2.2). A constant voltage is applied and current is recorded with light on and off. Measurements were performed with a Keithley 2450 source measure unit. The samples were illuminated by white light of intensity of about 24 mW/cm^2.

2.3.9 Electrochemical impedance spectroscopy (EIS)

EIS technique is used to study the system response to applied potential or passed current with respect to frequency (Wang et al., 2021). The data recorded by EIS technique is generally analysed by using the Nyquist and Bode plots. The Nyquist plot represents value of impedance in complex plane with its real part and imaginary part on the x and y-axis respectively.

However, the Bode plot contains log of frequency on x-axis and log of impedance on first ordinate and phase shift (ϕ) on second ordinate.

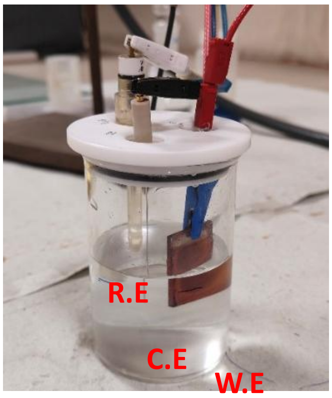

Fig. 2.9: Photograph of an electrochemical cell used for the EIS measurements

In this work, the EIS measurements were performed by using an electrochemical workstation (Model: Biologic VSP300). The electrochemical cell was a three-electrode system with Ag/AgCl and Pt-wire as reference electrode and counter electrode, respectively as shown in **Fig. 2.3**. The Ag/AgCl electrode was saturated in KCl (0.197 vs normal hydrogen electrode). The CBTS/CBTSSe thin films deposited on fluorine doped tin oxide (FTO) coated glass substrates with 0.2 cm^2 area dipped in the electrolyte was used as the working electrode. A neutral solution of Na_2SO_4 with pH 7.0 and 0.1 M molarity was used as electrolyte in the measurements. The EIS measurement was carried out using potentiostatic condition with frequency in the range of 5 MHz to 1 Hz with 10 mV applied potential.

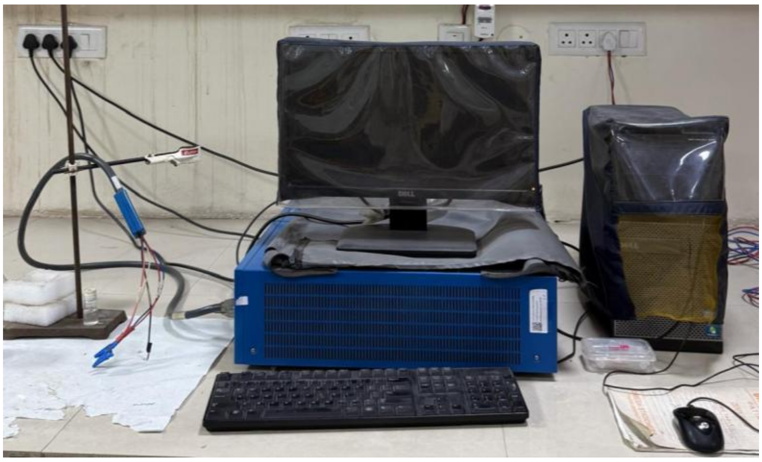

Fig. 2.10: Actual photograph of the experimental setup used for Nyquist and Mott-Schottky measurements

Acceptor concentration and position of the band edges were determined from Mott-Schottky (MS) plots. For the MS plots, the space charge region capacitance (C_s) was recorded with respect to the potential difference (V) between the semiconductor and electrolyte interface. When the semiconductor comes in contact with electrolyte redistribution of charges take place, and the conduction and valance band edges get shifted to match the semiconductor fermi level with redox potential of the electrolyte. However, there exist an applied potential where no band bending takes place and this is referred as flat-band potential (E_{FB}). From the x-intercept of $1/C_s^2$ versus V plot, we can find V_{FB} and from its slope, the acceptor concentration of the semiconductor (N_A) can be determined using the following equations,

$$\frac{1}{C_S{}^2} = \frac{-2}{q\varepsilon_0\varepsilon_S N_A A^2}\left(V - V_{FB} + \frac{KT}{q}\right) \qquad (2.6)$$

Furthermore, the valance band edge can be found by using the following equation,

$$E_{VB} = V_{FB} + \frac{KT}{q}\ln\left(\frac{N_V}{N_A}\right) \qquad (2.7)$$

From the knowledge of the valance band edge position (E_{VB}) and the bandgap (E_g) of the semiconductor, the bottom of the conduction band (E_{CB}) can be calculated as $E_{CB} = E_{VB} + E_g$. This will help to draw a complete energy band edge diagram.

CHAPTER 3

Analysis of CZTS and CBTS thin film solar cells by numerical simulations

As discussed in Chapter 1, although CZTS has drawn significant research attention in recent years as an alternate absorber material for thin film solar cells, the highest efficiency achieved for the solar cells of CZTS and CZTSSe is stagnated at 11.03% and 12.6%, respectively (Mitzi et al., 2011; Walsh et al., 2012). This inferior performance compared to the CIGS and CdTe based thin film solar cells has been attributed to a large V_{oc} deficit, which is reportedly caused by various recombination losses of the photogenerated charge carriers (Mitzi et al., 2013; Chen et al., 2010a; Chen et al., 2010b). Among the various strategies attempted to minimise the V_{OC} deficit, minimization of recombination at the front and rear interfaces has drawn the interest of many groups (Song et al., 2020; Kaur et al., 2017; Scragg et al., 2011; Scragg et al., 2013; Park et al., 2018; Shin et al., 2013). At the rear interface (i.e., at the back contact Mo), a degradation reaction occurs during the sulfurization process yielding a MoS_x layer (Scragg et al., 2011) that deteriorates the device performance by increasing the series resistance (Shin et al., 2013). In order to inhibit this reaction, the growth of an intermediate layer between the Mo and the CZTS has been proposed. These layers between the Mo and CZTS prevented the detrimental reaction (i.e., the formation of the MoS_2 layer) at the rear contact by blocking the diffusion of S towards it (Liu et al., 2017; Lu et al., 2020). While the use of the intermediate layers has yielded better efficiency compared to the devices without the intermediate layers (Scragg et al., 2013; Cui et al., 2014; Liu F. et al., 2014; Li et al., 2014; Park et al., 2018; Liu X. et al., 2014), further improvement is warranted.

Another issue associated with the back contact is the existence of a potential barrier for the photogenerated holes. This barrier facilitates carrier recombination leading to the reduction in collection efficiency and hence, performance degradation (Bar et al., 2008). Incidentally, the recombination losses is exaggerated due to a large back contact area, typically used in the CZTS devices (Dasa et al., 2012). The barrier for transporting the photogenerated holes can be lowered, for example, by introducing a back surface field (BSF) through the insertion of a p-type intermediate layer (von Roos, 1978; Khosroabadi and Keshmiri, 2014; Ghobadia et al., 2020; Benzetta et al., 2021). This approach relies on creation of a built-in field in the direction same as that in the p-CZTS/n- CdS junction of the solar cell. This electric field, in turn, would provide a conductive path to the holes and act as a potential barrier to the minority carrier electrons, thus minimizing the recombination at the back contact interface. Since, the width of the depletion region - wherein the built-in field is operational - is extended into the regions with lower carrier concentration, an effective BSF layer is required to be heavily doped (p^+ type) compared to the CZTS layer.

In this chapter, we have studied the CZTS and CBTS based solar cells by numerical simulations and identified the performance limiting factors. In particular, the role of defects at the front and back interfaces as well as in the bulk of the absorber layer have been established. We also show how by using a BSF layer, the carrier collection can be manipulated to improve the performance of the CZTS and the CBTS based solar cells.

3.1 Simulation methodology

The numerical analysis of a device involved solving the continuity equation for electrons and holes, and the Poisson's equation as implemented in the Solar Cell Capacitance Simulator (SCAPS) 3.3.08 package. For the simulations, SCAPS solves the basic semiconductor equations (the Poisson equation, relating charge with electrostatic potential (φ), and continuity equations). The Poisson equation is given by,

$$\frac{d^2\varphi}{dx^2} = \frac{e}{\varepsilon_o \varepsilon_r}(p - n + N_D - N_A + \rho_P - \rho_n) \qquad (3.1)$$

where e is electric charge, ε_o is permittivity of free space, ε_r is relative permittivity, n and p are electron and hole concentration, respectively, N_D and N_A are donor and acceptor concentration, respectively, and ρ_n and ρ_P are electron and hole distribution, respectively. The continuity equation is given as

$$\frac{dj_n}{dx} = G - R \qquad \frac{dj_p}{dx} = G - R \qquad (3.2)$$

where j_n and j_p is current density of electron and hole, respectively, and R and G are recombination and generation rate, respectively (Mostefaoui et al., 2015). The drift and diffusion equations for the charge carrier transport are given by: $j_n = D_n \frac{dn}{dx} + \mu_n n \frac{d\varphi}{dx}$; $j_p = D_p \frac{dp}{dx} + \mu_p p \frac{d\varphi}{dx}$ where μ_n and μ_p are mobility of the electrons and holes, D_n and D_p are corresponding diffusion coefficient (Burgelman et al., 2000). For a more accurate prediction of the device performance, possible recombinations at interfaces based on Shockley-Read-Hall formalism have been included. The considered cell structure is same as the experimental cell, which has yielded the highest efficiency for CZTS (Yan et al., 2018).

3.2 Simulation of CZTS solar cell

3.2.1 Simulations without including defects

Due to peculiar material properties of CZTS, irrespective of the thin film synthesis routes, numerous point antisite defects, interstitials and vacancies are found in the bulk of the film (Chen et al., 2010). These defects form acceptor/donor levels and deep trap states in the energy bandgap of CZTS, which act as recombination centres for the photogenerated electron-hole pairs. For instance, Gershon et al. reported an 8.3% efficient CZTS solar cell with an overall radiative defect density of ~10^{19} cm^{-3} (Gershon et al., 2013). On the other hand, significant interface defects at the Mo/CZTS junction can stem from the growth of the MoS_2 layer due to the high value of vapour pressure of sulphur during the formation of CZTS (Scragg et al., 2011). This MoS_2 layer typically results in increased series resistance and reduced efficiency (η) of the device (Zhang et al., 2021). For a systematic analysis, we have first evaluated device performance without considering any defect. Figure 3.1 shows a typical device structure of Mo/CZTS/CdS/i-ZnO/ITO/Al, which is similar to the best CZTS solar cell. The CZTS device was illuminated with one sun (=1000 W/m^2) illumination named as "AM1_5G 1 sun" with the air mass 1.5, global in SCAPS-3.3.08 package. The values of shunt and series resistance considered in our numerical study were taken from the experimental work as 1.02×10^3 Ωcm^2 and 2.58 Ω, respectively (Yan et al., 2018). For the absorption coefficient of the layers, 'Eg-sqrt' model is used in the SCAPS-3.3.08. The material and device parameters used in this work are listed in Tables 3.1 and 3.2.

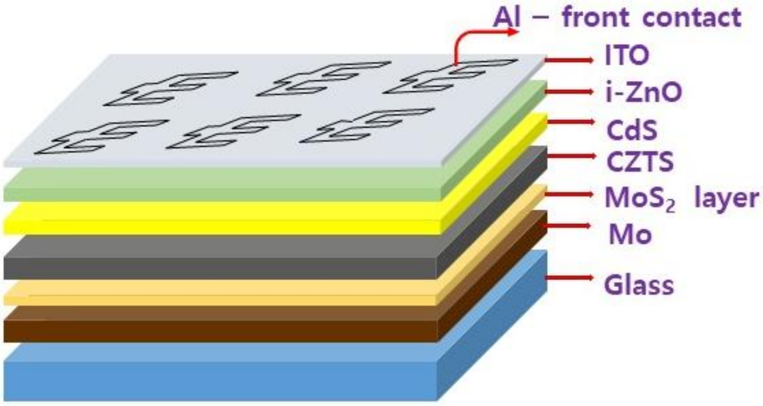

Fig. 3.1: Schematic view of the device structure considered for simulations. During the growth of the absorber CZTS layer, a thin MoS_2 layer is unintentionally formed. Hence, for a realistic simulation, the MoS_2 layer has been included.

Table 3.1: Parameters for front and back contacts used in the simulation

Properties of back metal contact		Properties of front metal contact	
Metal work function	5 eV	Metal work function	Flat bands
SRV of electron	10^5 cm/s	SRV of electron	10^7 cm/s
SRV of hole	10^7 cm/s	SRV of hole	10^5 cm/s

Table 3.2: Parameters for different layers used in the simulation

	MoS_2	**CZTS**	**CBTS**	**CdS**	**i-ZnO**	**ITO**
Thickness (µm)	0.3	0.8	0.80	0.06	0.06	0.24
Bandgap (eV)	1.3	1.5	1.9	2.4	3.4	3.3
Electron affinity (eV)	4.0	4.5	3.6	4.45	4.6	4.10
Dielectric permittivity	4.0	10.0	5.44	10.0	9.0	10.0
CB effective density of states ($\times10^{17}/cm^3$)	7.50	22.00	22.00	10.00	10.00	20.00
VB effective density of states ($\times10^{18}/cm^3$)	1.800	18.00	18.00	10.00	10.00	18.00
Electron thermal velocity ($\times10^7$ cm/s)	1.00	1.00	1.00	1.00	1.00	1.00
Hole thermal velocity ($\times10^7$ cm/s)	1.00	1.00	1.00	1.00	1.00	1.00
Electron mobility ($\times10^2$ cm^2/Vs)	1.00	1.00	30	1.00	1.00	0.5
Hole mobility ($\times10^1$ cm^2/Vs)	15.00	2.50	10	2.50	2.50	7.50
Donor density ($\times10^{17}$)	0	0	0	10.00	1.00	100.00
Acceptor density ($\times10^{15}$)	1.00	33.0	1.00	0	0	0

The data for MoS_2, CZTS, CBTS, CdS, i-ZnO and ITO have been taken from the references Lin et al., 2020, Gupta and Dixit, 2018, Khattak et al., 2018, Sadanand and Dwivedi, 2019, Hamri et al., 2019 and Adewoyin et al., 2018, respectively.

From the simulation, it was found that the device efficiency could be as high as ~17.68%, as shown in Fig. 3.2. This value is significantly higher than the reported highest efficiency (11.03%) of pure sulfide solar cell (Yan et al., 2018). This increased efficiency of 17.68% is closer to theoretically predicted Shockley-Queisser limit for CZTS (~28%) (Sravani et al., 2021) as compared to experimentally achieved value of 11.03%. The reason for the same may be the absence of defects at interfaces and bulk CZTS that decreases the loss of photogenerated charge carriers, and thereby increasing the number of charge carriers collected and the efficiency.

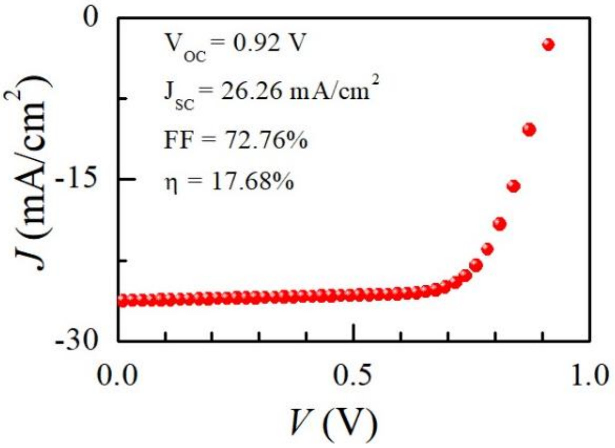

Fig. 3.2: Current density (*J*) versus voltage (*V*) characteristics of the CZTS solar cell without considering any defects either in the bulk or at interfaces. The device showed 17.68% efficiency, which is far better than champion efficiency 11.03% obtained experimentally till date (Yan et al., 2018).

3.2.2 Simulations including interface and bulk defects

The result presented in the preceding section (Section 3.2.1) revealed a large difference in the efficiency of the simulated and the experimental cells. This discrepancy is primarily since the simulation did not include any possible defects on the interface and bulk of CZTS. Hence, for a realistic analysis of the CZTS based device, we have investigated the role of defect densities at MoS_2/CZTS interface (N_{i1}), CZTS/CdS interface (N_{i2}), and bulk CZTS absorber (N_b), separately and in combination. The defects in the CZTS and at the CZTS/CdS interface are set at 0.6 eV above the valance band of CZTS (Wanda et al., 2016). The value of N_b is varied from $10^{12} – 10^{20}$ cm^{-3} due to which the minority carrier lifetime lies in the range of 10^{-4} - 10^{-12}s of the reported kesterite device (Courel et al., 2016). The defect densities at MoS_2/CZTS interface (N_{i1}) and at CZTS/CdS interface (N_{i2}) were varied in such a way to keep the interface recombination speeds in the range 1 × 10^4 to 1 × 10^{12} cm/s, as reported (Bouarissa et al., 2021).

Figure 3.3 shows contour plot of bulk defect density N_b and MoS_2/CZTS interface defect density N_{i1} dependence of the device performance metrics.

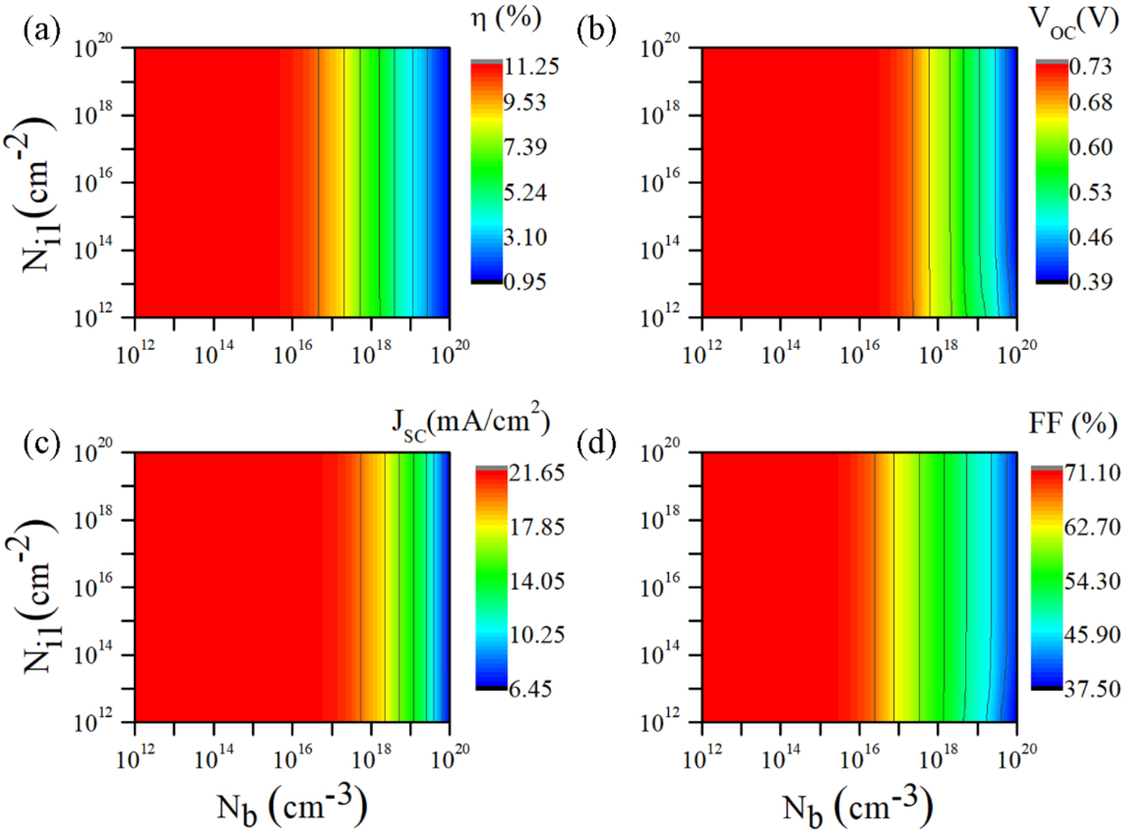

Fig. 3.3: Contour plots depicting the effect of defect density in bulk CZTS (N_b) and defect density at MoS_2/CZTS interface (N_{i1}) on (a) efficiency η, (b) Open circuit voltage V_{OC}, (c) short circuit current density J_{SC} and (d) Fill Factor FF of the considered device.

As evidenced, for the defect densities N_b in the range of 10^{12} to 10^{16} cm^{-3} and N_{i1} in the range of 10^{12} to 10^{16} cm^{-2}, the device performance remains unaffected. However, beyond the values of 10^{16} cm^{-3}, the bulk defect density N_b affected the device performance greatly whereas the MoS_2/CZTS interface defect density N_{i1} had little impact at a particular value of N_b. For example, for a value of $N_b = 10^{20}$ cm^{-3}, the device efficiency remained around 1% despite variation in N_{i1} from 10^{12} to 10^{20} cm^{-2}. The figure shows that the V_{OC} decreased from 0.73 to 0.39 V, J_{SC} from 21.65 to 6.45 mA/cm^2 and FF from 71.10 to 37.50% resulting in drastic decrease in η from 11.25 to 0.95%. This deterioration with increasing N_b is primarily due to the decrease in lifetime of the minority charge carriers as given by $\tau = 1/\sigma v N_t$ where σ is conductivity, v is speed and N_t is the total defect density (Courel et al., 2016).

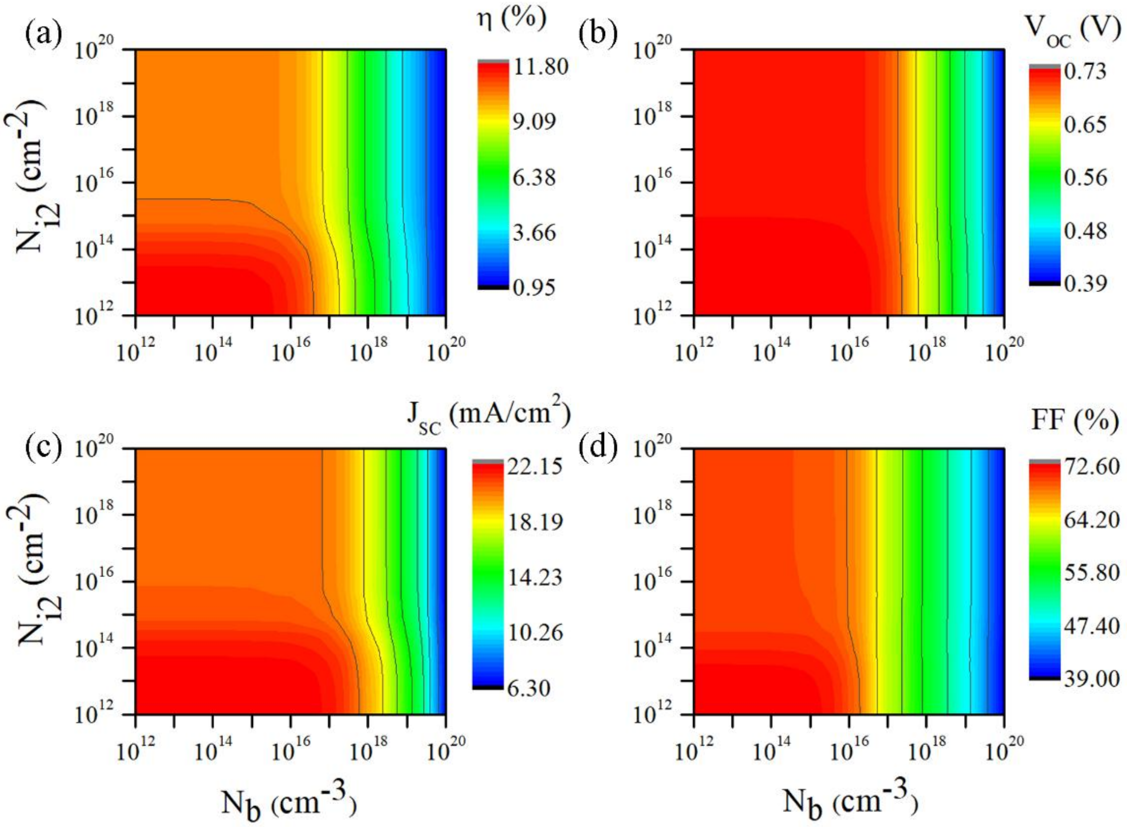

Fig. 3.4: Contour plots depicting the effect of defect density in bulk CZTS (N_b) and defect density at CZTS/CdS interface (N_{i2}) on (a) efficiency η, (b) Open circuit voltage V_{OC}, (c) short circuit current density J_{SC} and (d) Fill Factor FF of the considered device. Refer to the text for the minority carrier lifetime and recombination speed at the said interface.

Alternately, the defect density at the CZTS/CdS interface (N_{i2}) had a dominating effect similar to that of the bulk defect density (N_b) as shown Fig. 3.4. It is observed that V_{OC} decreased from 0.7340 to 0.3920 V with change in N_b but remained unaffected by change in the value of N_{i2}. On the other hand, both N_{i2} and N_b affected J_{SC} and thus efficiency of the device significantly. Keeping $N_b = 10^{12}$ cm^{-3} and changing N_{i2} value from 10^{12} to 10^{20} cm^{-2}, J_{SC} decreased from 22.13 to 20.48 mA/cm^2 (~7% decrease) and efficiency decreased from 11.78 to 10.38% (~11% decrease). On the other hand, keeping $N_{i2} = 10^{12}$ cm^{-2} and changing N_b from 10^{12} to 10^{20} cm^{-3}, J_{SC} decreased from 22.13 to 6.56 mA/cm^2 (~70% decrease) and efficiency from 11.78 to 1.34% (~89% decrease). This suggests the more crucial dependence of performance metrics on the defect density at bulk CZTS as compared to defects at the CZTS/CdS interface.

We have then used our data to predict defect densities while modelling the reported highest efficiency (Yan et al., 2018). The value of defect density at CZTS/CdS interface is chosen to be 1×10^{14} cm^{-2} which corresponds to interface recombination speed of 1×10^{6} cm/s. The bulk defect density was considered to be 5.5×10^{15} cm^{-3}, which corresponds to the minority carrier lifetime of 18 ns (using $\tau = 1/\sigma v N_t$, where σ is conductivity, v is speed and N_t is the total defect density) (Courel et al., 2016) and the value of MoS_2/CZTS interface defect density is considered to be 1×0^{15}cm^{-2}.

Using these values of defect densities, a CZTS solar cell has been designed and the results are presented in Fig. 3.5. From the band diagram of the device under illumination (Fig. 3.5a), formation of MoS_2 layer at the back contact introduced a negative VBO = -0.7 eV, This was calculated from VBO = $(\chi_{MoS_2} + E_{g,MoS_2}) - (\chi_{CZTS} + E_{g,CZTS})$, where χ and E_g are the electron affinity and bandgap of the corresponding materials (Minemoto et al., 2015). This VBO acts as a barrier for the movement of holes towards the back contact and is detrimental for the device performance. As expected, due to the high defect density, a sharp reduction in the charge carriers near interfaces is observed (Fig. 3.5b). The current density profiles corresponding to electrons and holes across depth of the device are also shown in Fig. 3.5c. The simulated device exhibited V_{OC} = 0.73V, J_{SC} = 21.59 mA/cm^2, FF = 69.77% and η = 11.0% as shown in Fig. 3.5d, which are very close to the experimental value (Yan et al., 2018). The close similarity in performance metrics of the simulated device and the experimental one validates the defect densities in the CZTS and at the interfaces considered here.

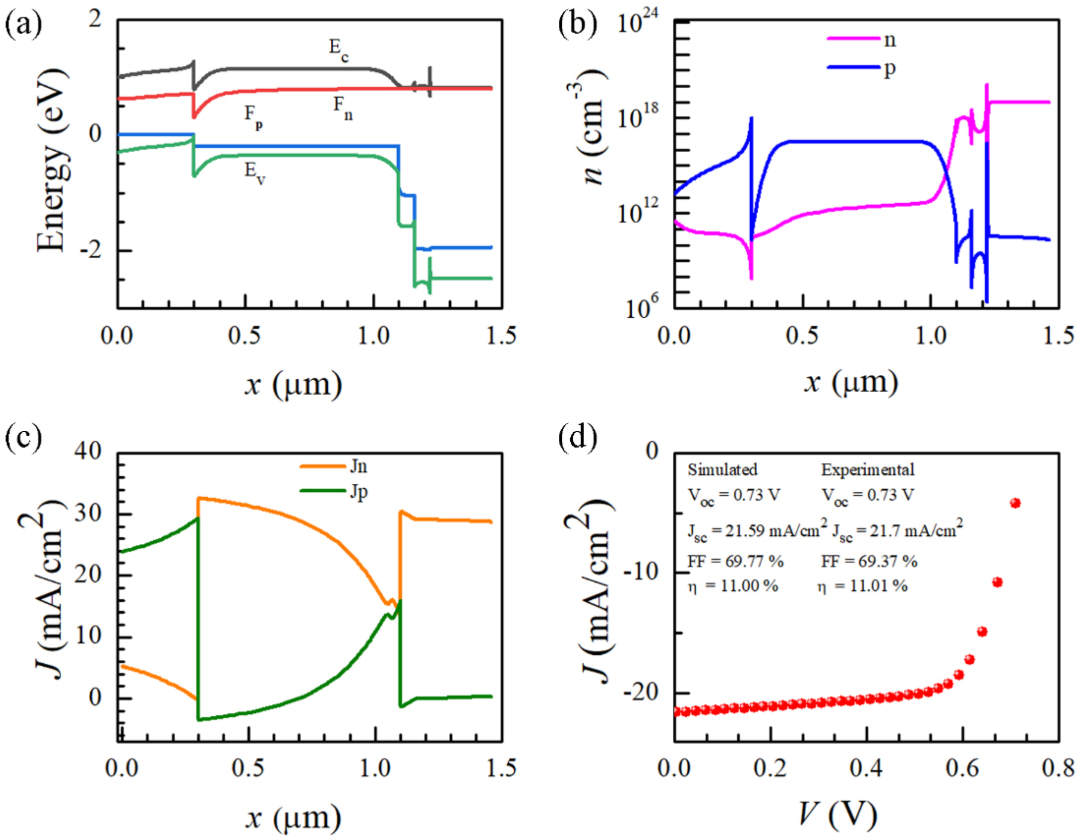

Fig. 3.5: (a) Position of band edges, and distribution of (b) carrier concentration *n* and (c) current density *J* across the device. The parameter *x* indicates the distance from the surface of the Mo film (i.e., x = 0 indicates the Mo film surface). The thickness of the layers is given in Table 3.2. A valence band offset VBO of -0.7 eV at MoS_2/CZTS interface was estimated in (a); (d) Current density *J* vs *V* characteristics of the simulated device. Note that the simulations correctly predicted the performance of the experimentally obtained champion cell (Yan et al., 2018). The comparison is listed as inset to (d).

We have next evaluated the impact of the bulk and interface defects individually to determine which defects are more damaging compared to others. The optimized values (the values which successfully yielded the experimental device output) of the defect densities N_b, N_{i1} and N_{i2} were considered for this simulation. Figure 3.6 shows comparative current density *J* vs *V* curves of the devices without defects (in both bulk and the interfaces), defects only in bulk of CZTS (5.5×10^{15} cm^{-3}), defects at MoS_2/CZTS interface (1×10^{15} cm^{-2}) and defects at CZTS/ CdS interface (1×10^{14} cm^{-2}). It is found that by considering defects only in the bulk of CZTS, the efficiency decreased to 14.16 from 17.68%, whereas the efficiency decreased to 11.80 and 14.71% when defects were included only at the MoS_2/CZTS interface and at the

CZTS/CdS interface, respectively. This suggests that defects present at the MoS_2/ CZTS interface is more damaging than the other defects.

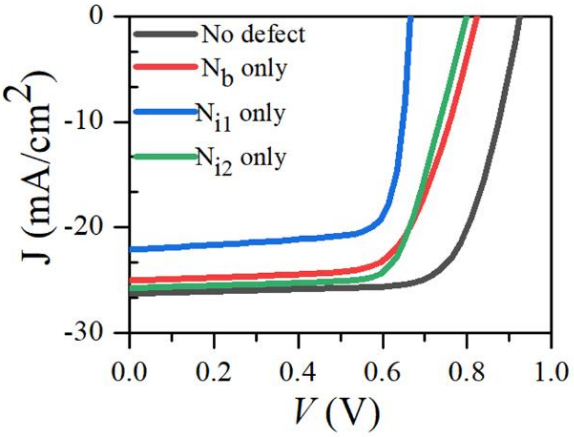

Fig. 3.6: Comparison of the current density *J* versus voltage *V* characteristics of the CZTS solar cell to show the impact of defect density in the bulk of CZTS (N_b) and at interfaces (N_{i1} at MoS_2/CZTS interface and N_{i2} at CZTS/CdS interface). Simulations yielded $\eta = 17.68\%$ for devices without any defect, $\eta = 14.16\%$ for defects only in the bulk CZTS, $\eta = 14.71\%$ for defects only at the CZTS/CdS interface, and $\eta = 11.80\%$ for defects only at the MoS_2/CZTS interface. The defects at the MoS_2/CZTS are found to be more damaging than the others.

3.2.3 Introduction of a BSF layer to boost the performance of solar cells

As discussed earlier, when a p^+-type BSF layer is inserted between the bottom contact (Mo) and the absorber layer (CZTS), it provides a conductive path to the holes and act as a potential barrier to the minority carrier electrons, thus minimizing the recombination at the back contact interface. Although the approach of using a BSF layer appears attractive, there are only a couple of studies of the same in the CZTS or CZTSSe based solar cells (Khattak et al., 2018; Benzetta et al., 2020; Giraldo et al., 2021). Khattak et al. used $Cu_2ZnSnSe_4$ (CZTSe) as a BSF layer to CZTS solar cell and numerically found an increase in efficiency from 9.61 to 12.92% with the introduction of BSF layer (Khattak et al., 2018). It may be noted that experimentally realization of a junction of phase pure CZTSe and CZTS will be very challenging due to inherent material peculiarities of these materials (Just et al., 2016). In a more recent report, Song et al. have shown performance improvement in the CZTSSe based solar cells by growing a p-type $MoSe_2$:Nb layer (Song et al., 2020). Nevertheless, a more detailed investigation of the effect of the BSF layer including the analysis of the band offsets at the BSF layer/CZTS interface (Scheer, 2009) is required.

In this section, the role of defect density at the interfaces and in the bulk of CZTS and the effect of the properties of the BSF layer on overall device performance have been studied in detail. We have numerically investigated the impact of a BSF layer in the form of Cu_2O, which has not been explored in the CZTS solar cells previously. It may be noted that the fabrication of Cu_2O is relatively straightforward and may be easily implemented experimentally (Drobny and Pulfrey, 1979; Herion et al., 1980; Golden et al., 1996; Meyer et al., 2012; Zuo and Ding, 2015; Yu et al., 2016). Significant enhancement in η of the CZTS solar cells up to 14.70% is observed primarily due to a decreased recombination current density facilitated by an optimized Cu_2O BSF layer. In addition, for a comparison with the reported improved performance due to a SnS layer near the back interface (Omrani et al., 2018; Ren et al., 2017), we show that for a high acceptor concentration (~10^{22} cm^{-3}), an efficiency as high as 15.70% can be achieved. Furthermore, a better understanding of the role of valance band offset (VBO) at the back interface has been achieved by studying the variation in electron affinity of the BSF layer.

3.2.3.1 Cu_2O as a BSF layer

In our study, we have included a 100 nm thick Cu_2O layer (with an acceptor concentration N_{A+} of 5.0×10^{18} cm^{-3}) between the Mo and the CZTS absorber layer to elucidate the potential benefits of BSF. The material properties of Cu_2O layer used in simulations are listed in Table 3.3. It is worth noting that the simulations include defect densities similar to the ones assumed in the study of the experimentally obtained highest efficiency CZTS cell (shown in Fig. 3.5d). Figures 3.7a-c show the energy band diagram, distribution of carrier density and current density across the device, respectively. Figure 3.7d shows the current–voltage characteristic of the device. With the introduction of the Cu_2O BSF layer, the open circuit voltage (V_{OC}) increased from 0.7303 to 0.7497 V and the efficiency of the device increased marginally to 11.35 from 11.01%. However, the J_{SC} and fill factor FF were not much affected, which may be most likely due to the fact that short wavelength photons are absorbed by the n-layer and long wavelength photons are absorbed by p-layer and by adding a BSF layer there is no effective improvement in overall photon absorption. From the bandgap and electron affinity values of BSF and absorber layer, a negative VBO of -0.7 eV between Cu_2O and CZTS, and an activation energy for recombination $E_a = 0.8$ eV ($E_a = E_{g,abs} - |VBO|$) were estimated. The role of VBO in the increase in efficiency is ruled out since VBO with Cu_2O is similar to that of the MoS_2 layer (Fig. 3.5a). Instead, the enhanced performance is attributed to high doping in Cu_2O, which is of the order of 10^{18} cm^{-3} as compared to 10^{16} cm^{-3} of CZTS layer. This concentration gradient between p+-Cu_2O and p-CZTS layer created a built-in field at the p+ -p junction which led to the diffusion of holes from p+ to the p layer to establish equilibrium hole density. When the device is illuminated, the photogenerated electrons move towards the n-layer for collection whereas the holes flow towards the p+-layer to maintain the equilibrium at p+-p junction and thus the photogenerated electron-hole pairs get separated yielding an improved V_{OC} (Mandelkorn and Lamneck, 1975).

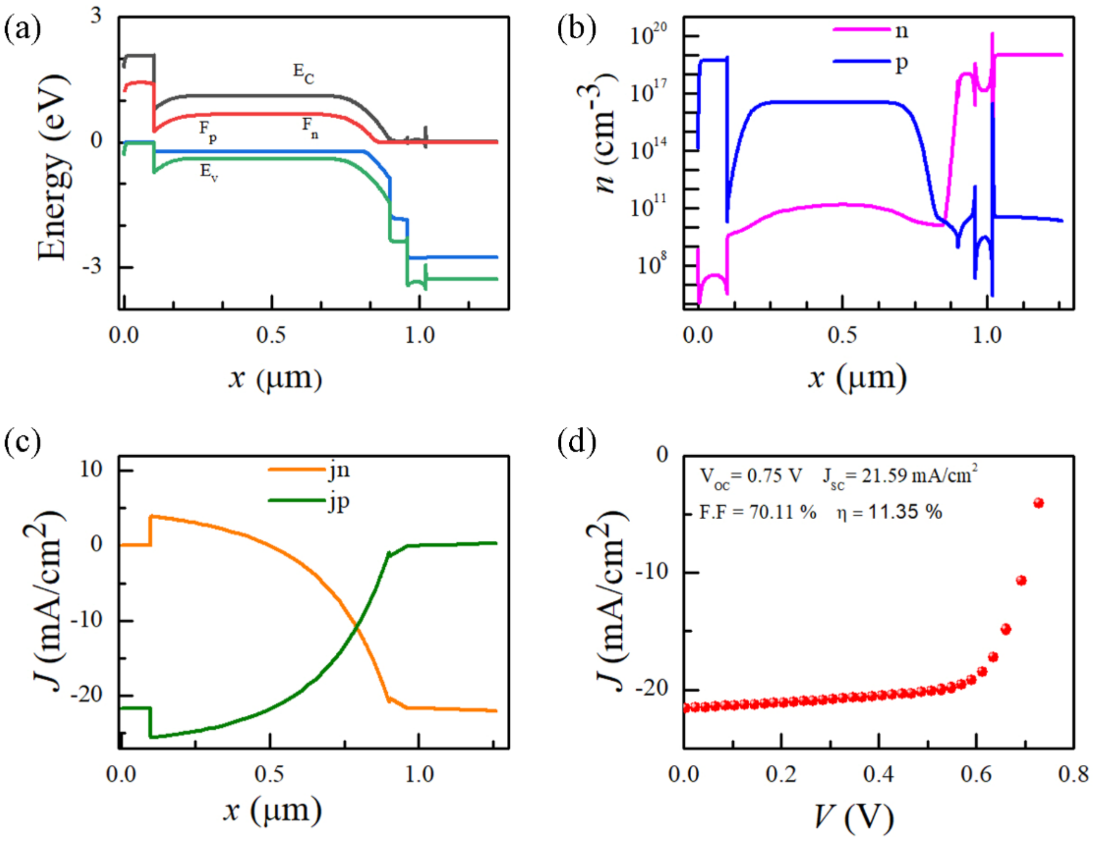

Fig. 3.7: (a) Position of band edges, and distribution of (b) carrier concentration *n* and (c) current density *J* across the device having a Cu_2O BSF layer. The parameter *x* indicates the distance from the surface of the Mo film (i.e., x = 0 indicates the Mo film surface). A valence band offset VBO of - 0.7 eV at Cu_2O/CZTS interface was estimated in (a); (d) Current density *J* vs *V* characteristics of the simulated device.

In order to study the role of band alignment at the back interface of the device, we have investigated the role of VBO that depends on the bandgap and difference in electron affinity of the absorber (CZTS) and the BSF (Cu_2O) layers. The values of bandgap and electron affinity of the CZTS layer and the value of bandgap of Cu_2O BSF were kept fixed and the value of electron affinity of the Cu_2O BSF layer was varied from 2.7 to 3.4 eV (Ichimura and Song, 2011; Wong et al., 2010), and thus, the VBO from -1.2 to -0.5 eV. It may be noted here that values beyond this range led to convergence failure of the program. The results of the simulation due to the change in the VBO are presented in Fig. 3.8. It was observed that with the decrease in |VBO| from 1.2 to 0.5 eV, the V_{OC} increased from 0.25 to 0.94 V, J_{SC} from 20.6518 to 21.83 mA/cm^2 and FF from 47.75 to 72.25% leading to significant enhancement in device efficiency from 2.47 to 14.80%. This increase in performance metrics is due to the reduction in barrier height at the back interface that facilitated the transportation of holes towards the back contact. Moreover, the decrease in |*VBO*| from 1.2 to 0.5 eV resulted an increase in activation energy for recombination from 0.3 to 1.0 eV ($E_a = E_{g,abs} - |VBO|$), which decreased the recombination possibilities at the interface and thus, enhanced the device performance.

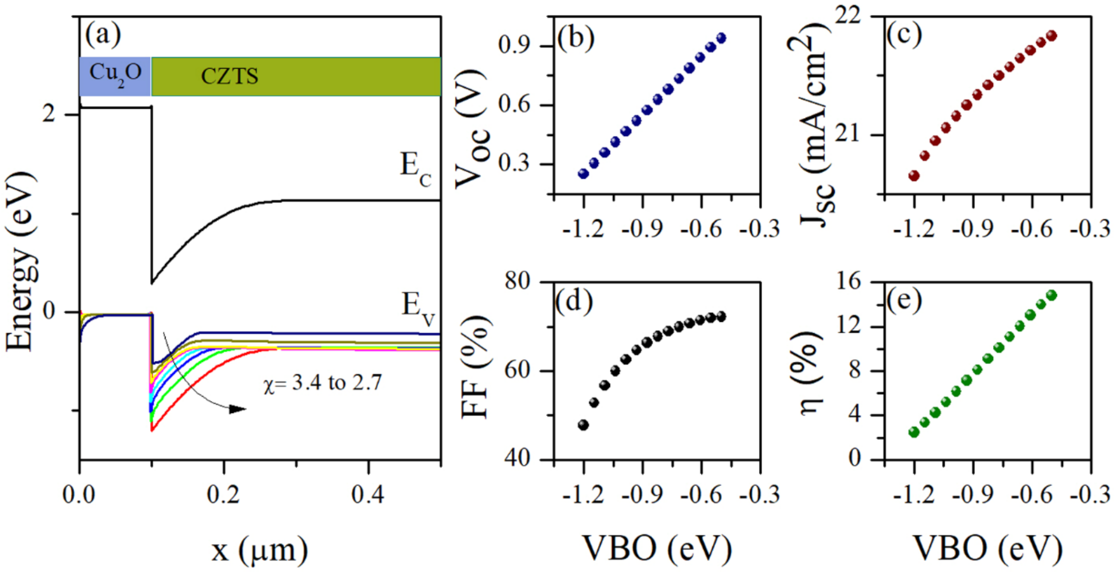

Fig. 3.8: (a) Position of band edges across the device having a Cu_2O BSF layer showing the VBO for different values of electron affinity of the Cu_2O layer; Variation in (b) Open circuit voltage V_{OC}, (c) short circuit current density J_{SC}, (d) Fill Factor FF and (e) efficiency η of the device as a function of VBO at back contact.

Further optimization of the device performance was carried out by investigating the role of thickness and acceptor density of the Cu_2O layer. The layer thickness was varied from 10 to 100 nm and the acceptor density was varied from 1×10^{18} to 1×10^{22} cm^{-3} keeping other parameters constant (as listed in Table 3.1). The results are summarized in Fig. 3.9.

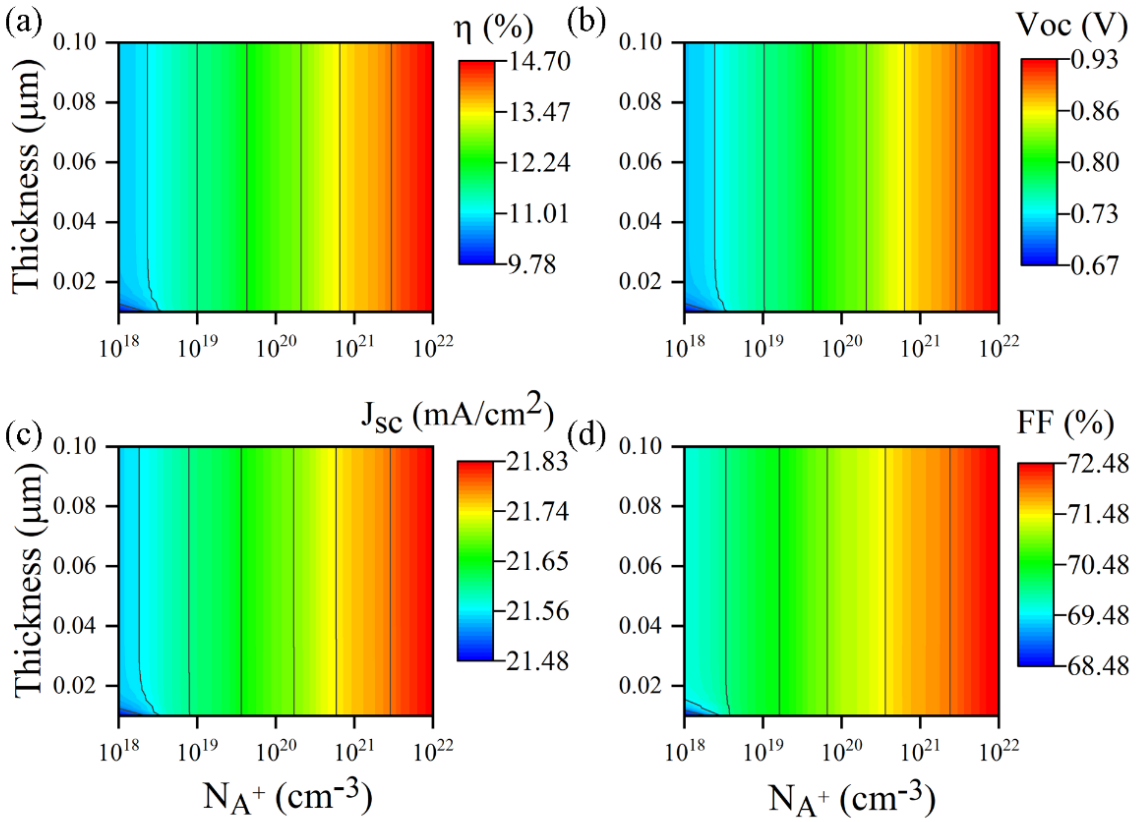

Fig. 3.9: Contour diagram showing dependence of (a) efficiency η, (b) Open circuit voltage V_{OC}, (c) short circuit current density J_{SC} and (d) Fill Factor FF of the device on acceptor concentration (N_{A+}) and thickness of the Cu_2O BSF layer.

As revealed in the figure (Fig. 3.9), the acceptor density N_{A+} strongly affected the device performance whereas the variation in thickness had little impact. Thickness of the BSF Cu_2O layer (up to 30 nm) played a role only when N_{A+} was in the range of 10^{18} to 10^{19} cm^{-3}. Beyond this range, the thickness did not affect the device performance. On the other hand, with increase in acceptor density of the BSF layer (Cu_2O film) the performance metrics increased significantly. With N_{A+} of 10^{22} cm^{-3}, the open-circuit voltage V_{OC} was greatly enhanced to 0.9290 V, J_{SC} to 21.83 mA/cm^2 and efficiency to 14.70%. The reason for this enhancement is understood to have originated from the enhanced gradient in hole concentration at the p+-p junction due to which the strength of field at this junction increased. As mentioned earlier, this field acted as a barrier for electrons and thus, prevented the electron-holes recombination at the back contact resulting in an effective enhancement in collection of charge carriers of the device (Park et al., 2018; Liu F. et al., 2014, Bar et al., 2008; Dasa et al., 2012; Roos, 1978).

Table 3.3: Material properties of Cu_2O and SnS layer used for simulation

layer properties	Cu_2O (Gupta et al., 2018)	SnS (Omrani et al., 2018)
Thickness (μm)	0.10	0.10
Bandgap (eV)	2.1	1.3
Electron affinity (eV)	3.2	4.2
Dielectric permittivity (relative)	7.1	12.5
CB effective density of states ($\times 10^{18}$1/cm^3)	2.50	10.00
VB effective density of states ($\times 10^{19}$/cm^3)	1.50	4.13
Electron thermal velocity ($\times 10^7$cm/s)	1.00	1.00
Hole thermal velocity ($\times 10^7$cm/s)	1.00	1.00
Electron mobility ($\times 10^1$ cm^2/Vs)	20.00	2.50
Hole mobility ($\times 10^1$ cm^2/Vs)	8.00	1.00
Donor density (1/cm^3)	0	0
Acceptor density ($\times 10^{18}$/cm^3)	5.00	3.00

3.2.3.2 SnS as BSF layer

Similar to the case of Cu_2O presented in the previous section, we have next studied the impact of SnS BSF layer in the CZTS based devices. Earlier, Ren et al. have experimentally shown that the presence of a thin SnS layer at the rear CZTS is beneficial for the performance of CZTS solar cells (Ren et al., 2017; Garain et al., 2021). We have performed simulations to identify the role of SnS layer in the reported enhanced performance of the devices. The results are depicted in Fig. 3.10. Figure 3.10a shows the energy band diagram of the CZTS solar cell with a 100 nm thick SnS as BSF layer with acceptor density of 3.0×10^{18} cm^{-3}.

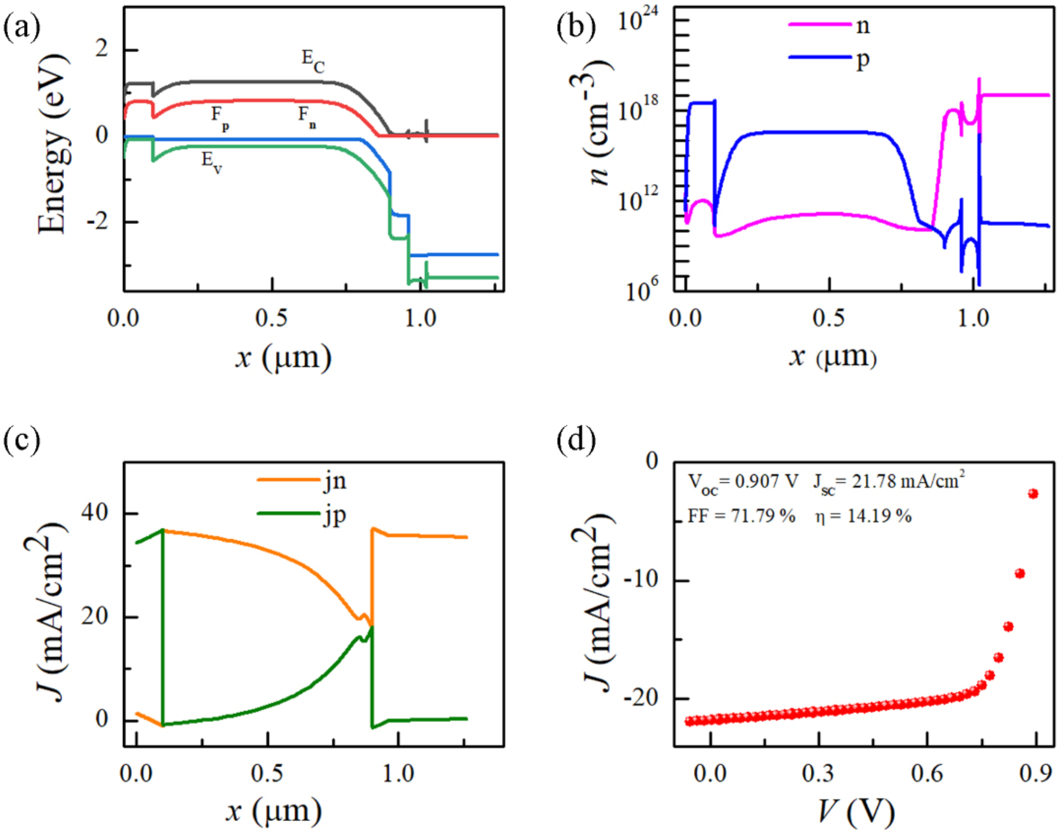

Fig. 3.10: (a) Position of band edges, and distribution of (b) carrier concentration *n* and (c) current density *J* across the device having a SnS BSF layer. The parameter *x* indicates the distance from the surface of the Mo film (i.e., x = 0 indicates the Mo film surface). A valence band offset VBO of -0.5 eV at SnS/CZTS interface was estimated in (a); (d) Current density *J* vs *V* characteristics of the simulated device.

Compared to Cu_2O, owing to favourable bandgap and electron affinity, the SnS layer introduced a smaller band offset (i.e., negative VBO of -0.5 eV) at SnS/ CZTS interface and thus, an activation energy E_a of ~1.0 eV for recombination. With the introduction of this SnS layer, the V_{OC} was greatly enhanced to 0.9069 V and the efficiency increased to 14.19%, which is better than that obtained with the Cu_2O layer. This can be attributed to the decrease in barrier height for the transport of holes towards back contact and the greater value of activation energy for recombinations (i. e., lower possibility of recombination) with the SnS layer compared to Cu_2O. It may be noted that at similar acceptor density (of ~10^{18} cm^{-3}) for both SnS and Cu_2O, the SnS BSF layer appears more effective, most likely due to efficient suppression of recombination at the rear contact of the device.

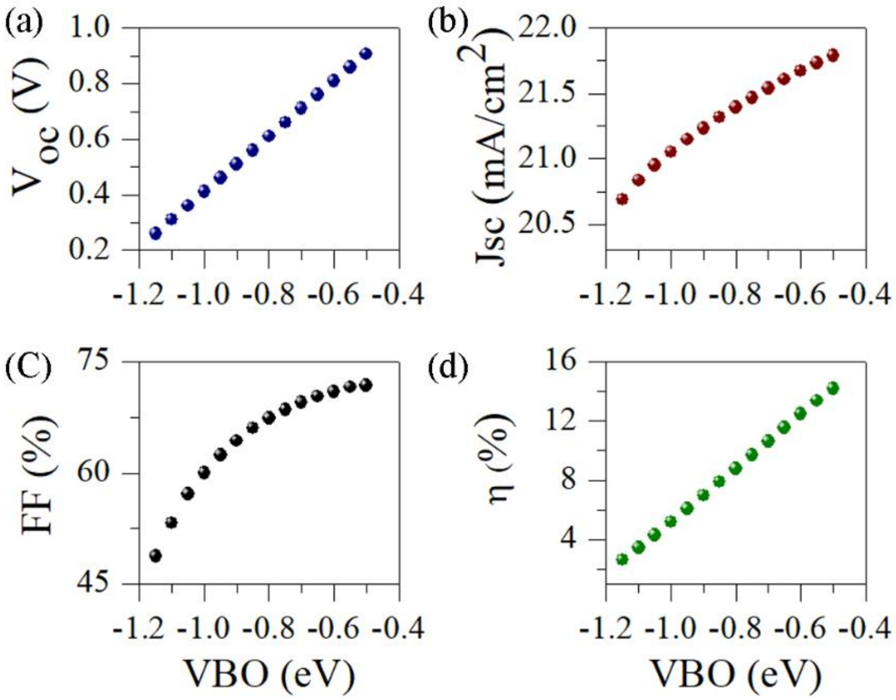

Fig. 3.11: Variation in (a) Open circuit voltage V_{OC}, (b) short circuit current density J_{SC}, (c) Fill Factor FF and (d) efficiency η of the device as a function of VBO at back contact using a SnS BSF layer.

We have next studied the impact of VBO in the CZTS based devices with a SnS BSF layer. The VBO was varied from -1.1 to -0.5 eV by varying the electron affinity value of SnS layer from 3.6 to 4.2 eV (in the convergence limit of the SCAPS package). The results are summarized in Fig. 3.11. It was observed that with the decrease in |VBO| from 1.1 to 0.5 eV, the V_{OC} increased from 0.26 to 0.90 eV resulting in efficiency enhancement from 2.63 to 14.18%. This enhancement is due to decrease in barrier for the flow of minority charge carriers at rear CZTS and increase in activation energy (0.2 eV to 0.8 eV) for recombinations, which reduced the back surface recombinations. Fig. 3.12 shows the contour plot of thickness and acceptor density dependence of device performance.

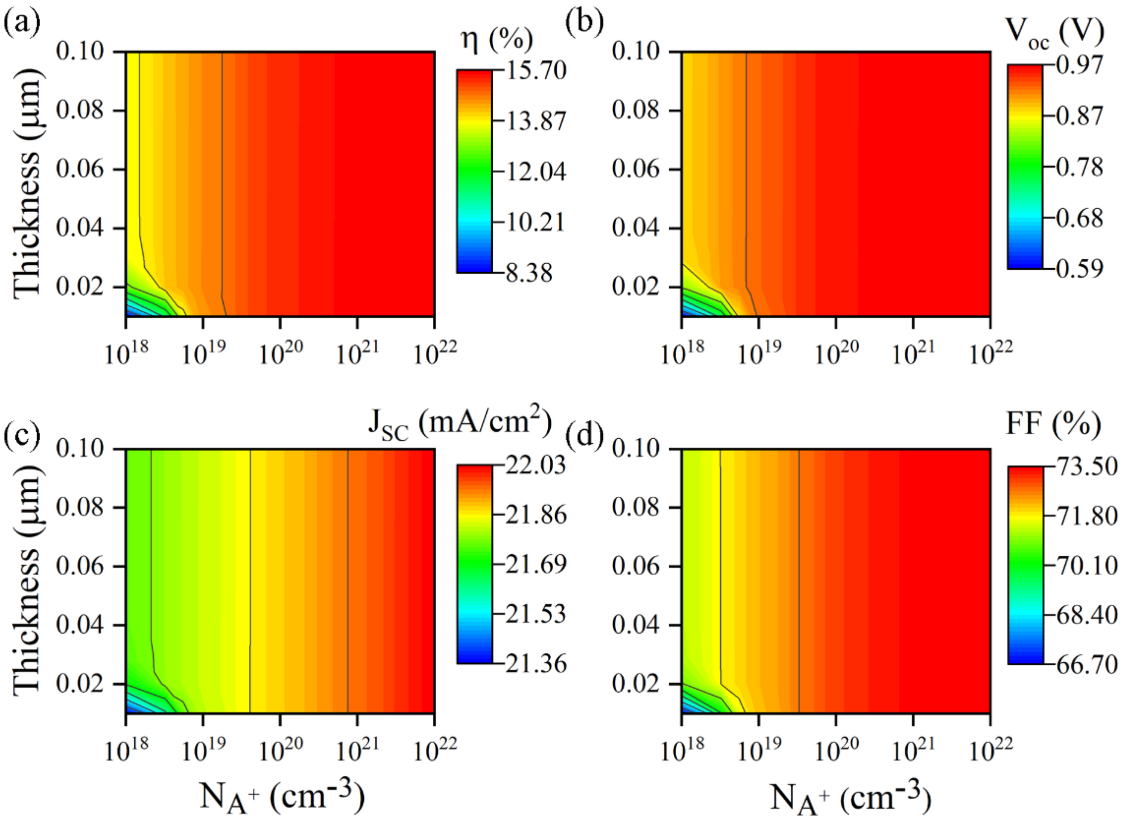

Fig. 3.12: Contour diagram showing dependence of (a) efficiency η, (b) Open circuit voltage V_{OC}, (c) short circuit current density J_{SC} and (d) Fill Factor FF of the device on acceptor concentration (N_{A+}) and thickness of the SnS BSF layer. The results show that efficiency as high as 15.70% can be achieved by engineering of the back contact interface.

Similar to the Cu_2O BSF layer (summarized in Fig. 3.9), the thickness of the SnS layer affected the performance in a limited range of acceptor concentration N_{A+} (10^{18}–10^{19} cm^{-3}). In this range of N_{A+} values, the efficiency increased with the increase in thickness. However, for thickness greater than 50 nm, the increase in efficiency became very small, suggesting that thickness of the BSF layer can be preferably be ≥50 nm. For N_{A+} values $>1 \times 10^{19}$ cm^{-3}, thickness does not affect the device performance. However, the increase in acceptor density of the SnS layer greatly enhanced V_{OC} to 0.97 V and efficiency of the device to 15.70%. This increase in V_{OC} is due to the increased concentration gradient between the p+ and p layer is because of increased built in potential of p+-p junction. This, in turn, resulted in effective charge separation and a cumulative increase in the efficiency of the device.

3.3 Simulation of CBTS based solar cell

As discussed in Chapter 1, Ba substitution in CZTS that yields Cu_2BaSnS_4 (CBTS) has been suggested to improve the cation ordering in the absorber layer. Improvement in the cationic ordering is expected to improve the device performance (Xiao et al., 2016; Shin et al., 2016). Although, the CBTS solar cells have shown very promising results in a short span of time, their performance is still inferior to that of the CZTS devices (Teymur et al., 2022). Yet, the details of charge collection mechanisms operational in the CBTS based devices are not clear. The impact of various material and junction properties including bulk and interface defect densities, band alignment at back and front contacts, etc. on the performance of the CZTS based devices has been studied numerically in detail (Houimi et al., 2021; Mazumder et al., 2022; Zhang et al., 2021). For instance, Haight et al. have shown that a spike-like band alignment at CZTS/CdS interface is more favourable in that it facilitates electron flow and minimizes recombination at the interface (Haight et al., 2011). Many groups have suggested the use of a BSF layer to reduce recombinations at the back interface (Giraldo et al., 2021; Minbashi et al., 2017; Omrani et al., 2018). In the previous sections (Section 3.2.1 and 3.2.2) while simulating the champion CZTS device (that demonstrated efficiency of ~11%), we found that such a performance would correspond to bulk defect density of order of 10^{15} cm^{-3} and interface defect density of ~10^{15} cm^{-2} and ~10^{14} cm^{-2} at CZTS/MoS_2 and CZTS/CdS interface, respectively. Similar numerical elucidation of CBTS devices is scarce in literature, although it is of high importance and can assist the experimentalists greatly. In particular, it is of huge interest to examine the resulting scenario in the CBTS based device with the defect densities, which have yielded the best performance in CZTS devices. We have investigated the CBTS solar cells by numerical simulation as outlined in Section 3.1.

3.3.1 Comparison with experimental champion device

For numerical investigation of the CBTS solar cell, bulk defect density of 10^{15} cm^{-3} and interface defect density of ~10^{15} cm^{-2} and ~10^{14} cm^{-2} at the CBTS/MoS_2 and CBTS/CdS interfaces are considered as initial conditions. It may be noted that these values of the defect densities are the same that have yielded the highest efficiency in the CZTS solar cells, as discussed in Section 3.2.2. The defect energy levels are considered to be located at 0.6 eV above the valance band maxima as reported by other researchers. Figure 3.13 shows the typical device structure with CBTS as an absorber layer.

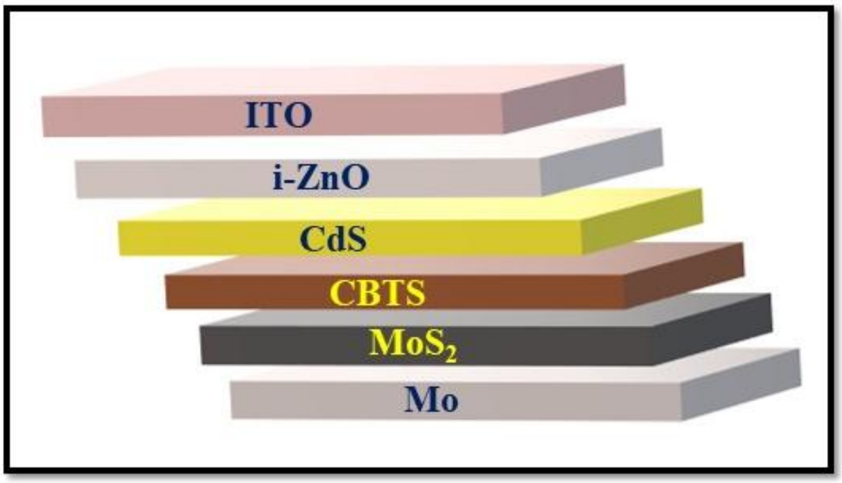

Fig. 3.13: Schematic view of the structure of the CBTS solar cell. A 300 nm thin MoS_2 layer is inserted between the CBTS layer and the Mo back contact for more realistic simulations.

The corresponding energy band diagram is presented in Fig. 3.14a, where x = 0 indicates the surface of the Mo back contact. A cliff-like CBO with the CdS window layer was observed since the conduction band minimum of CdS layer lies lower than that of the CBTS layer. The resulting current-voltage characteristic, depicted in Fig. 3.14d, reveals that for bulk defect density and interface defect densities (at MoS_2/CBTS and CBTS/CdS interfaces) same as those of CZTS devices (Section 3.2.1), the performance of the CBTS device is inferior. The values of η, Voc, Jsc and FF are reduced to 4.55%, 0.583 V, 12.3 mA/cm^2 and 63.3% for CBTS against the corresponding values of 11.0%, 0.73 V, 21.59 mA/cm^2 and 69.77% for CZTS. The reason for the observed degradation of the CBTS devices could be the changes in material properties compared to CZTS and the more detrimental effects of the defects that requires further studies. It may be noted that for the experimentally obtained champion CBTS thin film solar cell, η = 1.72% with Voc = 697.8 mV, Jsc= 5.25 mA/cm^2 and FF = 46.9% have been reported (Chen et al., 2018). The values of the defect densities, however, were not mentioned. Nevertheless, the lower performance compared to the simulated values (Fig. 3.14b) suggest poor collection of charge carriers.

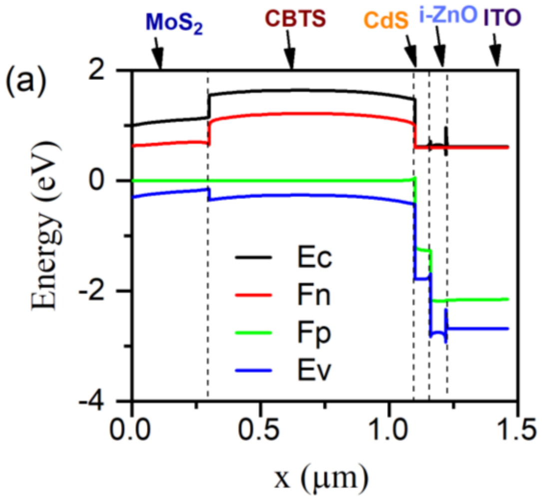

Fig. 3.14: (a) Energy band diagram of the CBTS thin film solar cell; x represents distance from surface of the Mo back contact, (b) J-V curve of the CBTS solar cell. Defect densities considered for the CBTS based device are similar to the ones that have yielded the highest efficiency for CZTS solar cells (Section 3.2.1).

3.3.2 Role of bulk and interface defect densities

Figure 3.15 presents the impact of variation in the defect density at the MoS_2/CBTS interface ($N_{MoS_2/CBTS}$) and bulk defect density in CBTS (N_{CBTS}) on performance metrics of the device. As noted from the figure, the performance parameters of the device was dependent on N_{CBTS} and remained unaffected by the variation in the MoS_2/CBTS interface defect density. For N_{CBTS} up to 10^{16} cm^{-3}, there was no noticeable change in the performance of the device. However, η, Voc, Jsc and FF significantly deteriorated for values of $N_{CBTS} > 10^{16}$ cm^{-3}. For instance, for increase in N_{CBTS} from 10^{16} to 10^{20} cm^{-3}, η decreased from 4.6% to 0.02%, Voc from 0.58 to 0.25 V, Jsc 12.4–0.25 mA/cm^2 and FF from 63.7% to 25.3%. This reduction could be attributed to the decrease in lifetime of the charge carriers with increase in defect density and thus, increase in recombinations of the photogenerated charge carriers (Gupta et al., 2018).

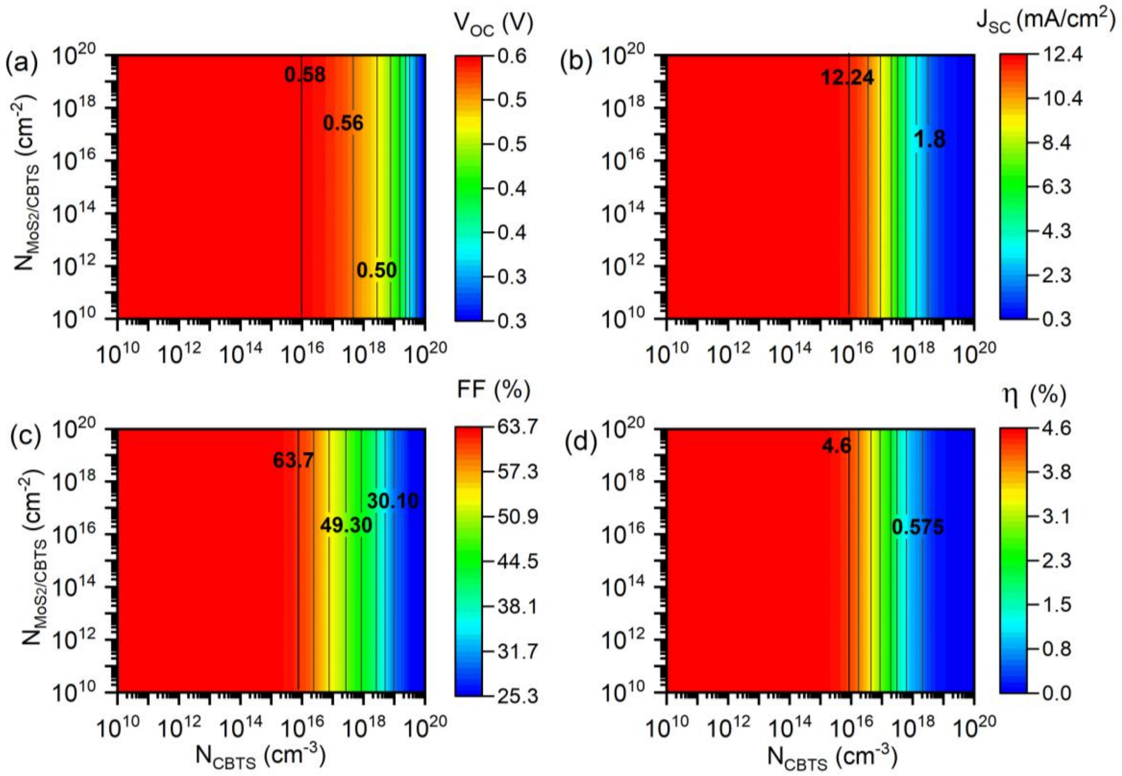

Fig. 3.15: Contour plots representing the effect of the defect density at the MoS_2/CBTS interface ($N_{MoS_2/CBTS}$) and bulk defect density (N_b) in CBTS on (a) open circuit voltage (V_{oc}), (b) short circuit current density (J_{sc}), (c) Fill factor (FF) and (d) efficiency (η) of the CBTS based solar cell.

On the other hand, the device performance, which was nearly independent of defect density at the MoS_2/CBTS interface (Fig. 3.15), was sensitive to the variation in density of defects at the other interface, i.e., CBTS/CdS (N_{CBTS}/CdS). As seen from contour plots in Fig. 3.16, increase in either $N_{CdS/CBTS}$ or bulk defect density N_{CBTS} deteriorated the device performance. $N_{CdS/CBTS}$ mainly degraded the performance effectively for its value between 10^{10} to 10^{14} cm^{-2} and negligibly affected device parameters from 10^{14} to 10^{20} cm^{-2}. For instance, for $N_{CBTS} = 10^{15}$ cm^{-3} , V_{oc} decreased from 0.760 to 0.583 V and J_{sc} from 14.0 to 12.30 mA/cm^2 for the increase in $N_{CdS/CBTS}$ from 10^{10} to 10^{14} cm^{-2} and both remained the same for further increase in $N_{CdS/CBTS} > 10^{14}$ cm^{-2}. Correspondingly, the efficiency decreased from 6.93% to 4.58% and remained constant for the increase in $N_{CdS/CBTS} > 10^{14}$ cm^{-2}. It shows that the rise in interface defect density has more pronounced effect on V_{oc} (~30% fall) than on J_{sc} (~13% fall), which is consistent with earlier reports on thin film solar cells (Wilhelm et al., 2011; Minemoto et al., 2001). The possible reason for the reduction in the V_{oc} has been explained by Wilhelm et al. on the basis of interface recombination rate (Wilhelm et al., 2011). Using the modified

SRH recombination rate equation, they have suggested that the interface recombination rate is proportional to the surface recombination velocity of the corresponding charge carrier (electron/hole). This velocity has been shown to increase with increase in the interface defect density. Thus, an increase in the defect density at interface causes an rise in the recombination rate and lowers the Voc. On the other hand, an increase in N_{CBTS} beyond 10^{16} cm^{-3} was found to cause a rapid fall in efficiency due to fast deterioration in J_{sc} and V_{oc}. For instance, at $N_{CdS/CBTS} = 10^{14}$ cm^{-2} , increasing N_{CBTS} from 10^{16} to 10^{20} cm^{-3} caused V_{oc} to decrease from 0.580 to 0.254 V and J_{sc} from 11.87 to 0.29 mA/cm^2 and the efficiency decreased from 4.2% to 0.02%. As expected, the decrease in Jsc is due to the increase in bulk defect density, which affects charge carrier transport in the quasi-neutral region (Chowdhury et al., 2020).

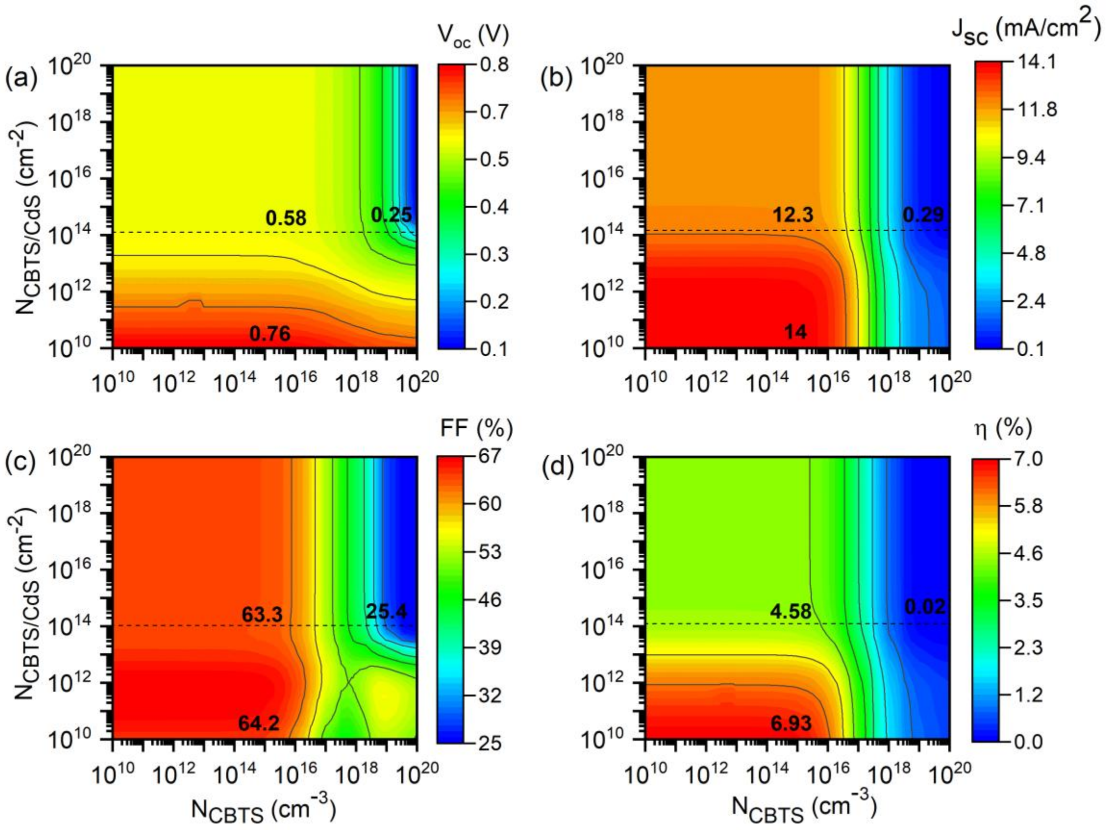

Fig. 3.16: Contour plots representing the effect of the defect density at the CBTS/CdS interface ($N_{CBTS/CdS}$) and bulk defect density (N_b) in CBTS on (a) open circuit voltage (V_{oc}), (b) short circuit current density (J_{sc}), (c) Fill factor (FF) and (d) efficiency (η) of the CBTS based solar cell.

The above results (Fig. 3.15 and Fig. 3.16), therefore, define the performance window of the CBTS based device with respect to the bulk and interface defect densities. For the device to yield better performance, $N_{CdS/CBTS}$ should be as low as possible with a N_{CBTS} value $\leq 10^{16}$ cm^{-3}. The maximum efficiency of 6.9% was achieved, for example, with the interface defect densities $N_{MoS2/CBTS} \sim 10^{15}$ cm^{-2}, $N_{CdS/CBTS} \sim 10^{10}$ cm^{-2} and bulk density $N_{CBTS} \sim 10^{14}$ cm^{-3} as shown in Fig. 3.17. The value of V_{oc}, J_{sc} and fill factor are 0.7615V, 14.05mA/cm^2 and 64.83% respectively.

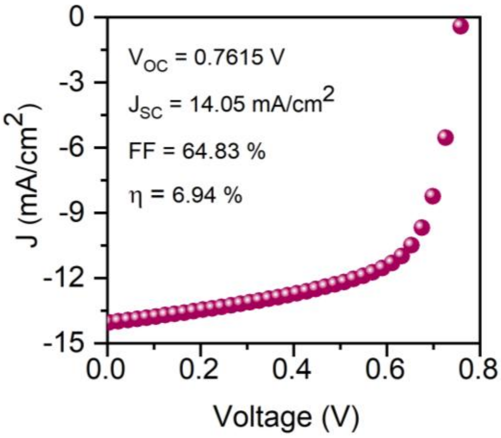

Fig. 3.17: J-V characteristics of the CBTS device with the optimized values of bulk defect density of CBTS and interface defect densities showing an efficiency of 6.9%.

In thin film photovoltaics, the loss of device efficiency has been traditionally correlated to various recombinations at the interfaces and in the bulk of the absorber layer (Sravani et al., 2021; Chen et al., 2019). For example, deep defects, which lie within the quasi Fermi levels, capture holes and become active centers for recombination of electrons and holes that reduces devices performance (Simmons et al., 1971). Hence, for more insight, we have studied the role of radiative and Auger recombinations (Chantana et al., 2021) in the present device. Radiative recombinations are typically prevalent in direct bandgap semiconductors and the radiative recombination coefficient B_r has dependence on carrier density, temperature and atomic structure (Zhang et al., 2018). Figure 3.18 shows the effect of variation in B_r on the device performance metrics. As observed from the figure, an increase in B_r led to deterioration in all performance metrics. The highest deterioration, however, was observed in Jsc. The values of Voc and FF remained constant at ~0.76 V and 65% till the $B_r \approx 10^{-7}$ cm^3/s and decreased thereafter. The V_{oc} decreased from 0.760 to 0.694 V for increase in B_r from 10^{-7} to 10^{-1} cm^3/s whereas J_{sc} decreased from 13.99 to 4.34 mA/cm^2. Overall, the efficiency was greatly reduced from 6.56% to 1.14% for increase in B_r from 10^{-7} to 10^{0} cm^3/s. Therefore for better device performance B_r should be less than 10^{-7} cm^3/s.

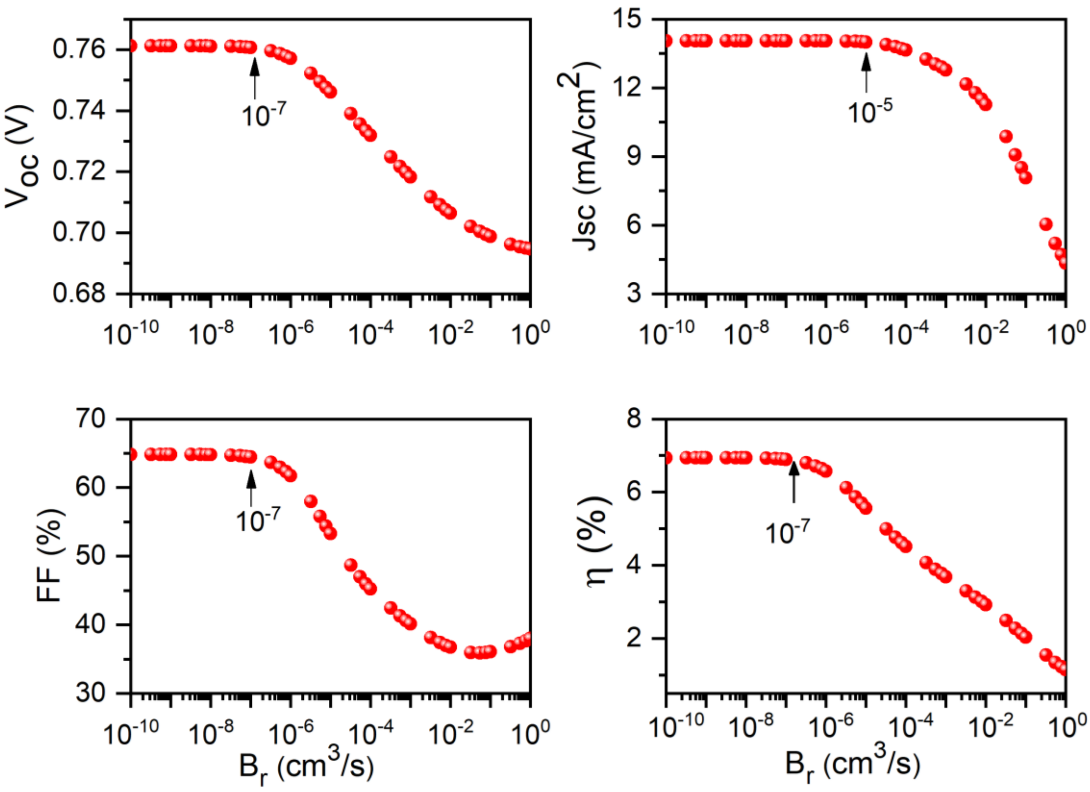

Fig. 3.18: Effect of increase in radiative recombination coefficient (Br) on performance metrics of the CBTS solar cells. The efficiency (η) degraded fast for value of $B_r > 10^{-7}$ cm^3/s.

While the radiative recombination deals with an electron and a hole, Auger recombination involves interaction of three particles via either *eeh* or *ehh* process (Chantana et al., 2021). An electron out of conduction band recombines with a hole from valence band and transfer the excess energy to another free electron or hole depending whether it is *eeh* or *ehh,* respectively. The recombination rate for *eeh* and *ehh* processes are given by (Kerr et al., 2022),

$$R_{eeh} = A_e n^2 p \quad R_{ehh} = A_h p^2 n \qquad \ldots (3.3)$$

where p and n are holes and electrons concentration, and A_e and A_h are Auger electron and hole recombination coefficients. Correspondingly, the Auger lifetime for a p-type material can be given as $\tau_{hi} = \frac{1}{(A_e + A_h)\Delta n^2}$, where Δn is the excess carrier density. For CZTS, Auger electron and hole recombination coefficients are considered to be ~10^{-24} and ~10^{-29} cm^6/s, respectively (Sravani et al., 2021). We have simulated the device efficiency as a function of independently varied Auger electron and hole recombination coefficients (i.e., A_e and A_h). Fig. 3.19 shows the dependence of device performance metrics on the Auger recombination coefficients. For the lower values of A_e and A_h, V_{oc}, J_{sc} and FF (and hence, η) remained constant and decreased gradually with increase in the values of the coefficients. It may be noted that the onset of decrease in the device parameter occurs for lower values of A_h and is delayed by three orders of magnitude for the Auger electron coefficients. For example, the onset of decrease in V_{oc} occurred for $A_h \sim 10^{-22}$ cm^6/s whereas that for the Auger electrons was at $A_e \sim 10^{-19}$ cm^6/s. For J_{sc}, the onset of decrease occurred at $A_h \sim 10^{-19}$ cm^6/s and $A_e \sim 10^{-16}$ cm^6/s. As noted from the figure, the efficiency remained constant at 6.9% for low values of the coefficients (up to $A_h \sim 10^{-22}$ cm^6/s and $A_e \sim 10^{-19}$ cm^6/s) and decreased gradually thereafter. Thus, it is desirable that A_h remains less than 10^{-22} cm^6/s and A_e be $< 10^{-19}$ cm^6/s for better device performance (Zhang et al., 2018).

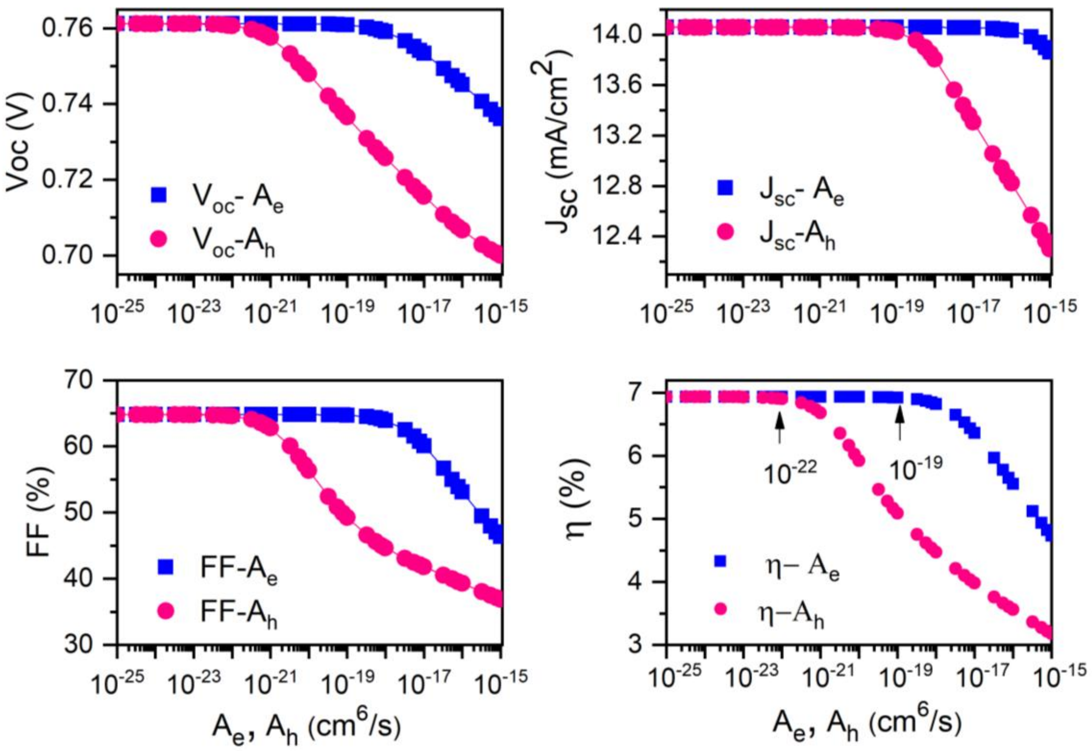

Fig. 3.19: Effect of increase in coefficient of Auger electron (A_e) and Auger hole (A_h) on performance metrics of the CBTS solar cells. Arrows in indicate the critical values of A_e and A_h, beyond which the efficiency falls rapidly.

In typical thin film solar cells, thickness of the absorber layer has been shown to be a very important parameter (Lundberg et al., 2003; Yadav et al., 2022). The impact of absorber thickness on performance metrics of the device is shown in Fig. 3.20. Apparently, V_{oc} showed little dependence of the absorber layer thickness as evident from its marginal increase from 0.74 to 0.76 V for increase in thickness of the CBTS layer from 0.3 to 2 μm. On the other hand,

J_{sc} and FF showed strong positive dependence on thickness. For instance, the Jsc and FF increased from 10.2 to 15.62 mA/cm^2 and from ~ 57 to about 72%, respectively for the same variation in thickness. Consequently, there was considerable improvement in device efficiency from 4.37% to 8.64%. It appears that the increase in thickness of the CBTS absorber layer facilitated absorption of more number of photons, and thereby, increased the photogenerated current and the device performance (Hattab et al., 2021; Chelvanathan et al., 2010).

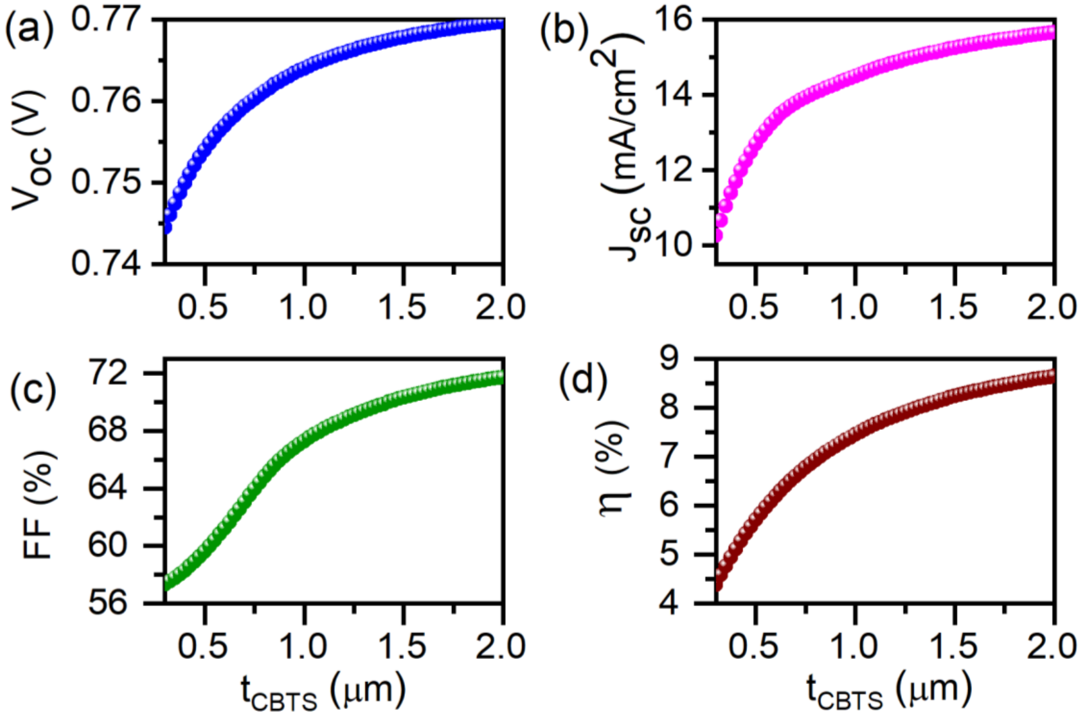

Fig. 3.20: Effect of variation in thickness of the CBTS layer (t_{CBTS}) on (a) open circuit voltage (V_{oc}), (b) short circuit current density (J_{sc}), (c) Fill factor (FF) and (d) efficiency (η) of the CBTS based solar cell.

In materials like CBTS, the intrinsic p-type conductivity arises due to various point defects such as Cu-vacancies, interstitials and antisites (Xiao et al., 2017). Hence, the acceptor concentration N_A assumes much significance in the device performance. The acceptor concentration dependence of V_{oc} and J_{sc} is depicted in Fig. 3.21. The V_{oc} increased gradually to ~0.76 V with increasing N_A in the range of 10^{13} to 10^{16} cm^{-3} and thereafter decreased sharply. On the other hand, J_{sc} remained constant at about 14.6 mA/cm^2 for values of N_A up to 10^{15} cm^{-3} and thereafter decreased rapidly. Consequently, a maximum efficiency of ~6.9% was obtained for N_A ~10^{15} cm^{-3} (Fig. 3.21c). The fall in J_{sc} is in concurrence with the fact that increase in acceptor concentration results in a reduction in lifetime of minority charge carriers causing more recombinations and lowering the probability of carrier collection. Besides, with increasing N_A, depletion region width in the CBTS absorber layer decreases. As noted earlier, shorter depletion region indicates diffusion-limited movement of the carriers in the quasi-neutral regions, which might increase the recombination rate and lower J_{sc} (Moustafa et al., 2022).

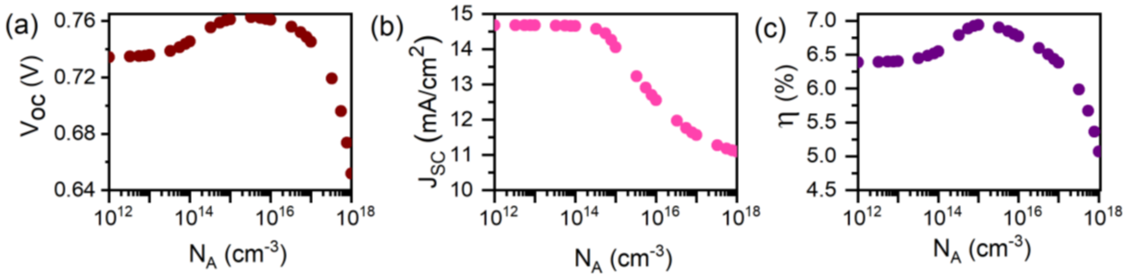

Fig. 3.21: Effect of variation in carrier concentration, N_A of CBTS on (a) open circuit voltage (V_{oc}), (b) short circuit current density (J_{sc}) and (c) efficiency (η) of the CBTS based solar cell**.**

In the p-n semiconductor junction based photovoltaic devices, the exciton dissociation is caused by the built-in field at the junction and the electrons/holes are collected at opposite electrodes. The performance of the device is, hence, critically dependent not only on how the electron-hole pair dissociates but also on how charge carriers are transported in the p and n-layers (Wang et al., 2014). Thus, apart from the absorber layer, the device performance is strongly affected by the band offset at the interface, thickness and donor concentration of the n-layer (here, a CdS thin film), etc. The optimum thickness of the CdS layer has been found to be about 50 nm, both experimentally and theoretically (Lee et al., 2015; Neuschitzer et al., 2015) in the case of CIGS and CZTS thin film solar cells. Keeping the thickness of the CdS layer at 50 nm, we have investigated the effects of variation in carrier concentration N_D of the CdS film and the band alignment between the CBTS and CdS layers. Figure 3.22 shows the variation in performance metrics with increasing carrier concentration N_D of the CdS layer. Increase in N_D is expected to move the n-type quasi-Fermi level closer to conduction band, which in turn enhances the band bending and concentration gradient between the p (CBTS) and n (CdS) layers. This results in an increased built-in voltage and enhanced charge carrier collection (Bouarissa et al., 2021). Indeed, with increase in N_D, there was increase in V_{oc} from 0.60 to 0.99 V, in J_{sc} from 13.55 to 14.36 mA/cm^2 and in FF from 58.0 to 65.51%. Consequently, efficiency is increased from 4.50 to 9.40%. It is worth mentioning here that achieving the carrier concentration of CdS thin films of ~ 10^{22}/cm^3 is extremely difficult experimentally. The simulation performed in this work is intended to demonstrate the trend in the variation in device performance with carrier concentration of CdS and a value of 10^{22}/cm^3 may indicate the upper limit.

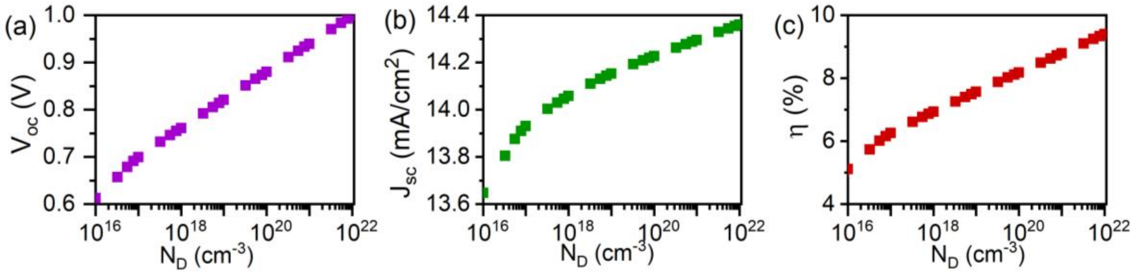

Fig. 3.22: Effect of variation in carrier concentration of the CdS buffer layer on (a) open circuit voltage (Voc), (b) short circuit current density (Jsc) and (c) efficiency (η) of the CBTS based solar cell.

As mentioned above, the band alignment influences the current transport across the junction and hence, the performance of the device. Experimentally, many researchers have attempted to improve the device efficiency by tuning conduction band offset (CBO) at the absorber/buffer interface by various methods such as KCN-etching of absorber layer, pre-deposition of buffer layer, varying the stacking order in sputtering CZTS thin films, post-heat treatment of absorber/buffer heterojunction, etc. (Bar et al., 2011; Liu et al., 2019). The CBO at the CBTS-CdS junction can be calculated from the difference of electron affinities of the CBTS and CdS layers. Depending on the positive or negative value of CBO, the interface will have a 'spike like' or 'cliff like' configuration. From the band diagram of the CBTS-CdS junction based device, a cliff like offset at this junction is observed, whose magnitude can be varied by changing the electron affinity of CdS layer χ_{CdS}. Therefore, χ_{CdS} was varied from 4.0 to 5 eV (convergence limit in this range only) as shown in Fig. 3.23.

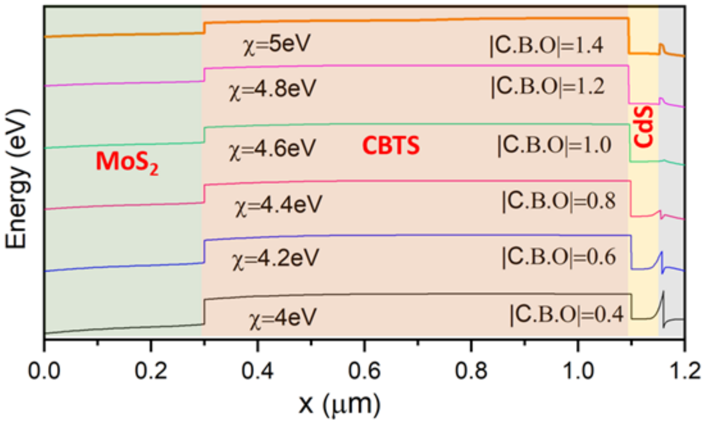

Fig. 3.23: Variation in CBO at CBTS/CdS interface of CBTS solar cell for electron affinity varied from 4 to 5eV. It can be seen that with increasing electron affinity, the magnitude of the CBO increases.

It can be seen that increasing the electron affinity resulted in the decrease in the CBO from -0.4 to -1.4 eV. The negative value of CBO in the considered range of χ_{CdS} suggests a cliff like interface (Minemoto et al., 2015). The impact of χ_{CdS} on V_{oc}, J_{sc} and η is depicted in Fig. 3.24.

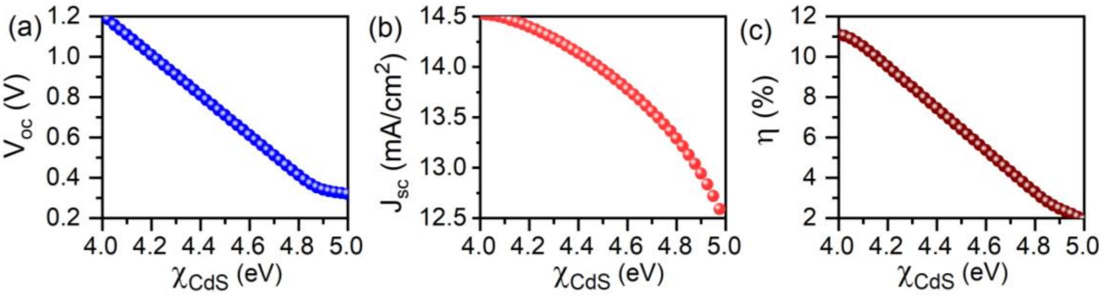

Fig. 3.24: Effect of electron affinity of the CdS layer (χ_{CdS}) on (a) open circuit voltage (Voc), (b) short circuit current density (Jsc) and (c) efficiency (η) of the CBTS based solar cell. The change in values of χ_{CdS} results in changes in the conduction band offset between the CBTS and CdS (Fig. 3.23).

It was found that with increase in χ_{CdS}, Voc greatly decreased from 1.20 to 0.31 V, whereas J_{sc} decreased marginally from 14.52 to 12.58 mA/cm^2. Correspondingly, the efficiency decreased from 11.10% to 1.91%. The fall in V_{oc} may be understood from the correlation between V_{oc} and the activation energy for recombination E_a given by $V_{oc}=\frac{E_a}{q}-\frac{AkT}{q}\ln\frac{j_{oo}}{j_{sc}}$, where q, k, A, T, j_{oo} and j_{sc} are electronic charge, Boltzmann constant, ideality factor, temperature, reverse saturation current and short-circuit current density. Activation energy for recombination is given by $E_a = E_{g,CBTS} - |CBO|$ and by varying χ_{CdS} from 4.0 to 5 eV, the activation energy for recombination decreased from 1.5 to 0.5 eV. This decrease in the activation energy presumably resulted in severe increase in the interface recombination and thus, significant reduction in V_{oc}. These results suggest that χ_{CdS} should be small (~4.0 eV) for an efficient current transport across the CBTS-CdS junction that may yield high efficient solar cells.

In Summary, we have numerically investigated the CZTS and CBTS thin film solar cells. In particular, the efficiency limited by various material properties was analysed and pathway to realize devices with efficiency much higher than the reported maximum value has been proposed. We have elucidated distinct role of defect densities at back and top interfaces and in the bulk of the absorber layers. It was found that the effect of bulk defect density is more profound compared to that due to the defects at MoS_2 and CdS interfaces. For the CZTS solar cells, we have shown that by introducing a highly doped p+ layer between the back contact Mo and the CZTS layer, efficiency can be improved. For instance, with introduction of a BSF Cu_2O layer, the efficiency increased from ~11.0 to 11.4% while the BSF SnS layer yielded an increase in efficiency to ~14.2%. More importantly, it is found that a higher concentration gradient at the p-p+ interface significantly lowered the open circuit voltage deficit ($E_g/q - V_{OC}$) and enhanced the efficiency remarkably. At optimized conditions, efficiency as high as 14.70% and 15.70% for Cu_2O and SnS, respectively, were obtained.

For the CBTS solar cells, the performance is severely deteriorated for bulk defect density > 10^{16} cm^{-3}. Intuitive manipulation of defect densities yielded an efficiency of 6.9% for $N_{MoS_2/CBTS} = 10^{15}$ cm^{-2}, $N_{CdS/CBTS} = 10^{10}$ cm^{-2} and $N_{CBTS} = 10^{14}$ cm^{-3}. The impact of the non-radiative recombination coefficient B_r, Auger electron (A_e) and hole recombination coefficient (A_h) has been explicitly studied, which revealed critical limits of 10^{-7} cm^3/s, 10^{-19} cm^6/s and 10^{-22} cm^6/s, respectively. Further improvement in performance of the device was achieved by optimizing carrier density of CBTS and CdS layers and facilitating current transport by tailoring the band alignment at the CBTS/CdS junction. The results suggest that device efficiency of about 11% can be obtained, which is a huge improvement over the current experimental champion cell of 6.2%.

CHAPTER 4

Growth and characterization of Cu_2BaSnS_4 (CBTS) thin films

In the previous chapter, it was shown that by optimizing the defect density at the interfaces and in the bulk, it may be possible to achieve 11% efficiency in contrast to the highest reported efficiency of ~6% for the CBTSSe based thin film solar cells (Teymur et al., 2022a). However, experimental realization of the same will be very challenging due to typical complexities involved in the synthesis of the CBTS film and device. Traditionally, solution based approaches for the synthesis of semiconducting thin films have been routinely preferred due to their distinct advantages. However, there have a been a number of issues in the fabrication of phase pure CBTS films by a solution method due to poor solubility of the Ba salts and formation of secondary phases such as Cu_2SnS_3, CuS and $BaSO_4$ (Teymur et al., 2018). The survey of literature on formation of CBTS thin films by solution based methods is presented in Chapter 1. One can find that despite interest on the fabrication of CBTS based thin films, studies enlightening the phase evolution mechanism and possible methods to mitigate unwanted secondary phases are scarce. In this chapter, the growth of single phase CBTS films and results of their detailed characterization are presented.

4.1 Evolution of CBTS phase

In this work, films were fabricated by sulfurization of the precursor films, which were deposited by spin coating of the precursor solution obtained by fully dissolving cation and anion salts. This method of dissolving at molecular-scale is considered to remove the long-range diffusion of precursors and provide explicit control of stoichiometry (Miller et al., 2012; Todorov et al., 2020). The details of synthesis of the film are outlined in chapter-2. Briefly, two solutions were prepared: Solution A contains salts of Cu, Sn and S while Solution B contains Ba salt. Cu solution is blue in colour and it turns milky when Sn is added to it. After adding thiourea, a clear transparent yellow solution of Cu-Sn-S is obtained. The solution containing Ba is a clear transparent solution, which when mixed with Cu-Sn-S solution, resulted in clear transparent pale-yellow solution. Fig. 4.1a shows the actual photographs at various stages of the making of the solution. The precursor films were dried at 270 ˚C on hot plate during spin coating process. The drying temperature was chosen from a TGA analysis of the powder prepared by drying the precursor solution at 90 ˚C for 12 hours. Figure 4.1 b shows a representative TGA curve of a powder prepared by drying of the precursor solution containing salts of stoichiometric ratio ([Cu]:[Ba]:[Sn]:[S] = 2:1:1:4). Sharp weight loss was observed for the temperature range from 150 to 270 ˚C, which corresponds to the decomposition of metal-thiourea complexes (Gokmen et al., 2013). Beyond 270 ˚C, there was a slow gradual decrease in the weight loss, possibly due to oxidation of intermediate sulphides. Therefore, the drying temperature for the spin-coated film was chosen to be 270 ˚C to make precursor film in order to ensure the metal-thiourea complex decomposition and to avoid sulphide oxidation (Chen et al., 2018).

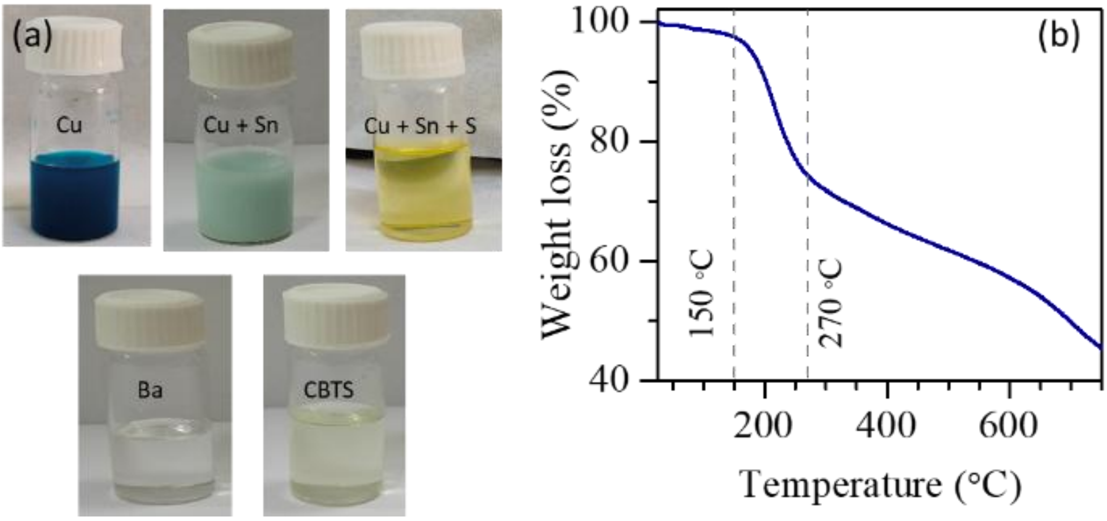

Fig. 4.1: (a) Photographs of vials containing different solutions. The Ba solution was prepared separately and was added to the solution that contained Cu, Sn and S; (b) Typical TGA curve of a powder prepared by drying of the precursor solution containing salts of stochiometric molar ratio (i.e., Cu:Ba:Sn:S = 2:1:1:4) at 90 °C for 12 hours.

The precursor films were sulfurized in a tubular furnace at 500, 550 and 575°C for 30 min with 0.5 g of S in a silica crucible in flowing argon. The typical XRD pattern of the films prepared from precursor solution with stoichiometric molar ratio Cu:Ba:Sn:S = 2:1:1:4 are presented in Fig. 4.2. For comparison, reference patterns of $BaSO_4$ (JCPDS file: 01–072–1378) and Cu_2SnS_3 (JCPDS file: 01–027–0198) are also given. Analysis of the patterns showed the formation of two phases, viz., $BaSO_4$ and Cu_2SnS_3 irrespective of the sulfurization temperature. The formation of Cu_2SnS_3 phase has been frequently observed during the growth of CZTS thin films, possibly due to poor reaction with the zinc sulfide during the sulfurization stage (Johnson et al., 2015).

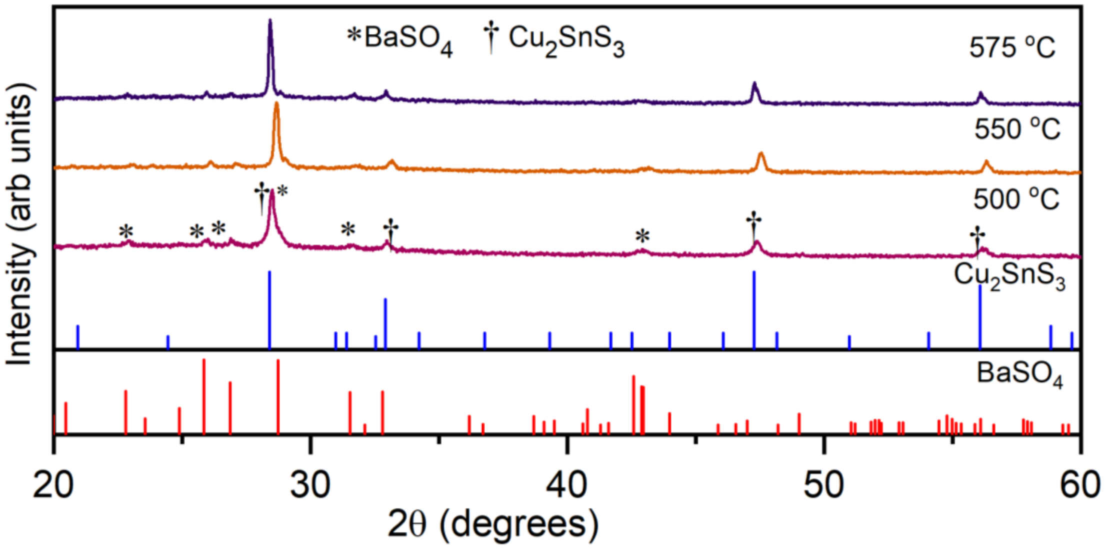

Fig. 4.2: Typical XRD pattern of the films prepared by sulfurization of the precursor films at different temperatures for 30 min with 0.5 g of S in a silica crucible in flowing argon. The precursor film was prepared from solution containing salts of stoichiometric molar ratio (i.e., Cu:Ba:Sn:S = 2:1:1:4). The bottom two panels show the reference patterns for $BaSO_4$ and Cu_2SnS_3.

The presence of $BaSO_4$ during the growth of CBTS films has been reported recently (Teymur et al., 2021; Teymur et al., 2018; Teymur et al., 2022 b). It is believed that the $Ba(OOCCH_3)_2$, used as Ba-source in this work, decomposes as per reactions (4.1- 4.2) (Hong et al., 2015; Afzal et al., 1991) to yield BaO, which reacts with S during sulfurization to produce $BaSO_4$ (Teymur et al., 2018)

$$Ba(OOCCH_3)_2 \longrightarrow BaCO_3 + (CH_3)_2CO \qquad (4.1)$$

$$BaCO_3 \longrightarrow BaO + CO_2 \qquad (4.2)$$

On the other hand growth of the Cu_2SnS_3 phase could be due to excess Cu in the film (as indicated by a strong XRD peak at about 28.4° in Fig. 4.2 that inhibits the formation of the CBTS phase. However, decreasing the Cu concentration in the solution alone, i.e., reducing the [Cu]/([Ba]+[Sn]) value did not help in the growth of the CBTS phase. The XRD patterns of the films (Fig. 4.3) grown from a solution with [Cu]/([Ba]+[Sn]) <1.0 and sulfurized at 500 °C for 30 min with 0.5 g of S revealed the presence of $BaSO_4$ (JCPDS file: 01–072–1378), Cu_2SnS_3 (JCPDS file: 01–027–0198) and Cu_2S (00–002–1272) phases. It is interesting to note that compared to the films grown with [Cu]/([Ba]+[Sn]) = 1.0 (shown in Fig. 4.2), the intensity of the peak corresponding to the $BaSO_4$ and Cu_2S phases increased with the decrease in the [Cu]/([Ba]+[Sn]) value (i.e., for 0.9 and 0.8).

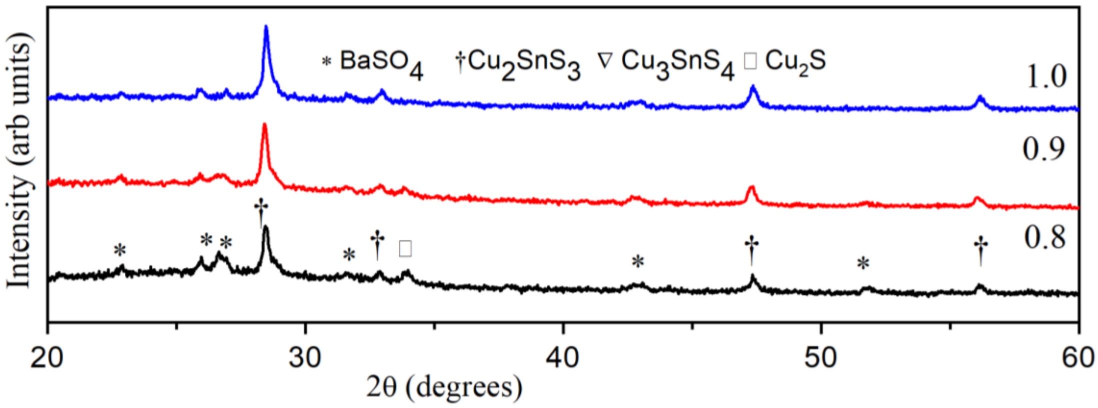

Fig. 4.3: Typical XRD pattern of the films prepared by varying [Cu]/([Ba]+[Sn]) ratio in the precursor solution keeping [Ba]/[Sn] = 1. All films were annealed at a temperature of 500 °C for 30 min in presence of 0.5 g of S. XRD pattern indicates that by changing [Cu]/([Ba]+[Sn]) in the precursor solution, the CBTS phase could not be obtained in the sulfurized film.

Issues of CBTS phase formation in the solution process have been reported earlier, wherein the [Ba]/[Sn] ratio was found to have a decisive impact on it (Teymur et al., 2021; Teymur et al., 2022b). We have therefore systematically varied the [Ba]/[Sn] ratio in the precursor solution and modified the sulfurization conditions to establish the reaction pathway. Fig. 4.4 a and b show typical XRD patterns of the films grown from precursor solutions with [Ba]/[Sn] = 1.2 and 1.3, respectively and sulfurized at different temperatures for 30 min with 0.5 g of S. The XRD pattern of the film grown at [Ba]/[Sn] = 1.2 was similar to that obtained for [Ba]/[Sn] = 1.0 for all temperatures. However, there were significant differences in the pattern for the film grown at [Ba]/[Sn] = 1.3. The pattern shows strong peaks corresponding to the $BaSO_4$ phase, especially for sulfurization at 575 °C. The peak intensity of the $BaSO_4$ phase (at ~25.88° and ~26.86°) was nearly same as that of the Cu_2SnS_3 phase (at ~28.44°). However, no peaks could be identified with the CBTS phase. Further attempts with increased sulfurization duration (for example, 60 mins) did not yield CBTS phase, although it enhanced the intensity of the $BaSO_4$ phase (Fig. 4.5).

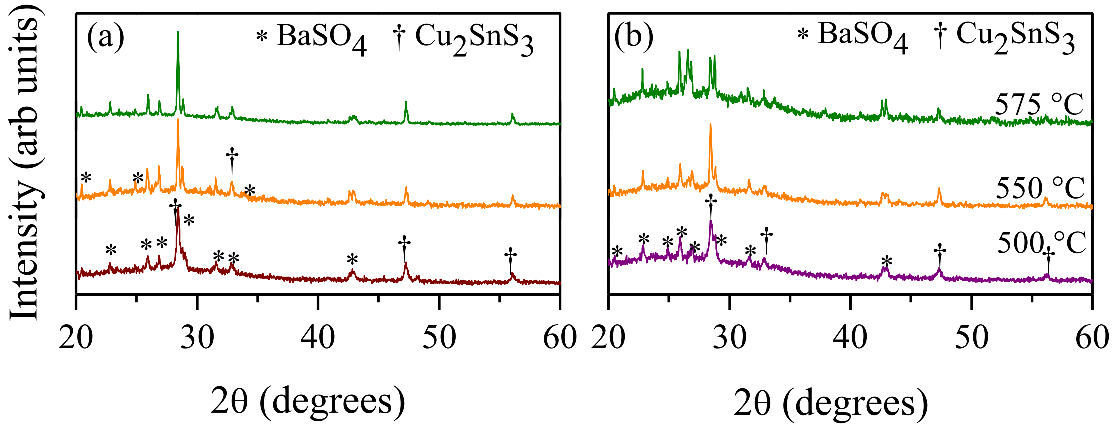

Fig. 4.4: Typical XRD patterns of the films grown from precursor solutions with (a) [Ba]/[Sn] = 1.2 and (b) [Ba]/[Sn] = 1.3, and sulfurized at different temperatures for 30 min with 0.5 g of sulfur. Note the significant changes in the pattern obtained for the film sulfurized at 575° C in (b).

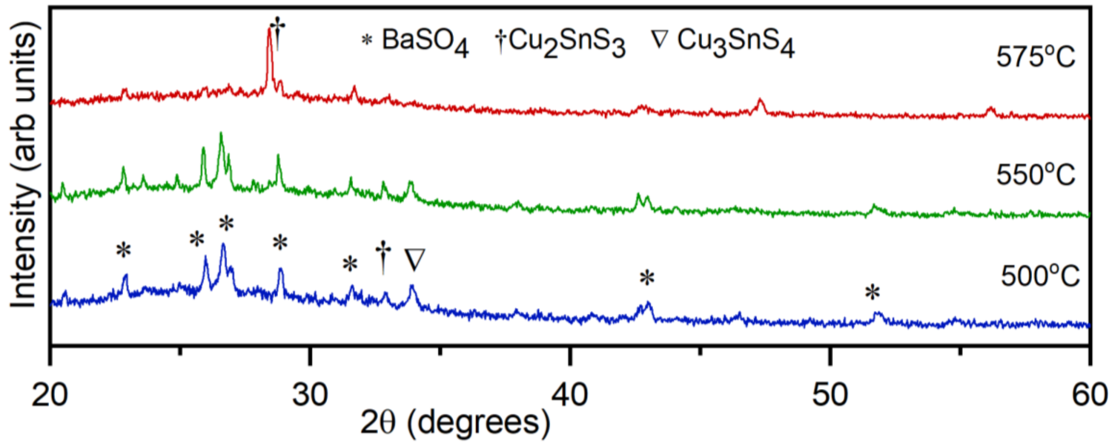

Fig. 4.5: Typical XRD pattern of the films grown from precursor solution with [Ba]/[Sn] = 1.3 and sulfurized for 60 min with 0.5 g of S at different temperatures. At this composition, $BaSO_4$ and CTS phases are observed with comparable intensities, but no peak corresponding to CBTS is observed at any temperature.

These results indicate that there was poor incorporation of Ba in the films grown with ideal cation concentration in the precursor solution and increasing the [Ba]/[Sn] value from the ideal 1.0 to 1.3 resulted in increasing the proportion of the $BaSO_4$ phase compared to the Cu_2SnS_3 phase. It suggests that further increase in the [Ba]/[Sn] value may facilitate the reaction between the components and the formation of CBTS. Figure 4.6 shows the XRD pattern of the films grown with [Ba]/[Sn] = 1.4 in the precursor solution and sulfurized for 30 min with 0.5 g sulfur at various temperatures.

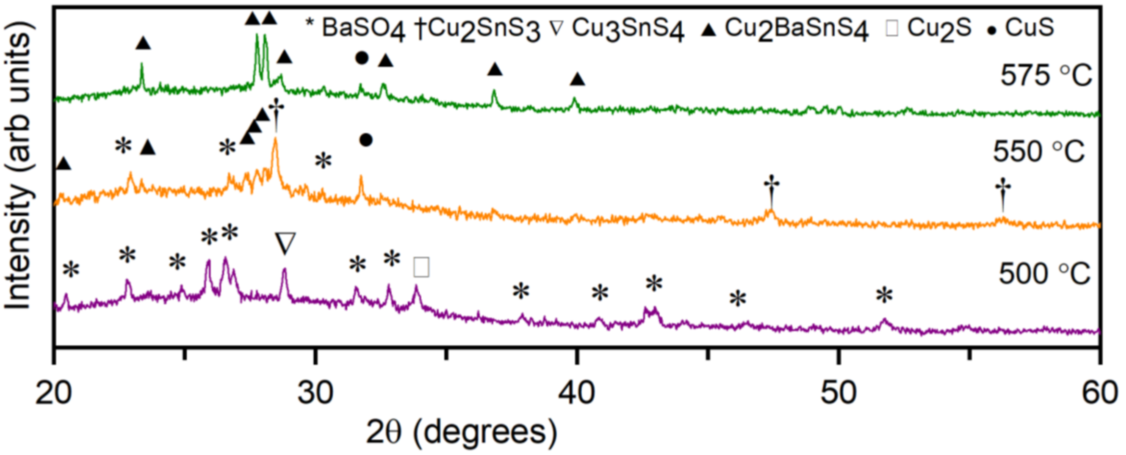

Fig. 4.6: Typical XRD pattern of the films grown with [Ba]/[Sn] = 1.4 in the precursor solution and sulfurized for 30 min with 0.5 g of S at various temperatures. Note that the film sulfurized at 575 ˚C consists of the CBTS phase with a minor trace of CuS.

The pattern for the film sulfurized at 500 ˚C showed the presence of $BaSO_4$ (JCPDS file: 01–072–1378), Cu_2SnS_3 (JCPDS file: 01–027–0198), Cu_3SnS_4 (JCPDS file: 00–039–0217) and Cu_2S (00–002–1272) phases. However, unlike the cases of [Ba]/[Sn] for 1.0–1.3, the intensity of the peaks of $BaSO_4$ was comparable to that of the Cu_2SnS_3 and Cu_3SnS_4 phases. With increase in the sulfurization temperature to 550 ˚C, the peak corresponding to the Cu_2S phase (at ~33.76˚) disappeared, intensity of the $BaSO_4$ peaks decreased and peaks corresponding to the CBTS phase (JCPDS file: 03–065–7569) appeared. Further increase in the sulfurization temperature (i.e., 575 ˚C) caused reactions that yielded the CBTS phase. All the peaks in the XRD pattern, except a peak at ~31.72˚ that corresponds to the CuS phase (Fu et al., 2016; Kassim et al., 2020) are identified with the CBTS phase. It appears that the formation of $BaSO_4$ in initial stage in significant amount is crucial to the development of the CBTS phase in the current case. As evidenced, increase in the sulfurization temperature from 500 to 550 ˚C (for same duration and sulfur amount) the intensity of the $BaSO_4$ peaks decreased with simultaneous evolution of the CBTS peaks.

With further increase in the sulfurization temperature to 575 ˚C, the $BaSO_4$ peaks disappeared and a dominant CBTS film was obtained, possibly governed by the following reaction.

$$BaSO_4 + Cu_2SnS_3 \rightarrow Cu_2BaSnS_4 + 2O_2 \tag{4.3}$$

It is worth mentioning that apart from the temperature, the dwelling time and the amount of sulfur during the sulfurization process step can affect the reaction pathway (Redinger et al., 2011; Ren et al., 2017; Olgar et al., 2023). Boosted by the appearance of the CBTS phase in the 550 ˚C - sulfurized samples, we carried out additional experiments by varying the sulfurization parameters. Figure 4.7 shows the typical XRD patterns of the films grown with [Ba]/[Sn] = 1.4 in the precursor solution and sulfurized at 550 ˚C at different sulfurization parameters. While the films sulfurized for 30 min with 0.5 g of sulfur contained traces of CBTS phases (Fig. 4.6), increase in the sulfur amount 1.0 g apparently did not yield only CBTS phase (Fig. 4.7). When the dwelling time was increased to 60 min (sulfurized with 0.5 g of sulfur), peaks corresponding to the CBTS phase disappeared and those for $BaSO_4$, Cu_2S and Cu_3SnS_4 phases appeared, which is indicative of a decomposition reaction of the CBTS. It is believed that with 0.5 g sulfur, a longer dwelling time will cause sulfurization in a sulfur-deficient environment that would decompose the CBTS and prevent sustained formation of CBTS. Similar observation during the CZTS thin films growth has been reported by Ren et al. (Ren et al., 2017) and Redinger et al. (Redinger et al., 2011).

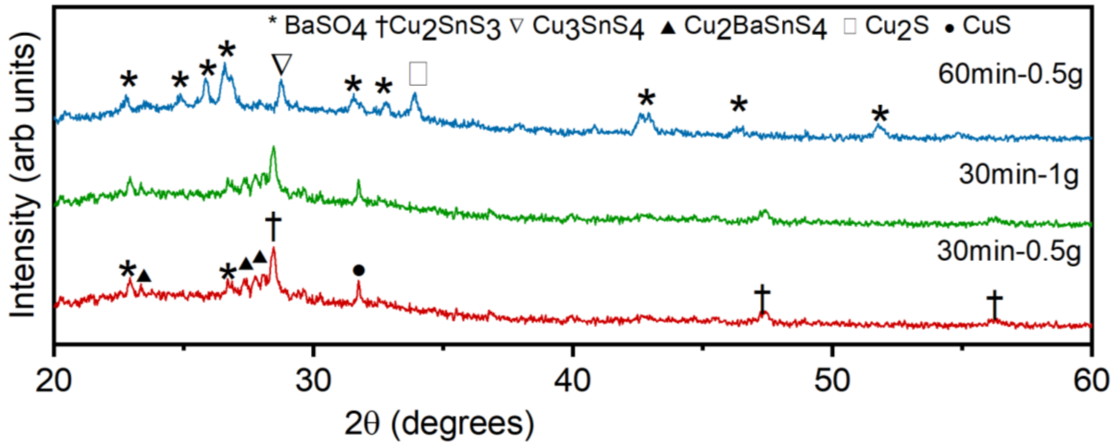

Fig. 4.7: Typical XRD pattern of the films grown with [Ba]/[Sn] = 1.4 in the precursor solution and sulfurized at 550°C for different durations and amount of sulfur powder.

On the other hand, variation in the sulfurization parameters for 575°C yielded interesting results and are summarized in Fig. 4.8. XRD pattern of the film prepared by sulfurization for 30 min with 1 g of S disclose the fabrication of the CBTS phase along with a minor contribution of CuS, as observed from Fig. 4.6. In order to explore whether the amount of S has any role in the observed CuS phase, sulfurization was carried out with increased amount up to 2.0 g. However, no change in the XRD patterns was observed (Fig. 4.8a). The persistence of the CuS phase may indicate incomplete reactions during the sulfurization process. This was indeed confirmed by preparing films by sulfurization with 1.0 g S for 45 mins, which exhibited XRD peaks corresponding only to the CBTS phase. The phase purity of the sample was further confirmed by Raman spectroscopy as shown in Fig. 4.7b**.** Raman peaks at 186, 251, 341 and 366 cm^{-1} were observed, which have been identified as characteristic vibrational modes of CBTS (Crovetto et al., 2020; Luo et al., 2020). It may be noted that sulfurization for similar duration (45 min) with lesser amount of sulfur (0.5 g) yielded mixed phases. This suggests that although sulfurization at 575 ˚C promoted reaction between Cu-Sn-S and Ba-S compounds, only an appropriate set of sulfurization parameters (temperature, dwelling time and the amount of sulfur) leads to the formation of single phase CBTS.

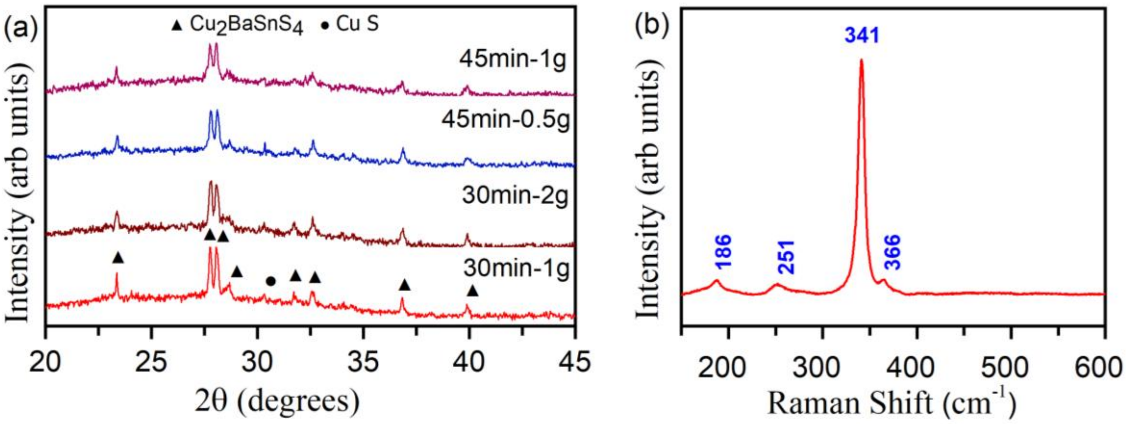

Fig. 4.8: (a) Typical XRD pattern of the films grown with [Ba]/[Sn] = 1.4 in the precursor solution and sulfurized at 575 °C for different durations and different amount of sulfur powder. Phase pure CBTS films were obtained only for sulfurization with 1.0 g S for 45 mins. (b) The Raman spectrum of the phase pure sample. All the Raman peaks are identified with vibrational modes of CBTS.

These results highlight the complex interdependence of molar concentration of salts in the precursor solution and sulfurization parameters on the reaction pathway and the CBTS phase formation. The same has been schematically summarized in Fig. 4.9**.**

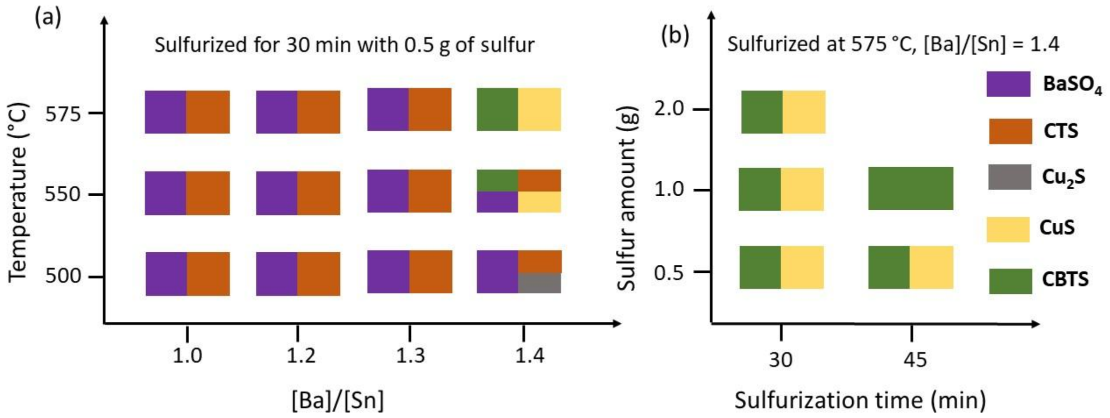

Fig. 4.9: Evolution of phases as a function of (a) [Ba]/[Sn] ratio in the precursor solution and sulfurization temperature (dwelling time of 30 mins with 0.5 g of sulfur) and (b) dwelling time and sulfur amount for sulfurization at 575 °C. The picture is not to scale.

4.2 Properties of the phase pure CBTS thin films

We then examined numerous properties such as surface morphology, optical and electrical properties of the single phase CBTS film (i.e., the film grown with [Ba]/[Sn] = 1.4 in the precursor solution and sulfurized at 575 ˚C for 45 min with 1.0 g of sulfur).

4.2.1 Microstructure

Figure 4.10 shows the typical surface and cross-sectional microstructure of the films. A uniform morphology was observed. The thickness of the films grown from two cycles of spin coating was found to be ~740 nm.

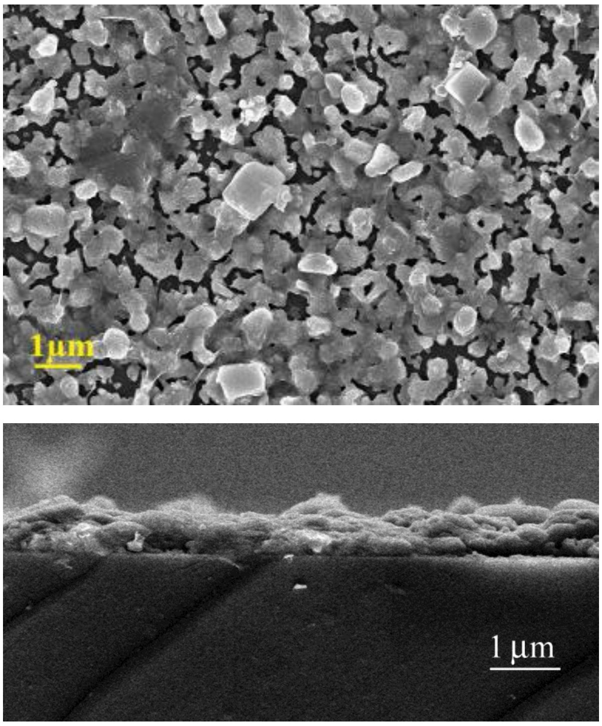

Fig. 4.10: Representative surface and cross-sectional FESEM image of the phase pure CBTS film (i.e., the film grown with [Ba]/[Sn] = 1.4 in the precursor solution and sulfurized at 575 °C for 45 min with 1.0 g S).

4.2.2 Optical properties

The optical bandgap (E_g) of the films was estimated from the Tauc plot of $(\alpha h\nu)^2$ vs photon energy hν, where α is the absorption coefficient. The value of α was determined using the reflectance (R) and transmittance (T) curves (shown in Fig. 4.11a) using the formula $\alpha = (1/d) \ln [(1-R)^2/T]$ for the film of thickness d. The bandgap is estimated by linearly extrapolating the $(\alpha h\nu)^2$ vs hν curve (Fig. 4.11b). The bandgap of the present film was found to be 2.00 eV, which is consistent with earlier reported values for CBTS (Teymur et al., 2018; McCarthy et al., 2018; Chen et al., 2018). This is also supported from the room temperature PL measurement that revealed a strong symmetric peak centered at about 2.06 eV (shown in Fig. 4.11c). This peak is typical of near-band edge (NBE) emission of the CBTS films, as reported in literature (Crovetto et al., 2019; Levcenko et al., 2021; Kim et al., 2021). Typically the PL peak width tends to widen when tail states are present, as observed for the CZTS based thin films (Ge et al., 2016; Teymur et al., 2021; Teymur et al., 2022). In the present case, the presence of a sharp symmetric PL peak, therefore, is indicative of significantly reduced cationic antisite disorder, as suggested by the earlier theoretical and experimental studies (Ge et al., 2016; Levcenko et al., 2021; Crovetto et al., 2020).

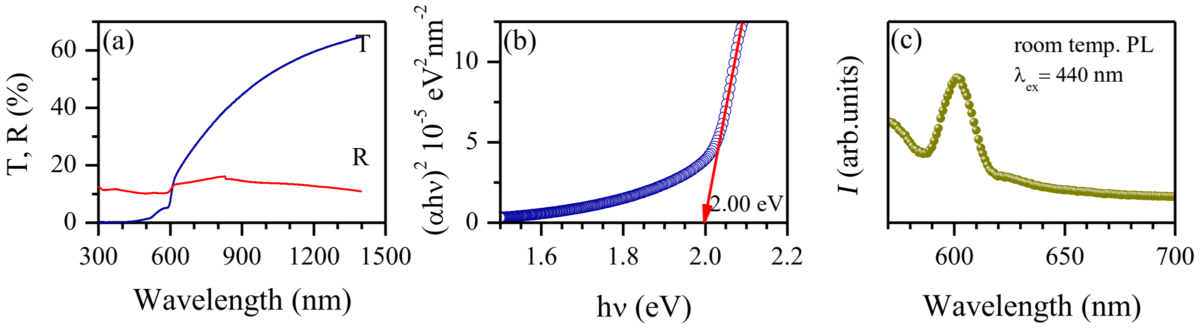

Fig. 4. 11: (a) Transmittance (T) and reflectance (R) of the phase pure CBTS thin film (i.e., the film grown with [Ba]/[Sn] = 1.4 in the precursor solution and sulfurized at 575 °C for 45 min with 1.0 g sulfur); (b) Tauc plot suggesting the band gap to be 2.00 eV; (c) Room temperature PL spectrum of the film with peak at 601 nm (~ 2.06 eV).

4.2.3 Electrical properties

Electrical properties of the phase pure CBTS films were assessed from resistivity and Hall measurements at using the van der Pauw geometry. Aluminum of a thickness of ~ 250 nm was deposited onto four corners of samples of ~1×1 cm^2 area through shadow mask by thermal evaporation. The resistivity of the film was found to be ~ 8.1×10^4 Ωcm, which is of the same order as observed for CZTS thin films in literature (Gershon et al., 2016). Hall measurement revealed p-type conductivity of the samples with a carrier concentration of ~1.7×10^{14} cm^{-3}. Using the obtained values of resistivity and carrier concentration, the Hall mobility was estimated to be about 0.45 cm^2/Vs. The observed carrier concentration of the order of 10^{14} cm^{-3} in our films is similar to the earlier reports of Chen et al. (Chen et al., 2018), Kim et al. (Kim et al., 2021), Shin et al. (Shin et al., 2017), Guo et al. (Guo et al., 2019), etc. However, this value of carrier concentration is significantly lower than that of the high performing CZTS (~10^{16} cm^{-3}) thin films (Ziabari et al., 2020). In the CBTS films, Cu-vacancy, which acts a shallow acceptor, is energetically favoured and is expected to contribute to carrier (hole) concentration (Teymur et al., 2022; Hong et al., 2016). In view of this, the poor concentration in the present films suggests the presence of a compensation mechanism. While investigating CBTSSe films with poor composition, Teymur et al. have found that hole concentration remained nearly same despite variation in the Cu-poor composition (Teymur et al., 2022). They suggested that in these type of films, the compensating mechanisms may limit the effect of doping. On the other hand, the lower mobility of the present films compared to that reported in literature (Teymur et al., 2022; Kim et al., 2021; Guo et al., 2019) may be attributed to the small grain size and voids in the films.

Typical photoresponse of the phase pure CBTS films is presented in Fig. 4.12. Photosensitivity of the films was calculated from the light and dark currents I_{light} and I_{dark} with the relation $\Delta I\ (\%) = \frac{I_{light}-I_{dark}}{I_{dark}} \times 100$. As noted from the figure, the films exhibited about 30% increase in the current upon white light illumination. The photosensitivity of the films is apparently low compared to that of the CZTS thin films (Gupta et al., 2019). This may be due to higher bandgap of the CBTS films compared to that of CZTS (which implies absorption of limited portion of the solar spectrum), and poor separation of photo-generated electron hole pairs and their collection (Pandey et al., 2022).

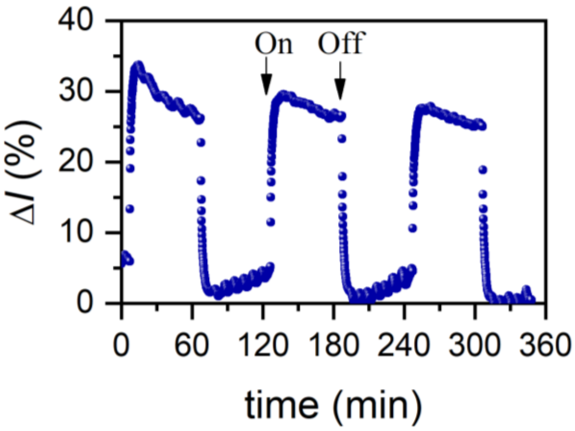

Fig. 4.12: Typical white light photoresponse of the phase pure CBTS films. $\Delta I\ (\%) = \frac{I_{light}-I_{dark}}{I_{dark}} \times 100$ when I_{light} and I_{dark} represent light and dark currents.

4.2.4 Electrochemical Impedance spectroscopy (EIS)

Further investigation of the phase pure CBTS films was carried out by EIS. In the typical three electrode system, the CBTS films grown on FTO-coated glass substrates were used as working electrode. Identical process steps of film synthesis (i.e., the film grown with [Ba]/[Sn] = 1.4 in the precursor solution and sulfurized at 575°C for 45 min with 1.0 g sulfur) yielded phase pure CBTS films as revealed from the XRD pattern (shown Fig. 4.13).

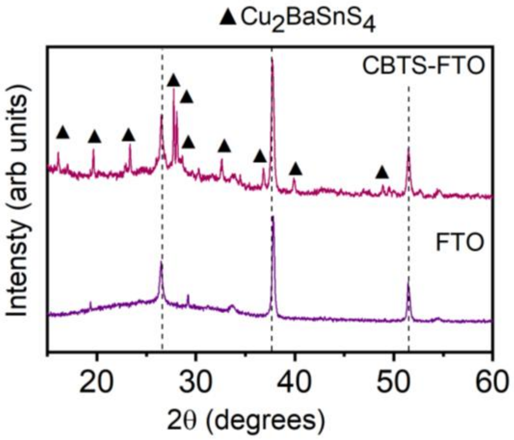

Fig. 4.13: XRD pattern of the phase pure CBTS film on FTO coated glass substrate. The CBTS film was fabricated using optimized precursor solution composition, sulfurization temperature, duration and amount of sulfur (i.e., the film was grown with [Ba]/[Sn] = 1.4 in the precursor solution and sulfurized at 575 °C for 45 min with 1.0 g sulfur).

Figure 4.14a shows the Nyquist plot of complex impedance that consists of a semicircle in the frequency range from 5 MHz to 5.6 kHz and a straight line in the low frequency region from 5.6 kHz to 1 Hz. The high frequency impedance portion arises from the capacitance of the space charge region (C_{SC}) and the accompanying resistance (R_{SC}) due to contact of electrode and the electrolyte. On the other hand, the linear behaviour in the low frequency region is expected to account for the ionic diffusion in the electrolyte nearer to the electrode-electrolyte interfacial region, typically characterized by a Warburg element W. Our initial efforts to model the observed impedance data through a combination of a series resistance (R_s), a resistor-capacitor element pair (C_{SC} and R_{SC}) and the Warburg element W failed. The impedance data could be fitted successfully, as shown in Fig. 4.14a, only when another resistor-capacitor element pair was included in the model (shown in inset to Fig. 4.14a). This additional element pair may be indicative of the charge transfer resistance at the electrode-electrolyte interface (R_{CT}) and the accompanying Helmholtz capacitance (C_H) (Ge et al., 2017; Formal et al., 2011).

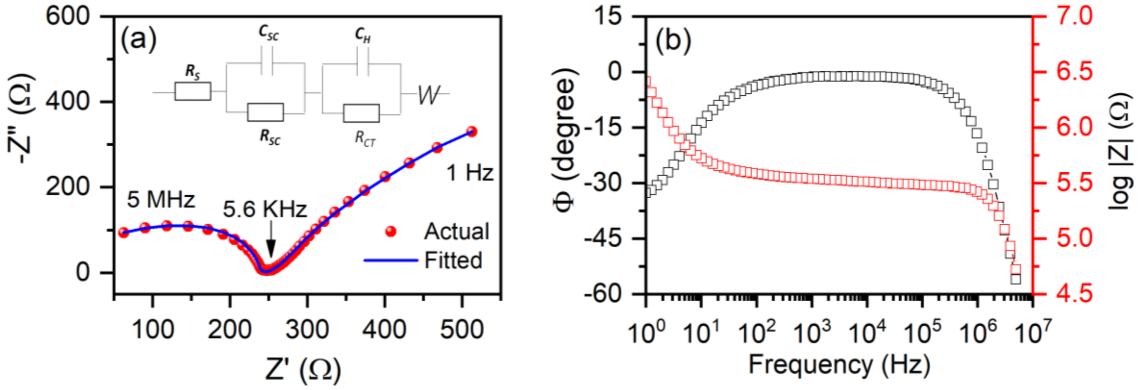

Fig. 4.14: (a) measured and fitted Nyquist plot in the frequency range from 5 MHz to 1 Hz using a 10 mV sinusoidal potential. The measure data were fitted using a circuit model (given as inset) and (b) Bode phase plot of phase pure CBTS film.

The values of circuit elements obtained from the fitting of the experimental data are found to be $R_s = 21.9\ \Omega$, $R_{SC} = 221.7\ \Omega$, $C_{SC} = 0.26$ nF, $R_{CT} = 349.3\ \Omega$ and $C_H = 0.69$ mF. The characteristic time constants corresponding to the resistance-capacitance pairs was determined to be 0.057 μs and 0.24 s for the R_{SC} - C_{SC} and R_{CT} - C_H pairs, respectively. These values of time constants suggests that the transfer of charges at the CBTS-electrolyte interface is much slower compared to the electronic process occurring in bulk CBTS. Such a behaviour has been reported for CBTS based photoelectrochemical cells earlier (Ge et al., 2017).

The Bode plot, which describes the electron life time within the electrode-electrolyte transitions, is presented in Fig. 4.14b. The negative values of the phase angle suggests superior electrochemical behaviour (Swami et al., 2014). The carrier lifetime can be estimated from $\tau = 1/(2\pi f_{max})$ and is associated with the recombination rate of the charge carriers (Sharma et al., 2021). In the present case, a carrier lifetime of 44.62 μs is estimated. Incidentally, this value is more than that estimated for the CZTS thin films (Pandey et al., 2022). Typically, the carrier lifetime is correlated to the carrier recombination rate, i.e., greater is the lifetime, lesser will be the carrier recombination loss. In the particular case of electrochemical catalysis, a higher carrier life time is desirable.

In this chapter, we have demonstrated control of reaction pathway directing to the formation of single phase CBTS thin films from a non-toxic 2-methoxy ethanol based solutions. It was found that the molar concentration ratio [Ba]/[Sn] in the precursor solution plays a decisive role in the formation of initial phase and hence, the reaction pathway. Ideal cation ratio always yielded secondary phases in spite of a large variation in the sulfurization parameters. The low [Ba]/[Sn] values (< 1.4) in the solution and low sulfurization temperature yielded predominantly $BaSO_4$ and Cu_2SnS_3 phases, whereas [Ba]/[Sn] = 1.4 favoured the formation of phase pure CBTS for precursor films sulfurized at 575 ◦C. UV–visible and room temperature PL measurements revealed a band gap of ~2.0 eV for these films. The films showed white light sensitivity (~30%) for illumination of 24 mW/cm^2. Detailed electrical and electro-impedance measurements showed p-type conductivity with 1.7×10^{14} cm^{-3} a carrier concentration for the films.

CHAPTER 5

Growth and characterization of Se-alloyed Cu_2BaSnS_4 (CBTSSe) thin films

As shown in the previous chapter, Cu_2BaSnS_4 (CBTS) thin films were synthesized using a molecular precursor solution and employing optimized post-deposition annealing process parameters. Phase-pure CBTS films were obtained for a concentration ratio of [Ba]/[Sn] = 1.4 in the solution and sulfurized at 575 °C for 45 minutes with 1.0 g of S in a tubular furnace under flowing Argon. The introduction of Se in pure sulphide CZTS helps tune the bandgap and improve its grain size (Raju at al., 2013; Tiwari et al., 2017a; Tiwari et al., 2017b). The tuning of bandgap helps in increasing the range of solar spectrum that can be absorbed, whereas the increase in grain size decreases the density of grain boundaries, and hence minimizes the recombination rate at the grain boundaries (Wei et al., 2019). Consequently, the power conversion efficiency of the CZTSSe devices is increased. Along similar lines, it is expected that Se alloying of CBTS will decrease the bandgap from 1.9 eV, making it more appropriate for photovoltaic applications. In fact, the theoretical calculation has predicted that the bandgap of $Cu_2BaSn(S_{1-x}Se_x)_4$ lies in the range of 2.0 - 1.55 eV, and the minimum value of 1.55 eV is obtained for x = 3 (Hong et al., 2016). This chapter deals with the synthesis of CBTSSe thin films using the solution-based process.

5.1 Evolution of phase in CBTSSe thin films

The details of the synthesis of the films from a molecular precursor solution have been presented in Chapter 2. Briefly, two solutions, solution A (containing copper acetate, tin chloride and thiourea mixed homogeneously in 2-methoxyethanol) and solution B (prepared by mixing barium acetate with the help of lactic acid in 2-methoxyethanol) were prepared. These two solutions were mixed under magnetic stirring for 15 minutes to make the precursor solution. Amount of Ba in Solution B was adjusted to vary [Ba]/[Sn] ratio in the final solution. The precursor solution was spin coated on SLG substrates and was dried at 270 °C for 2 minutes. This cycle of spin coating was replicated for several times to get a sufficiently thick as-deposited film. The as-deposited film was annealed in a tubular furnace at various temperatures with 1.0 g of S (this amount of sulfur was used for the synthesis of phase pure CBTS thin films as mentioned in the last chapter). While annealing along with sulfur, different amounts of Se ingots were placed in the crucible. This process of heat treatment in presence of solid sulfur and selenium is referred to as sulpho-selenization.

The as-deposited films were sulpho-selenized using the same conditions in which phase pure CBTS thin films were obtained (i.e., at 575 °C for 45 minutes with 1.0 g of S and added 0.1 g of Se so that the ratio Se/(S+Se) is ~ 0.1). However, the resultant film was found to be damaged. The film was peeled off at several places making it highly non-uniform across an area of 25 mm × 25 mm, as shown in Fig. 5.1. Traditionally, in the CZTS films, the inclusion of Se has been found to increase the net volume of the films. In the present case, annealing for a longer duration (45 minutes) caused a decomposition reaction. Therefore, the time duration of sulpho-selenization was reduced from 45 to 5 minutes. However, this also resulted in the removal of the film at places. This indicates that the processing temperature of 575 °C is not sustainable even for 5 minutes.

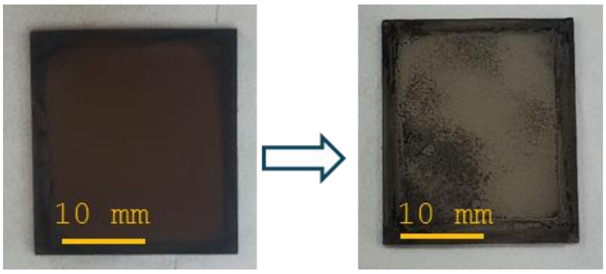

Fig. 5.1: Photograph of as-deposited film (left panel) and the film after sulpho-selenization (right panel) at 575 °C for 45 min with 1.0 g of S and 0.1 g of Se. The [Ba]/[Sn] ratio was 1.4 in the precursor solution.

In view of the above, the temperature was lowered to 550 °C and the sulpho-selenization was carried out for 45 minutes with 1.0 g of S and 0.1 g of Se. However, the results were similar (i.e., the film was patchy and highly non-uniform due to loss of film). However, when the dwelling time was reduced to 5 min, the resultant film was uniform in appearance. XRD pattern of the film revealed the presence of two dominant peaks at 2θ values of about 28.2 and 28.9° and minor peaks at 22.8, 25.9, 26.9, 31.5, 32.7, 42.8 and 47.18°. Analysis of the pattern revealed that none of these peaks correspond to either CBTS or CBTSSe. For example, the peaks at 28.2, 42.8 and 47.18° can be assigned to $Cu_2Sn(S,Se)_3$ (CTSSe) (Bayazıt et al., 2019). The peak at 28.9° corresponds to the Cu_3SnS_4 (CTS) phase, whereas those at 22.8, 25.9 and 26.9° are signatures of the $BaSO_4$ phase. The minor peak at ~31.7° is because of the CuS phase. The formation of these secondary phases was also observed during formation of CBTS phase (Chapter 4). The presence of only secondary phases possibly signifies poor reaction between these phases that would have otherwise yielded a single phase. In order to boost the inclusion of Se, the amount of Se during the sulpho-selenization was varied from to 0.2 to 0.5 g. In all cases, the films were uniform and had a gray-black appearance. The typical XRD pattern of the films is presented in Fig. 5.2.

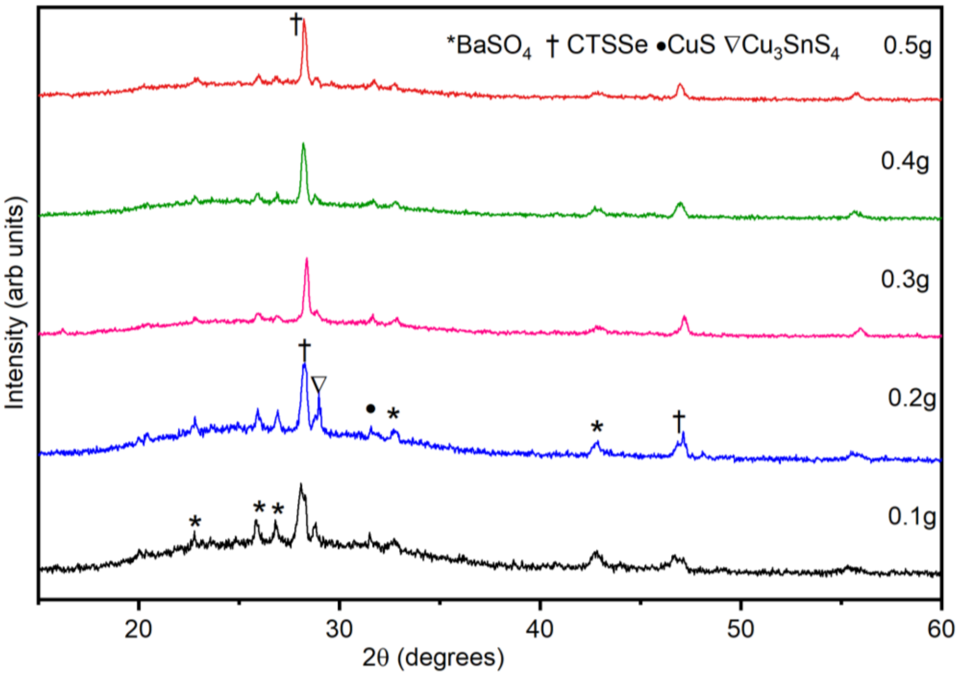

Fig. 5.2: XRD pattern of the films sulpho-selenized at 550 °C for 5 min with 1.0 g of S and various amounts of Se. The [Ba]/[Sn] ratio was 1.4 in the precursor solution. The peak indexed by † corresponds to CTS and it gets left shifted to lower angles for increasing Se amounts (0.3, 0.4 and 0.5 g) indicating the formation of CTSSe.

With the amount of Se increased from 0.1 to 0.2 g, the existing peaks became marginally sharper. When the amount of Se was increased to 0.3 g, the intensity of the peak at 28.9°, corresponding to the CTS phase, increased. With further increase in the amount of Se, this peak was shifted to lower 2θ values, indicating the change in lattice ordering with the replacement of S by Se, as Se has a larger ionic radius compared to S (Kim et al., 2017). This was also supported from the Raman spectra of the films as shown in Fig. 5.3. For the Se amount of 0.1 and 0.2 g, peaks were obtained at 293 and 348 cm^{-1} those correspond to the CTS phase (Fernandes et al., 2010). With increasing the Se amount to 0.5 g, a new peak at 255 cm^{-1} appeared in addition to the peak at 350 cm^{-1}. These peaks indicate the formation of CTSSe as reported earlier (Bayazıt et al., 2019).

Fig. 5.3: Typical Raman spectra of the films sulpho-selenized at 550 °C for 5 min with 1.0 g of S and various amounts of Se. The [Ba]/[Sn] ratio was 1.4 in the precursor solution. The corresponding XRD patterns are shown in Fig. 5.2.

The above results show that sulpho-selenization at 550 °C for 5 minutes did not yield single CBTSSe phase despite the large variation in the Se amount. This may be understood in terms of poor interaction among the secondary phases. It has been reported that increasing the time duration of annealing resulted in the elimination of secondary phases during the growth of for CZTS (Ashfaq et al., 2019). Therefore, we have increased the dwelling time to 10 minutes and assessed whether a single phase was formed. Typical XRD pattern of the films are presented in Fig. 5.4a. Major peaks at about 28.4, 47 and 56.0° were obtained for the film sulpho-selenized for 10 minutes with 0.4 g of Se. These peaks are identified with the CTS phase (Bayazit et al., 2019). The minor peaks were found to be associated with the secondary phases of CuS and $BaSO_4$ (for example, peak at ~31.7° corresponds to the CuS Phase, peaks at about 22.8, 25.9, and 26.9° correspond to $BaSO_4$). When the Se amount was increased, the peaks at about 28.4, 47.0 and 56.0° (identified with the CTS phase) are found to be left shifted, which indicates the formation of CTSSe. The presence of these phases was further confirmed by the Raman spectroscopy presented in Fig. 5.4b. One can find Raman peaks at 296 and 350 cm^{-1} corresponding to the CTS phase and a broad hump that indicates the presence of the CuS phase for the film processed with 0.4 g of Se. In support of the XRD results, Raman peaks at

204, 243, 296 and 346 cm^{-1} corresponding to the CTSSe phase (kim at al., 2017) were obtained when the Se amount was increased to 0.5 g.

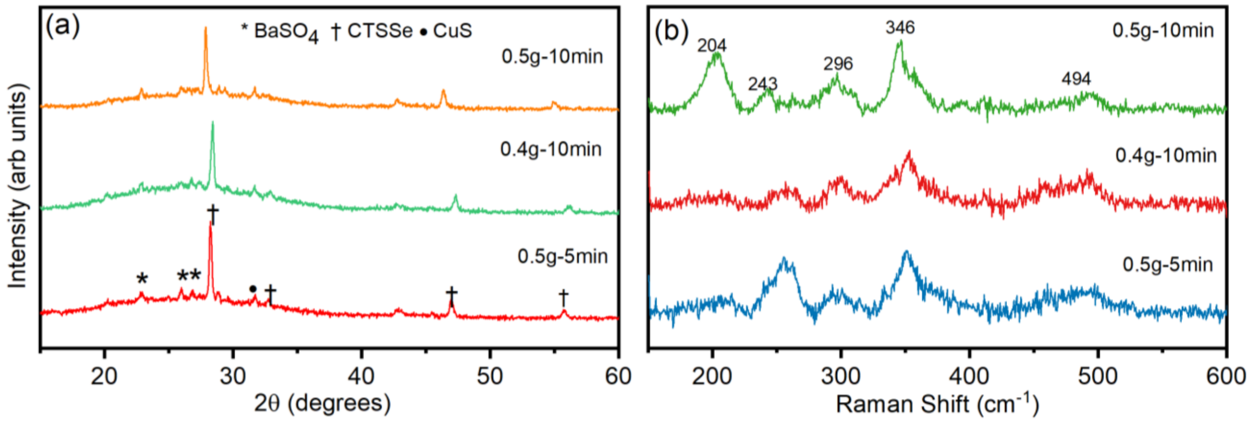

Fig. 5.4: Typical (a) XRD pattern and (b) Raman spectra of the films sulpho-selenized at 550 °C for 10 min with 1.0 g of S and various amounts of Se. The [Ba]/[Sn] ratio was 1.4 in the precursor solution.

During the growth of CZTSSe thin films, it has often been reported that annealing at a higher temperature leads to a decomposition reaction. In such a scenario, the CZTSSe, which was formed during the early stages of annealing, decomposes into the secondary phases. In order to rule out such a possibility, we have carried out sulpho-selenization at a lower temperature of 500 °C for 5 minutes with 1.0 g of S and 0.5 g of Se. The XRD pattern and the Raman spectrum of the film are presented in Fig. 5.5a and b, respectively. The XRD pattern of the films showed the presence of the peaks, similar to those obtained for sulpho-selenization at 550 °C for 5 minutes with 1.0 g of S and 0.5 g of Se. The Raman spectrum shows the peaks at 255, 290 and 350 cm^{-1} indicating the presence of CTSSe phase.

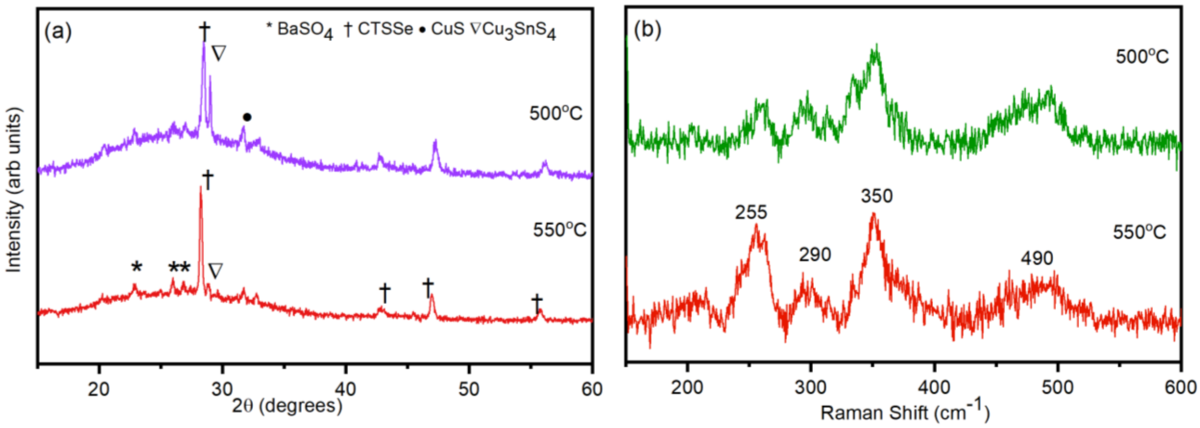

Fig. 5.5: (a) XRD pattern and (b) Raman spectrum of the film sulpho-selenized at 500 °C for 5 min with 1.0 g of S and 0.5 g of Se. The [Ba]/[Sn] ratio was 1.4 in the precursor solution. For comparison, results for the film sulpho-selenized at 550 °C with same condition are also shown.

The above-presented results suggest that CBTSSe phase could not be obtained despite large variation in the parameters (i.e., temperature, dwelling time and selenium amount) during sulpho-selenization of the as-deposited films grown with [Ba]/[Sn] = 1.4 in the precursor solution. In all cases, secondary phases such as CTS, CTSSe, CuS and $BaSO_4$ have been obtained. As discussed in the previous chapter, the presence of $BaSO_4$ in sufficient amounts was required for the formation of CBTS phase. It appears that in the case of Ba deficiency, secondary phases such as $BaSO_4$, CTS and CuS are easily formed (Teymur et al., 2018). Based on a similar argument, we have increased the [Ba]/[Sn] ratio to 1.7 in the precursor solution and fabricated thin films.

Fig. 5.6a presents the XRD pattern of the films grown from the precursor solution with [Ba]/[Sn] = 1.7 and sulpho-selenized at 500 °C with 1.0 g of S and 0.1 g of Se for various times. The two most intense peaks at about 28.4 and 28.8° are identified with Cu_2SnS_3 and Cu_3SnS_4 phases. The notable difference compared to the films obtained with [Ba]/[Sn] ratio of 1.4 (summarized in Figs. 5.2, 5.4 and 5.5), is the significant intensity of the peaks corresponding to $BaSO_4$ (at about 25.9 and 26.9°). Although no peak corresponding to CBTSSe could be observed, the comparable intensity of $BaSO_4$ and CTS indicates the possibility of the formation of CBTSSe at a higher temperature. The presence of the impurity phases Cu_2SnS_3 and Cu_3SnS_4 is also observed from Raman spectrum of the films shown in Fig. 5.6b. Raman peaks at 296 and 352 cm^{-1} correspond to the characteristic peaks of tetragonal Cu_2SnS_3, and the low intensity peak at 316 cm^{-1} corresponds to Cu_3SnS_4 (Avellaneda et al., 2022).

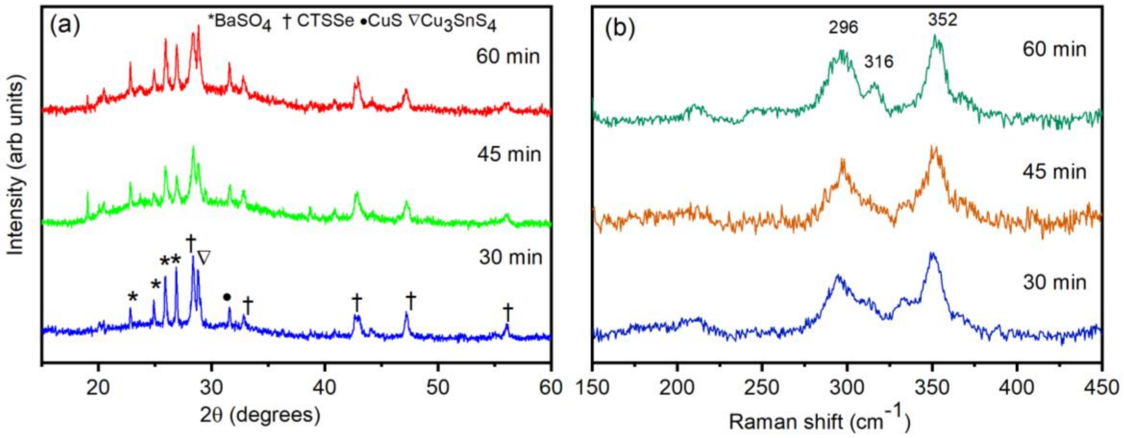

Fig. 5.6: (a) XRD pattern and Raman spectra of the films sulpho-selenized at 500 °C for different times in the presence of 1.0 g of S and 0.1 g of Se. The [Ba]/[Sn] ratio was 1.7 in the precursor solution.

The above hypothesis (i.e., the presence of $BaSO_4$ in significant amounts, as indicated by comparable intensity of XRD peaks of $BaSO_4$ and CTS can result in the formation of CBTSSe if sulpho-selenization is carried out at higher temperature) was verified by carrying out sulpho-selenization at 550 °C for various durations. The S and Se amount was kept the same (i.e., 1.0 g of S and 0.1 g of Se). The typical XRD patterns of the films are shown in Fig. 5.7a. For the films, heat treated for 5 min, impurity phases $BaSO_4$ and CTSSe were present. Although the pattern was similar to the film obtained for [Ba]/[Sn] = 1.4 (Fig. 5.2), the intensity of the peaks of $BaSO_4$ and CTSSe has now become comparable. The existence of the impurity phases (indicated by peaks at about 292 and 350 cm^{-1}) is also confirmed from the Raman spectrum, shown in Fig. 5.7b. When the dwelling time was increased to 15 min, significant changes in the XRD pattern of the film were observed. The peaks corresponding to $BaSO_4$ disappeared in the patterns and several peaks corresponding to CBTSSe appeared (for example, at about 23.3, 27.7, 28.0 and 32.5°). The pattern, however, contained peaks of impurity phases of CuS and CTSSe. The Raman spectrum of this film is characterized by an intense peak at 340 cm^{-1} and a hump around 490 cm^{-1} corresponding to CBTSSe and CuS, respectively. This implies that by increasing the dwelling time further a phase pure CBTSSe may be obtained.

Indeed for increased dwelling time of 30 and 45 mins, all peaks in the XRD patterns are identified with the CBTSSe phase. No peak corresponding to any impurity phase was detected. The phase purity of the samples was also confirmed by the Raman spectra, as depicted in Fig. 5.7b. However, on further increasing the dwelling time to 60 minute, the presence of the secondary phases, possibly due to decomposition of CBTSSe phase was observed.

Interestingly, decomposition of CBTSSe was also observed when the temperature of sulpho-selenization was increased to 575 °C. In the corresponding XRD patterns and Raman spectrum, only secondary phases of CTSSe and $BaSO_4$ were detected, as shown in Fig. 5.8.

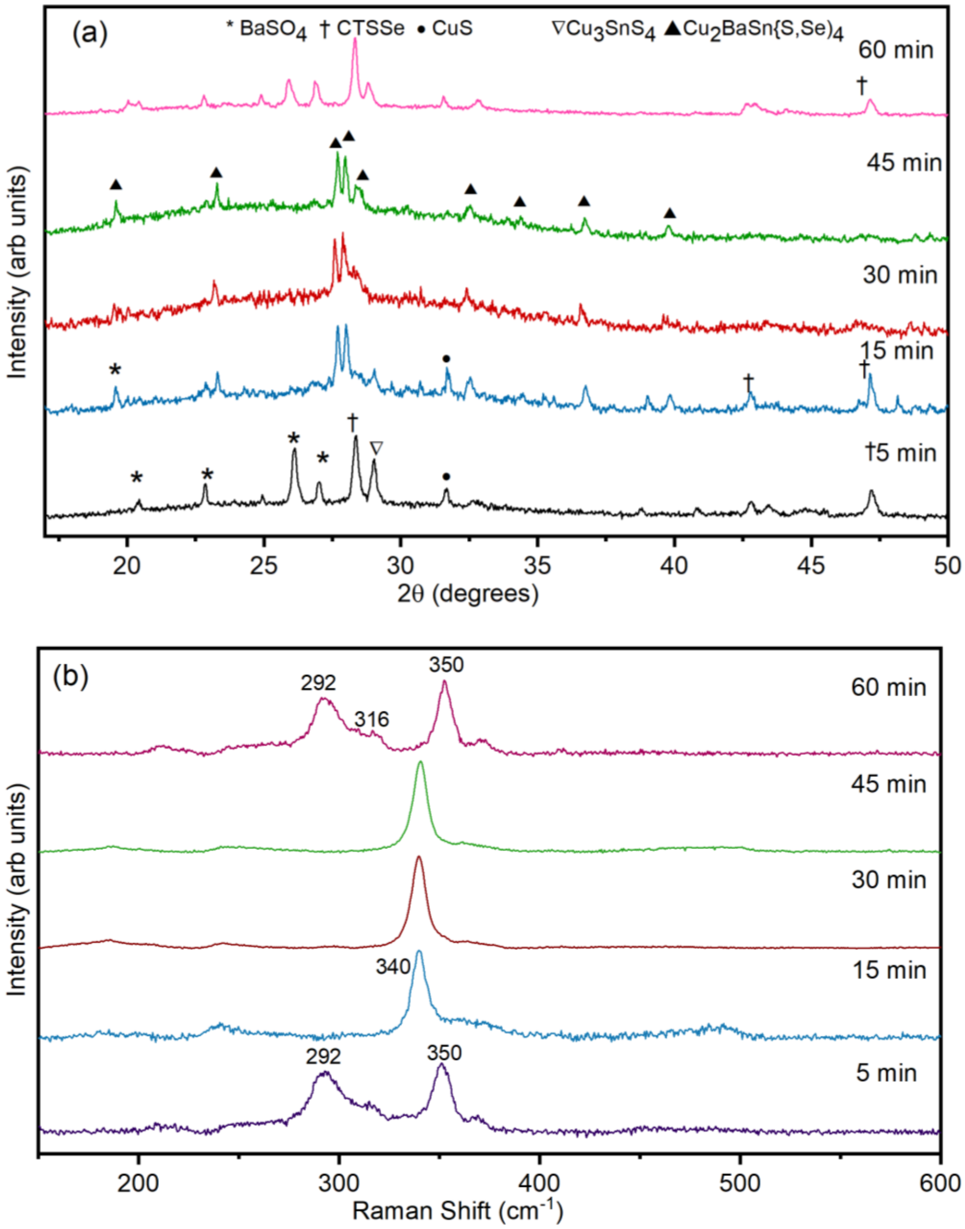

Fig. 5.7: (a) Typical XRD pattern and (b) Raman spectra of the films sulpho-selenized at 550 °C for various durations with 1.0 g of S and 0.5 g of Se. The [Ba]/[Sn] ratio was 1.7 in the precursor solution. Note that the resultant film was free of all impurity phases for heat treatment for 45 minutes.

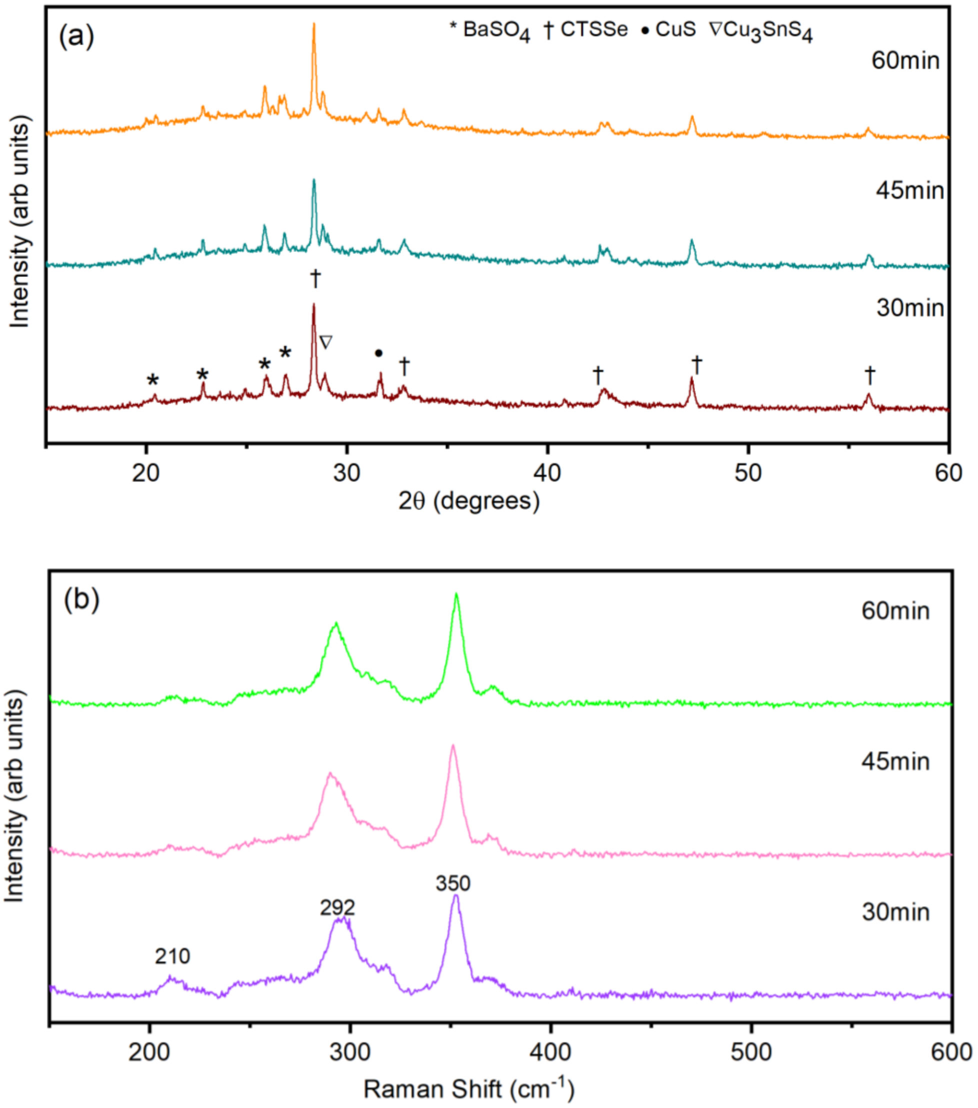

Fig. 5.8: (a) Typical XRD pattern and (b) Raman spectra of the films sulpho-selenized at 575 °C for various durations with 1.0 g of S and 0.5 g of Se. The [Ba]/[Sn] ratio was 1.7 in the precursor solution. All peaks belong to the secondary phases.

5.2 Effect of Se/(S+Se) ratio in the CBTSSe thin films

As mentioned earlier, the insertion of Se in the CBTS thin films is expected to alter the electrical and optical properties. One of the most remarkable manifestations of Se alloying is the reduced bandgap, which can make the resulting films more attractive for photovoltaic applications. In this work, the amount of Se in the films was increased by sulpho-selenizing the films with an increased amount of Se while the amount of S was kept fixed. The other conditions of the heat treatment (i.e., temperature of 550 °C, dwelling time of 45 min and S of

1.0 g) were kept unchanged. Figure 5.9a shows the XRD pattern of the films deposited on FTO substrates obtained after sulpho-selenization with varying amounts of Se. The asterisk (*) marks the peaks corresponding to the peaks arising from the FTO substrate. Rest of the peaks in the patterns are identified with the CBTSSe phase. With the increase in the amounts of Se the peaks get shifted to lower angles as reported for the CZTSSe films (Patil et al., 2020; Zaki et al., 2024). This left shift is also observed in the Raman spectra as shown in Fig 5.9b for increasing Se amount. The lower shift of the XRD peaks is thought to stem from the increase in the amount of Se in the films due to sulpho-selenization with higher amount of Se.

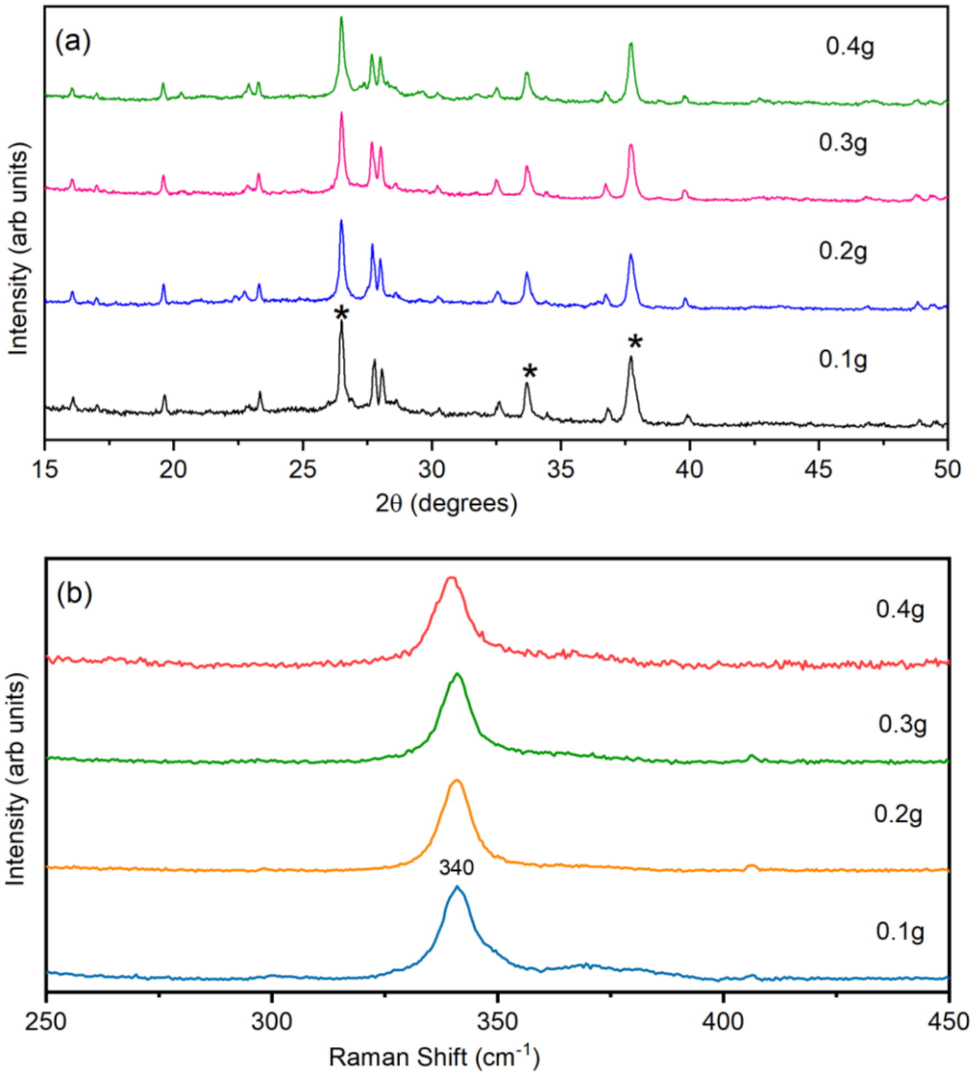

Fig. 5.9: (a) Typical XRD pattern and (b) Raman spectra of the films sulpho-selenized at 550 °C for 45 min with 1.0 g of S and varying amounts of Se. The [Ba]/[Sn] ratio was 1.7 in the precursor solution. The films were grown on FTO substrates. In the XRD patterns, the substrate peaks are marked by an asterisk (*).

Rietveld refinement of the XRD patterns of the phase pure sample (i.e., the one sulpho-selenized at 550 °C for 45 min with 1.0 g of sulphur and 0.1 g of selenium, Fig. 5.9) was performed using the GSAS II software (Toby et al. 2013). A shifted Chebyschev function with seven coefficients was used to model the background. Several parameters such as scale factors, coefficients of background function, peak shapes, crystallite size/microstrain broadening, lattice constants, atomic positions and isotropic thermal parameters were used for the refinement. Structure .cif files for Cu_2BaSnS_4 was used for the refinement of the trigonal structure. For the sample sulpho-selenized at 550 °C for 45 min with 1.0 g of sulphur and 0.1 g of selenium, atomic occupancies of S and Se were fixed at nominal ratios (e.g., 90% – and 10 %) for each anionic Wyckoff position. Figure 5.10 shows the Rietveld refinement of the XRD pattern of the sample. As noted from the figure, all peaks were identified with the trigonal phase with lattice parameters of a = 6.3739(16) and c = 15.8557(25) Å. However, the quality of the fitting is visibly poor and is reflected from the χ^2 value of about 3.3. This may be due to the large scatter in the measured XRD data. Based on our experience, a sufficiently slow scan during the XRD measurement is recommended.

Fig. 5.10: Rietveld refinements of the powder XRD pattern of the sample sulpho-selenized at 550 °C for 45 min with 1.0 g of sulphur and 0.1 g of selenium.

The elemental composition of the films was determined from EDS measurements carried out at multiple points on the film surface. Figure 5.11 shows representative EDS spectra of the samples prepared on glass substrates with varying amounts of selenium placed during the sulpho-selenization (W_{Se}).

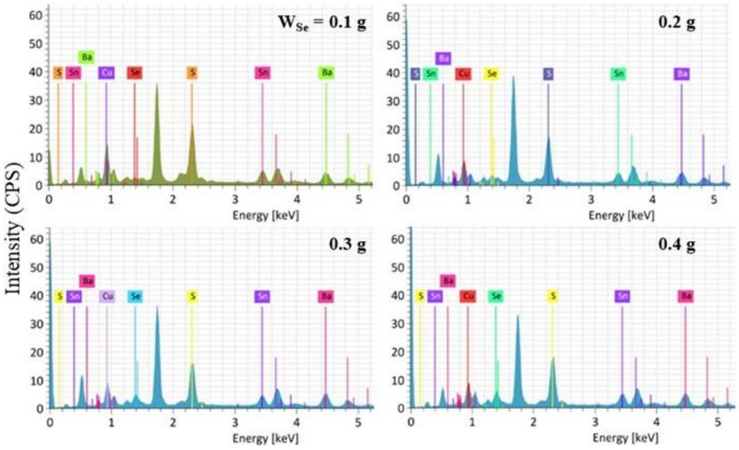

Fig. 5.11: Representative EDS spectra of the films grown with varying amounts of selenium placed during sulpho-selenization

It may be mentioned here that the EDS spectrum contained the information from the substrate owing to the small thickness of the samples. For all calculations, the contribution from the obvious peaks such as silicon and oxygen (both from substrate) and carbon (due to handling of the samples) was excluded. Figure 5.12 shows the variation in Se/(Se+S) with the amount of Se placed during sulpho-selenization. With increase in amount of Se from 0.1 to 0.4 g, the [Se]/([Se]+[S]) ratio increased from ~0.03 to 0.22. Figure 7b depicts the variation in [Se]/([Se]+[S]) with WSe, which shows a linear relationship.

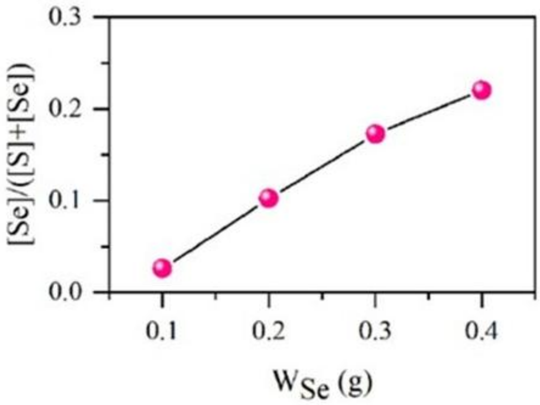

Fig. 5.12: Plot of the variation in the ratio Se/(Se+S) in the films versus the amount of Se placed during sulpho-selenization. All films were sulpho-selenized at 550 °C for 45 min with 1.0 g of S and varying amounts of Se. The [Ba]/[Sn] ratio was 1.7 in the precursor solution. The elemental composition of the films was estimated from EDS measurement carried out at multiple spots on surface of the films.

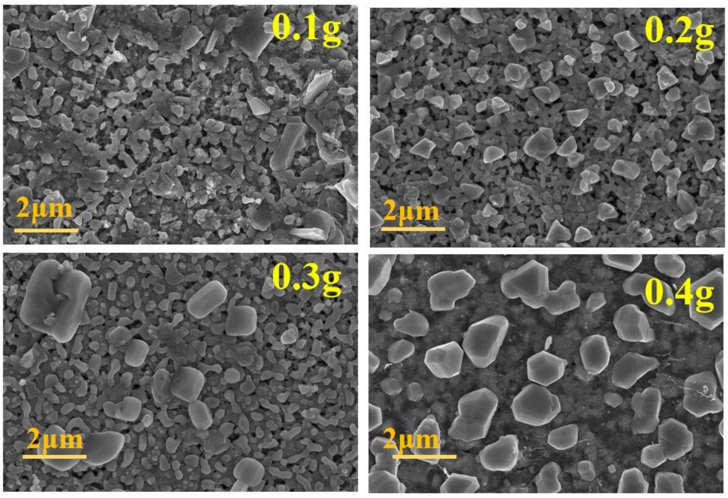

Fig. 5.13: Representative FESEM images of thin films grown with different amount of Se placed during sulpho-selenization in the furnace. All films were sulpho-selenized at 550 °C for 45 min with 1.0 g of S and varying amounts of Se. The [Ba]/[Sn] ratio was 1.7 in the precursor solution.

Typical surface microstructure of the CBTSSe thin films grown with different amount of Se placed during sulpho-selenization in the furnace are shown in Fig. 5.13. A uniform microstructure was obtained for the films with 0.1 g of Se. However, as the Se amount was increased, a different microstructure with a bimodal grain distribution was observed. Relatively larger grains were found to cover an under-layer that consisted of smaller grains. As the Se amount increased, the size of the grains on the top increased. The obtained microstructure is similar to the ones reported earlier for the CZTSSe films and is typical of nanoparticle and solution fabricated films (Werner et al., 2015a; Werner et al., 2015b; Schnabel et al., 2015).

We have then examined the variation in the bandgap of the films arising due to the increased Se amount in the films. The bandgap of the films was estimated from the Tauc's plots of $(\alpha h\nu)^2$ vs hν and by linearly extrapolating, as shown in Fig 5.14. For the film sulpho-selenized with 0.1 g of Se, the bandgap is found to be 1.93 eV, which is marginally lower than that of the pure sulphide (i.e., CBTS) film, as presented in Chapter 4. It was found that the absorption edge is shifted towards lower energy with the increase in the Se amount. The bandgap of the films was found to decrease with Se amount (Fig. 5.14b). The bandgap of the film heat treated with 0.4 g of Se (Se/(Se+S) = 0.22 in the films) was found to be 1.55 eV. This reduction in the bandgap is attributed to larger radius of Se as compared to S, which makes atomic levels of p Se at higher energy as compared to those of S.

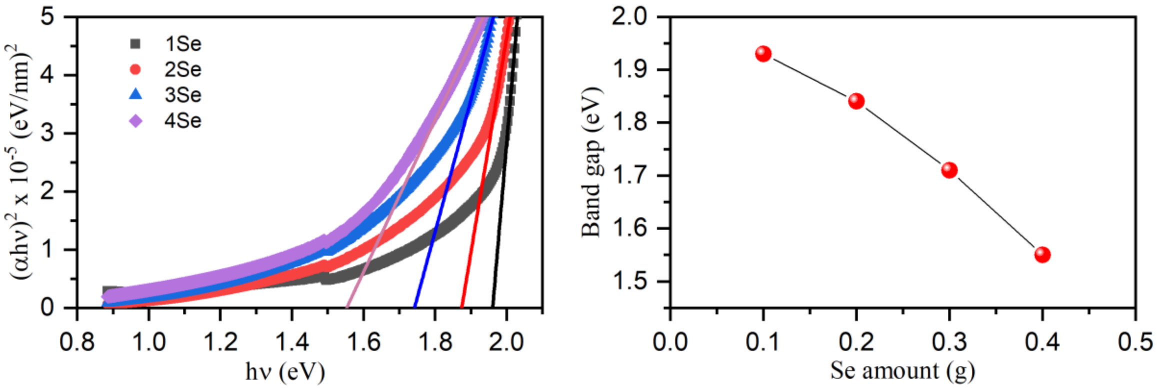

Fig. 5.14: (a) Tauc plot of the films prepared with different amounts of Se during sulpho-selenization; (b) Variation in the bandgap of the films with the amount of Se placed during sulpho-selenization in the furnace.

Electrical resistivity of the films was measured using the van der Pauw method. The resistivity for the CBTSSe film prepared with 0.1 g of Se was found to be ~4.3 x 10^2 Ωcm. Increasing the Se amount increased the resistivity of the films. For example, a resistivity value of 6.3 x 10^2 Ωcm was obtained for the film annealed with 0.4 g of Se. This value of resistivity of the order of 10^2 Ωcm, has also been reported for the CZTSSe thin films (McCandless et al., 2019).

5.3 Results of the EIS measurement

EIS measurements were performed using a three electrode system as outlines in Chapter 2. Since the film sulpho-selenized with 0.4 g of Se has the most suitable bandgap (~1.55 eV) for photovoltaic applications among all the films synthesized, it was chosen for the EIS measurements. This film deposited on the FTO-coated substrate was used as the working electrode. Figure 5.15a and b show the variation of real (C') and imaginary parts (C") of capacitance as a function of frequency. It may be noted that the imaginary part, C" corresponds to the irreversible dissipation of the energy generally caused by dielectric loss of the medium (Patil et al., 2020). The real and imaginary parts of the capacitance were calculated using the relations (Taberna et al., 2003),

$$C'(\omega) = \frac{-Z"(\omega)}{\omega|Z(\omega)|^2} \tag{5.1}$$

$$C"(\omega) = \frac{Z'(\omega)}{\omega|Z(\omega)|^2} \tag{5.2}$$

where ω represents angular frequency, Z', Z" and |Z| represents real part, imaginary part and magnitude of the measured impedance respectively. The decrease in capacitance is observed with increase in frequency for f < 10^2 Hz and it saturates, similar to the previous reports on the CZTSSe (Patil et al., 2020).

The Nyquist plot of complex impedance is shown in Fig. 5.15c. As observed from the figure, the curve have a half semicircle in the frequency range from 7 MHz to 1 kHz and a straight line in the low frequency region from 1 kHz to 1 Hz. It was attempted to fit the measured impedance data with multiple combination of series resistance and resistor-capacitance pairs. However, the only circuit represented in the inset of Fig. 5.13c was a successful fit. In this equivalent circuit, two resistor-capacitor element pairs, a series resistance and the Warburg element were included. As discussed in Chapter 4, the capacitance of the space charge region (C_{SC}) and the accompanying resistance (R_{SC}) are due to contact between electrode and electrolyte, and are responsible for the high frequency region of the curve. A single semicircle (though incomplete) obtained in this region suggests the single relaxation process. On the other hand, the Warburg element W characterizes the linear behaviour in the low frequency region that accounts for ionic diffusion within electrolyte close to electrolyte-electrode interface region. The second resistor-capacitance pair suggests the resistance due to charge transfer at interface of the working electrode and electrolyte, R_{CT} and the accompanying Helmholtz capacitance, C_H (Ge et al., 2017; Formal et al., 2011).

The values of the circuit elements obtained from the fitting of the data are shown in Table 5.1. The characteristic time constants corresponding to the resistance-capacitance pairs was determined to be 0.015 μs and 0.32 s for the R_{SC} - C_{SC} and R_{CT} - C_H pairs, respectively. These values of time constants suggests that the transfer of charges at the CBTSSe-electrolyte interface is much slower compared to the electronic process occurring in bulk CBTSSe. Such a behaviour has been reported for CBTS based photoelectrochemical cells earlier (Ge at al., 2017a, Ge et al., 2017b).

It is worth mentioning that the Nyquist plot for the CBTSSe thin film was very similar to that obtained for the CBTS films (presented in Chapter 4). For easy comparison, the data obtained for the CBTS films (Chapter 4) are presented in Table 5.1. As noted from the table, the values for R_s were similar (21.42 Ω for CBTSSe versus 21.9 Ω for CBTS) whereas the R_{SC} values decreased significantly (28.5 Ω for CBTSSe versus 221.7 Ω for CBTS). Similarly, the time constants corresponding to the R_{SC} - C_{SC} and R_{CT} - C_H pairs showed significant differences (0.015 μs and 0.32 s for CBTSSe versus 0.057 μs and 0.24 s for CBTS films). The observed difference may be understood from the lower resistivity of the films (the CBTSSe films have a resistivity two order of magnitude lower than that of CBTS).

Table 5.1: Comparison of values of circuit elements obtained from fitting of the Nyquist plots for CBTS (presented in Chapter 4) and CBTSSe thin films

	R_s (Ω)	R_{SC} (Ω)	C_{SC} (nF)	R_{CT} (Ω)	C_H (mF)
CBTS (Chapter 4)	21.9	221.7	0.26	349.3	0.69
CBTSSe	21.42	28.5	0.53	363.7	0.94

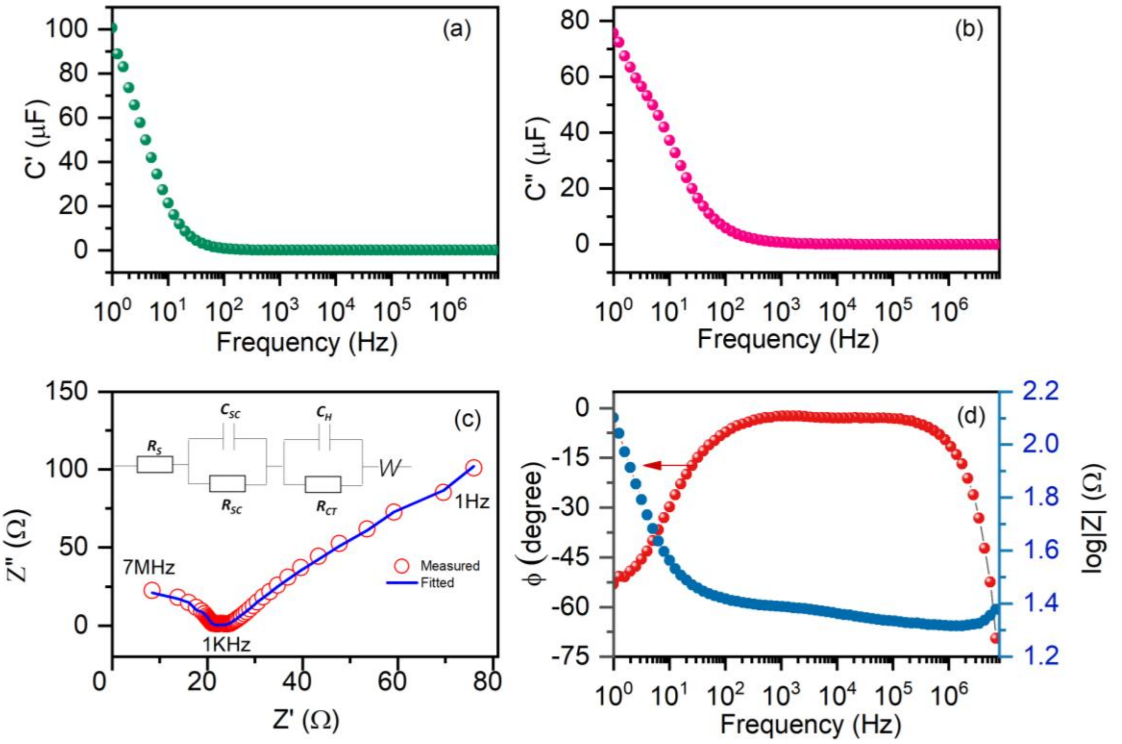

Fig. 5.15: (a-b) Real and imaginary part of the space charge capacitance of the semiconductor-electrolyte interface with respect to frequency; (c) Nyquist plot of real and imaginary part of the impedance; the inset shows the circuit diagram used for fitting the measured data; (d) Bode plot depicting the frequency response of the magnitude of impedance and phase angle.

Figure 5.15d shows the Bode plot of the CBTSSe electrode. The Bode plot, gives information about the life time of electron within the electrode-electrolyte transitions. The superior electrochemical behaviour was suggested by the negative values of the phase angle (Swami et al., 2014). The carrier lifetime was estimated from the following equation (Sharma et al., 2021),

$$\tau = \frac{1}{2\pi f_{max}} \qquad (5.3)$$

For the prepared CBTSSe thin films, a carrier lifetime of 18.89 μs is calculated. This value of the carrier life time is smaller than that of the CBTS films (44.62 μs, Chapter 4). Typically, the carrier lifetime depends on the carrier recombination rate, i.e., higher lifetime means the lower carrier recombination loss.

To study the process of charge transfer at the CBTSSe semiconductor-electrolyte junction of the cell, the capacitance-Voltage measurements were performed at 10 KHz under a DC voltage bias applied vs RHE. The results are depicted in Fig. 5.16. An exponential decrease in the capacitance was noted under the reverse voltage bias with a fixed polarization potential as show in Fig. 5.16a. The depletion width (W_d) and space charge density ($N_{C\text{-}V}$) was derived from the capacitance-voltage graph using following equations,

$$W_d = \frac{A\varepsilon_0\varepsilon_S}{C_S} \tag{5.4}$$

$$N_{C-V} = \frac{C^3}{q\varepsilon_0\varepsilon_S A^2(\frac{dC_S}{dV})} \tag{5.5}$$

where $\varepsilon_0, \varepsilon_S$, q, A and C_s corresponds to dielectric constant of vacuum (8.854×10^{-12} F/m), dielectric constant of the CBTSSe (7.3), electronic charge, area of the CBTSSe film dipped in the electrolyte and space charge region capacitance.

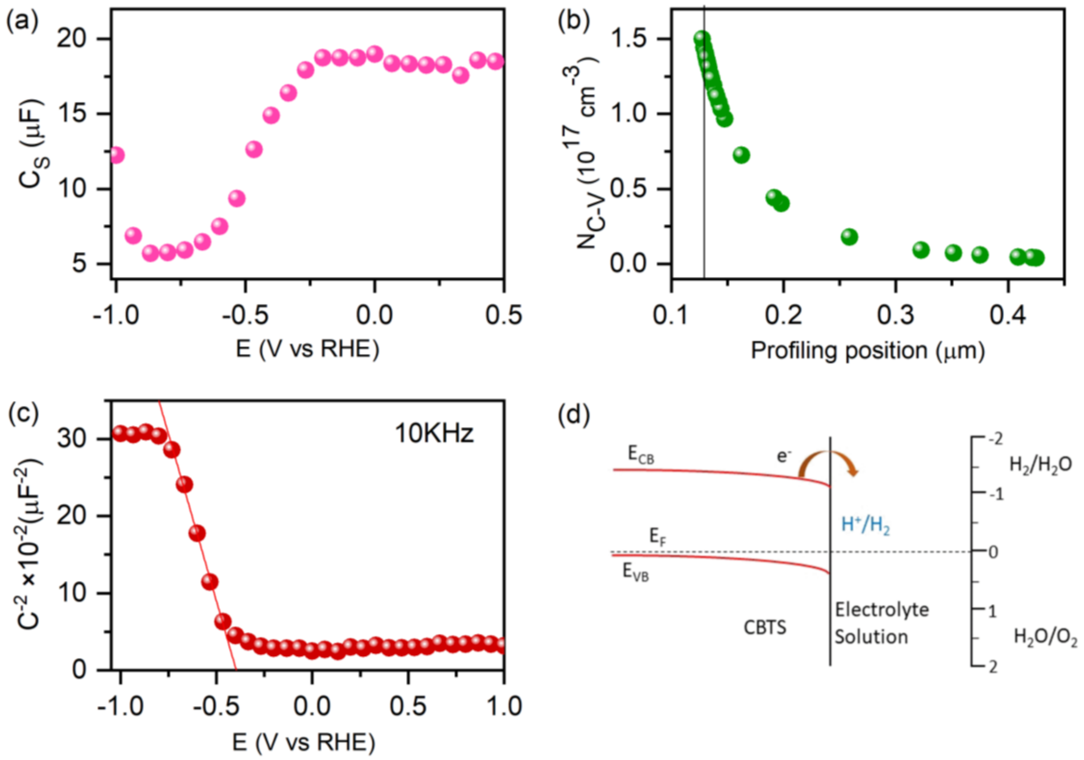

Fig. 5.16: (a) Frequency dependent space charge capacitance versus voltage; (b) Plot of profiling position and space charge density ($N_{C\text{-}V}$) calculated from the capacitance versus

voltage curve; (c) Mott-Schottky plot carried out at 10 kHz under an applied DC bias voltage, and (d) energy band position with respect to water redox potential determined by Mott-Schottky analysis of phase pure CBTSSe.

Figure 5.16b depicts the variation of space charge density $N_{C\text{-}V}$ with the profiling position and the values of W_d and $N_{C\text{-}V}$ were calculated to be 0.12μm and ~10^{17} cm^{-3}, respectively. It may be observed that high depletion width will result in more charge separation and will increase the photocurrent. Figure 5.16c represents the Mott-Schottky (MS) plot of the CBTSSe thin film. It provides the information about type of conductivity, flat band potential (V_{FB}), acceptor concentration (N_A), valance band maxima (E_{VB}) and conduction band minima (E_{CB}). Following equations are involved for estimation of N_A and Flat band potential from the MS- plots,

$$\frac{1}{{C_S}^2} = \frac{-2}{q\varepsilon_0\varepsilon_S N_A A^2}\left(V - V_{FB} + \frac{KT}{q}\right) \tag{5.6}$$

$$E_{VB} = V_{FB} + \frac{KT}{q}\ln\left(\frac{N_V}{N_A}\right) \tag{5.7}$$

where N_v represents effective density of states (~10^{19} cm^{-3}) at the valance band edge, V is applied potential, K is the Boltzmann constant, T is the temperature (300 K) and q is electronic charge. The p-type conductivity of the CBTSSe thin films is confirmed from MS plot having negative slope. The acceptor concentration calculated is 1.58×10^{17} cm^{-3} using the slope of the MS plot. The flat band potential (V_{FB}) is measured to be 0.40 V (vs RHE) using equation (5.7) and the intercept of the M-S plot. The position of valance band maxima is measured to be at 0.50 V (vs RHE). Accounting the band gap of CBTSSe film grown by sulpho-selenization with 0.4 g of Se, the position of the conduction band minima is determined to be -1.043V (vs RHE). The band edge position has been summarized in Fig. 5.16d as obtained from the analysis of the MS plot. The Fermi level is estimated to be 0.102 eV above the valance band maxima of CBTSSe. The obtained results signifies that the developed p-type CBTSSe film can be used as potential photocathode for hydrogen evolution reaction.

In this chapter, the growth of phase pure CBTSSe thin films by optimizing the process parameters (such as [Ba]/[Sn] ratio in the precursor solution, sulpho-selenization temperature and dwelling time, etc.) has been presented. The [Ba]/[Sn] ratio of 1.7 in the precursor solution was found to be the most critical factor in obtaining phase pure films. By placing varying amounts of Se in the furnace during the sulpho-selenization process step, the concentration of Se in the films was systematically varied and the impact thereof was investigated. It was observed that by varying the Se amount from 0.1 to 0.4 g during sulpho-selenization, the

Se/(Se+S) ratio in the resulted films increased from 0.05 to 0.23. With increase in the Se amount in the films, the bandgap of the films decreased gradually from 1.93 to 1.55 eV. The EIS measurement on the film grown with 0.4 g of Se during sulpho-selenization revealed its p-type conductivity with an acceptor concentration of 1.58×10^{17} cm^{-3}. The results indicate that these films can be potentially used as photocathode for hydrogen evolution.

CHAPTER 6

Summary and future scope

The major outcomes of the thesis work are highlighted in this chapter. The work for the future investigation has also been proposed.

Thin film solar cells offer promising solutions in the quest for cost-competitive and environment-friendly energy resources. In the last two decades, Cu_2ZnSnS_4 (CZTS) has drawn significant interest as an absorber layer in thin film solar cells due to its high absorption coefficient, suitable bandgap and non-toxic earth abundant constituents. However, the efficiency of the devices has been stagnated at about 12.6% despite intense global efforts. This performance is far lower than that predicted from the Shockley Queisser limit and is believed to stem from a large V_{oc} deficit as a consequence of the presence of a large density of the Cu_{Zn} antisite defects (caused due to similar sizes of Cu^{+1} and Zn^{+2}) in CZTS. Isoelectronic substitution by very different sized cations has shown to improve the cationic ordering in CZTS. In recent years, encouraging results have been obtained by replacement of Zn by Ba that yields Cu_2BaSnS_4 (CBTS). However, a large difference in size causes significant structural changes in CBTS, and hence, opto-electronic properties compared to CZTS. So far, the highest efficiency obtained for the CBTS thin film based device is about 6% that suggests more research is warranted on these films. This thesis deals with the growth and characterization of CBTS and Se-alloyed CBTS (CBTSSe) thin films.

In view of the differences in the optical and electrical properties of CBTS films with those of CZTS, we have numerically investigated and compared the performance of both devices. It is observed that an efficiency of about 17.68% can be achieved for CZTS solar cells, which is much higher than the experimentally obtained record efficiency of 11%. The experimental results could be simulated only when an appropriate amount of defects in the bulk and at interfaces (i.e., back interface MoS_2/CZTS and front interface CZTS/CdS) is introduced. For instance, inclusion of bulk defect density of 5.5×10^{15} cm^{-3}, defect density of $\sim 1 \times 10^{15}$ cm^{-2} and $\sim 1 \times 10^{14}$ cm^{-2} at back and front interfaces successfully reproduce the champion device efficiency of 11%. A possible route – by inserting a back surface field (BSF) layer - to improve the efficiency of the devices with CBTS films having these amounts of defect density has been demonstrated. We have studied the impact of Cu_2O and SnS films as BSF layers and found that the efficiency can be significantly improved to 14.7% and 15.7 %, respectively. On the other hand, for CBTS films with similar defect density that resulted 11% efficiency for CZTS (experimentally obtained champion cell) simulations yielded an efficiency of only 4.55%.

Performance of the CBTS devices could be increased to 6.9% (reported experimental value) only when the defect densities were considerably reduced (interface defect density $N_{MoS2/CBTS} \sim 10^{15}$ cm^{-2}, $N_{CdS/CBTS} \sim 10^{10}$ cm^{-2} and bulk density $N_{CBTS} \sim 10^{14}$ cm^{-3}). Apart from interface defect densities, there is a critical limit to bulk defect densities as studied by varying non-radiative recombination coefficient B_r, Auger electron (A_e) and hole recombination coefficient (A_h). Results limits the value of B_r, A_e and A_h to 10^{-7} cm^3/s, 10^{-19} cm^6/s and 10^{-22} cm^6/s, respectively. The results suggest poor defect tolerance of CBTS compared to CZTS, and hence, experimental conditions for the fabrication of CBTS films are expected to be more stringent.

The CBTS films were fabricated by spin coating of a freshly prepared non-toxic 2-methoxy ethanol based molecular precursor solution and sulfurizing it with sulphur powder. Although solution based routes appear attractive for fabrication of the films, the formation of the secondary phases must be suppressed as their presence detrimentally affect the performance of the solar cell. By varying the molar concentration ratio in the solution and the sulfurization parameters (temperature, dwelling time and sulphur amount), the reaction pathway leading to the formation of phase pure CBTS was established. It was found that the molar concentration ratio [Ba]/[Sn] in the precursor solution plays a decisive role in the formation of initial phase and hence, the reaction pathway. Ideal cation ratio always yielded secondary phases in spite of a large variation in the sulfurization parameters. The low [Ba]/[Sn] values (< 1.4) in the solution and low sulfurization temperature yielded predominantly $BaSO_4$ and Cu_2SnS_3 phases, whereas [Ba]/[Sn] = 1.4 favoured the formation of phase pure CBTS for precursor films sulfurized at 575 °C. UV–visible and room temperature PL measurements revealed a band gap of ~2.0 eV for these films. The films showed white light sensitivity (~30%) for illumination of 24 mW/cm^2. Detailed electrical and electro-impedance measurements showed p-type conductivity having 1.7×10^{14} cm^{-3} carrier concentration for the films.

Selenium-alloying of the CBTS films i.e., CBTSSe films was carried out by heat treating the as-prepared precursor films in the presence of 1.0 g of sulphur (that yielded CBTS films) and varying amounts of selenium. It was found that the process parameters that produced CBTS films yielded various secondary phases. This, thus, necessitated further optimization of the parameters including Ba/Sn ratio in the precursor solution, sulpho-selenization temperature and dwelling time, etc. The Ba/Sn ratio of 1.7 in the precursor solution was found to be the most critical factor in obtaining the phase pure films. Typically, phase pure CBTSSe films were obtained only for sulpho-selenization at 550 °C for 45 min with 1.0 g of sulphur and different amounts of selenium. By placing varying amounts of Se in the furnace during the sulpho-selenization process step, the concentration of Se in the films was systematically varied and the impact thereof was investigated. It was observed that by varying the Se amount from 0.1 to 0.4 g during sulpho-selenization, the Se/(Se+S) ratio in the resulted films increased from 0.05 to 0.23. With increase in the Se amount in the films, the bandgap of the films decreased gradually from 1.93 to 1.55 eV. The EIS measurement on the film grown with 0.4 g of Se during sulpho-selenization revealed its p-type conductivity with an acceptor concentration of 1.58×10^{17} cm^{-3}. The results indicate that this films can be potentially used as photocathode for hydrogen evolution.

This thesis work is devoted to the growth of CBTS and CBTSSe thin films by a non-toxic solution based method. The reaction pathway resulting to achieve single phase has been established in both cases. Fabrication of solar cells ad correlating the device performance to the property of the films discussed in this thesis will be natural extension of this work. For instance, the role of surface potential at grain boundaries and interaction at interfaces (front and back) can be studied to improve efficiency of devices. Studying the long-term stability of CBTS thin films under various environmental conditions (e.g., humidity, temperature, light exposure) and identifying degradation mechanisms are also very important for the photovoltaic technology and should be undertaken. One can aim at developing passivation strategies or protective coatings to enhance the stability and durability of CBTS solar cells.

Future work could focus on optimizing device fabrication processes, including absorber layer deposition techniques and interface engineering, to enhance practical device performance under real-world operating conditions. In particular, improving film uniformity and reducing secondary phase formation remain critical challenges. Additionally, a more rigorous quantitative comparison with existing literature on CBTS and related kesterite materials would help validate the present findings and better position the results within the broader landscape of emerging thin-film photovoltaic technologies. Further in-depth studies on defect chemistry, including intrinsic point defects and defect complexes, are essential to understand their impact on carrier recombination mechanisms. Advanced characterization and simulation approaches could be employed to identify dominant recombination pathways and guide strategies for minimizing non-radiative losses. Moreover, future research may explore compositional tuning, doping strategies, and bandgap engineering to improve charge carrier dynamics and overall device efficiency, thereby advancing the potential of CBTS as an eco-friendly and cost-effective alternative for next-generation solar cells.

References

1. https://www.un.org/en/climatechange/raising-ambition/renewable-energy.
2. Afzal, M., Butt, P. K., & Ahmad, H. (1991). Kinetics of thermal decomposition of metal acetates. Journal of thermal analysis, 37, 1015-1023.
3. Agawane, G. L., Vanalakar, S. A., Kamble, A. S., Moholkar, A. V., & Kim, J. H. (2018). Fabrication of $Cu_2(Zn_xMg_{1-x})SnS_4$ thin films by pulsed laser deposition technique for solar cell applications. Materials Science in Semiconductor Processing, 76, 50-54.
4. Al-Hattab, M., Moudou, L. H., Khenfouch, M., Bajjou, O., Chrafih, Y., & Rahmani, K. (2021). Numerical simulation of a new heterostructure CIGS/GaSe solar cell system using SCAPS-1D software. solar energy, *227*, 13-22.
5. Altamura, G., Vidal, J. (2016). Impact of minor phases on the performances of CZTSSe thin-film solar cells. Chemistry of Materials, 28 (11), 3540-3563.
6. Ashfaq, A., Jacob, J., Bano, N., Nabi, M. A. U., Ali, A., Ahmad, W., & Hussain, S. (2019). A two-step technique to remove the secondary phases in CZTS thin films grown by sol-gel method. Ceramics international, 45(8), 10876-10881.
7. Assoud, A., Soheilnia, N., & Kleinke, H. (2005). New quaternary barium copper/silver selenostannates: different Coordination Spheres, Metal− Metal Interactions, and physical properties. Chemistry of materials, 17(9), 2255-2261.
8. Avellaneda, D., Paul, A., Shaji, S., & Krishnan, B. (2022). Synthesis of Cu2SnS3, Cu3SnS4, and Cu4SnS4 thin films by sulfurization of SnS-Cu layers at a selected temperature and/or Cu layers thickness. Journal of Solid State Chemistry, 306, 122711.
9. Bar, M., Nishiwaki, S., Weinhardt, L., Pookpanratana, S., Shafarman, W.N., Heske, C., 2008. Electronic level alignment at the deeply buried absorber/Mo interface in chalcopyrite-based thin film solar cells. Appl. Phys. Lett. 93 (4), 042110.
10. Bär, M., Schubert, B. A., Marsen, B., Wilks, R. G., Pookpanratana, S., Blum, M., & Schock, H. W. (2011). Cliff-like conduction band offset and KCN-induced recombination barrier enhancement at the CdS/Cu_2ZnSnS_4 thin-film solar cell heterojunction. Applied Physics Letters, 99 (22).
11. Basak, A., & Singh, U. P. (2021). Numerical modelling and analysis of earth abundant Sb_2S_3 and Sb_2Se_3 based solar cells using SCAPS-1D. Solar Energy Materials and Solar Cells, 230, 111184.

12. Bayazıt, T., Olgar, M. A., Kucukomeroglu, T., Bacaksız, E., & Tomakin, M. (2019). Growth and characterization of Cu_2SnS_3 (CTS), Cu_2SnSe_3 (CTSe), and $Cu_2Sn(S,Se)_3$ (CTSSe) thin films using dip-coated Cu–Sn precursor. Journal of Materials Science: Materials in Electronics, 30, 12612-12618.
13. Bouarissa, A., Gueddim, A., Bouarissa, N., Maghraoui-Meherezi, H., 2021. Modeling of ZnO/MoS_2/CZTS photovoltaic solar cell through window, buffer and absorber layers optimization. Mater. Sci. Eng., B 263, 114816.
14. Cabas-Vidani, A., Haass, S. G., Andres, C., Caballero, R., Figi, R., Schreiner, C., Romanyuk, Y. E. (2018). High-efficiency (LixCu1− x) 2ZnSn (S, Se) 4 kesterite solar cells with lithium alloying. Advanced Energy Materials, 8(34), 1801191.
15. Carrete, A., Shavel, A., Fontané, X., Montserrat, J., Fan, J., Ibáñez, M., & Cabot, A. (2013). Antimony-based ligand exchange to promote crystallization in spray-deposited Cu2ZnSnSe4 solar cells. Journal of the American Chemical Society, 135(43), 15982-15985.
16. Chagarov, E., Sardashti, K., Kummel, A. C., Lee, Y. S., Haight, R., Gershon, T. S., "$Ag_2ZnSn(S,Se)_4$: A highly promising absorber for thin film photovoltaics" The Journal Of Chemical Physics 144, 104704 (2016).
17. Chantana, J., Kawano, Y., Nishimura, T., Mavlonov, A., Shen, Q., Yoshino, K., & Minemoto, T. (2021). Impact of Auger recombination on performance limitation of perovskite solar cell. *Solar Energy*, *217*, 342-353.
18. Chatterjee, S., & Pal, A. J. (2017). A solution approach to p-type Cu_2FeSnS_4 thin-films and pn-junction solar cells: role of electron selective materials on their performance. Solar Energy Materials and Solar Cells, 160, 233-240.
19. Chelvanathan, P., Hossain, M. I., & Amin, N. (2010). Performance analysis of copper–indium–gallium–diselenide (CIGS) solar cells with various buffer layers by SCAPS. Current applied physics, 10 (3), S387-S391.
20. Chen, J., & Park, N. G. (2019). Causes and solutions of recombination in perovskite solar cells. *Advanced Materials*, *31*(47), 1803019.
21. Chen, S., Gong, X. G., Walsh, A., & Wei, S. H. (2010). Defect physics of the kesterite thin-film solar cell absorber Cu_2ZnSnS_4. Applied Physics Letters, 96(2). (b)
22. Chen, S., Yang, J. H., Gong, X. G., Walsh, A., & Wei, S. H. (2010). Intrinsic point defects and complexes in the quaternary kesterite semiconductor Cu_2ZnSnS_4. Physical Review B—Condensed Matter and Materials Physics, 81(24), 245204. (a)

23. Chen, Z., Sun, K., Su, Z., Liu, F., D. Tang, H. Xiao, L. Shi, L. Jiang, X. Hao, Y. Lai, (2018). Solution-processed trigonal Cu_2BaSnS_4 thin-film solar cells, ACS Appl. Energy Mater. 1 3420–3427.

24. Chowdhury, M.S., Shahahmadi, S.A., Chelvanathan, P., Tiong, S.K. N. Amin, K.-A. Techato, N. Nuthammachot, T. Chowdhury, M. Suklueng, (2020). Effect of deep-level defect density of the absorber layer and n/i interface in perovskite solar cells by SCAPS-1D, Results Phys. 16 102839.

25. Courel, M., Arvizu, J.A.A., Gal´an, O.V., 2016. The role of buffer/kesterite interface recombination and minority carrier lifetime on kesterite thin film solar cells. Mater. Res. Express 3 (9), 95501.

26. Crovetto, A., Borsting, K., Nielsen, R., Hajijafarassar, A., Hansen, O., Seger, B., Vesborg, P. C. (2019). TaS_2 back contact improving oxide-converted Cu_2BaSnS_4 solar cells. ACS Applied Energy Materials, 3(1), 1190-1198.

27. Crovetto, A., Xing, Z., Fischer, M., Nielsen, R., Savory, C. N., Rindzevicius, T., & Vesborg, P. C. (2020). Experimental and first-principles spectroscopy of Cu_2SrSnS_4 and Cu_2BaSnS_4 photoabsorbers. ACS Applied Materials & Interfaces, 12(45), 50446-50454.

28. Cui, Y., Tong, J., Shao, H., Wang, G., & Pan, D. (2019). Novel $Cu_2BaSn(S, Se)_4$ thin film fabricated by solution process and its application in solar cells. Superlattices and Microstructures, 135, 106243.

29. Cullity, B D., Stock, S. R., (2014): Elements of X-Ray Diffraction, 3rd edition, Pearson New International Edition, 1-649.

30. Dasa, S., Frye, C., Muzykov, P.G., Mandal, K.C., 2012. Deposition and characterization of low-cost spray pyrolyzed Cu_2ZnSnS_4 (CZTS) thin-films for large-area high-efficiency heterojunction solar cells. ECS Trans. 45 (7), 153–161.

31. Dolgonos, A., Mason, T.O., Poeppelmeier, K.R., (2014): Direct optical band gap measurement in polycrystalline semiconductors: a critical look at the Tauc method, J. Solid State Chem., 240, 43–48.

32. Dsouza, N., Singh, A. K., Maurya, R., Kanakala, R., Madaka, R., Bandaru, N., Rath, J. K. (2023). Silicon surface passivation of industrial n-type CZ Si (111) by Al_2O_3 layers deposited by thermal ALD process for application in carrier selective contact solar cells. Journal of Materials Science: Materials in Electronics, 34(14), 1179.

33. Fernandes, P. A., Salomé, P. M. P., & Da Cunha, A. F. (2010). A study of ternary Cu_2SnS_3 and Cu_3SnS_4 thin films prepared by sulfurizing stacked metal precursors. Journal of Physics D: Applied Physics, 43(21), 215403.

34. Fu, J., Tian, Q., Zhou, Z., Kou, D., Meng, Y., Zhou, W., & Wu, S. (2016). Improving the performance of solution-processed $Cu_2ZnSn(S, Se)_4$ photovoltaic materials by Cd2+ substitution. Chemistry of Materials, 28(16), 5821-5828.

35. Garain, R., Basak, A., & Singh, U. P. (2021). Study of thickness and temperature dependence on the performance of SnS based solar cell by SCAPS-1D. Materials Today: Proceedings, 39, 1833-1837.

36. Ge, J., & Yan, Y. (2017). Synthesis and characterization of photoelectrochemical and photovoltaic Cu_2BaSnS_4 thin films and solar cells. Journal of Materials Chemistry C, 5(26), 6406-6419. (a)

37. Ge, J., Chu, J., Jiang, J., Yan, Y., & Yang, P. (2014). Characteristics of In-substituted CZTS thin film and bifacial solar cell. ACS applied materials & interfaces, 6(23), 21118-21130.

38. Ge, J., Koirala, P., Grice, C. R., Roland, P. J., Yu, Y., Tan, X., Yan, Y. (2017). Oxygenated CdS buffer layers enabling high open-circuit voltages in earth-abundant Cu_2BaSnS_4 thin-film solar cells. Advanced Energy Materials, 7(6), 1601803. (b)

39. Ge, J., Roland, P. J., Koirala, P., Meng, W., Young, J. L., Petersen, R., & Yan, Y. (2017). Employing overlayers to improve the performance of Cu2BaSnS4 thin film based photoelectrochemical water reduction devices. Chemistry of Materials, 29(3), 916-920. (c)

40. Ge, J., Yu, Y., & Yan, Y. (2016). Earth-Abundant Orthorhombic $BaCu_2Sn (Se_x S_{1-x})_4$ ($x \approx 0.83$) Thin Film for Solar Energy Conversion. ACS Energy Letters, 1(3), 583-588.

41. Gershon, T., Lee, Y. S., Antunez, P., Mankad, R., Singh, S., Bishop, D., & Haight, R. (2016). Photovoltaic materials and devices based on the alloyed kesterite absorber $(Ag_xCu_{1-x})_2ZnSnSe_4$. Advanced Energy Materials, 6(10), 1502468.

42. Gershon, T., Sardashti, K., Gunawan, O., Mankad, R., Singh, S., Lee, Y. S., Haight, R. (2016). Photovoltaic device with over 5% efficiency based on an n-type $Ag_2ZnSnSe_4$ absorber. Advanced Energy Materials, 6(22), 1601182.

43. Giraldo, S., Fonoll-Rubio, R., Z. Jehl Li-Kao, Y. Sanchez, L. Calvo-Barrio, V. Izquierdo-Roca, A. Perez-Rodríguez, E. Saucedo, (2021). Rear interface engineering of kesterite $Cu_2ZnSnSe_4$ solar cells by adding $CuGaSe_2$ thin layers, Prog. Photovolt.: Res. Appl. 29, 334–343.

44. Gokmen, T., Gunawan, O., Todorov, T. K., & Mitzi, D. B. (2013). Band tailing and efficiency limitation in kesterite solar cells. Applied Physics Letters, 103(10).

45. Goldstein, J., Newbury, D. E., Joy, D. C., Lyman, C. E., Echlin, P., Lifshin, E., Sawyer, L., Michael, J. R., (2003): Scanning Electron Microscopy and X-Ray Microanalysis: Third Edition, Kluwer academic/Plenum publishers, 1-675.
46. Guo, H., Li, Y., Guo, X., Yuan, N., & Ding, J. (2018). Effect of silicon doping on electrical and optical properties of stoichiometric Cu_2ZnSnS_4 solar cells. Physica B: Condensed Matter, 531, 9-15.
47. Guo, H., Ma, C., Chen, Z., Jia, X., Cang, Q., Yuan, N., & Ding, J. (2019). The fabrication of Cu_2BaSnS_4 thin film solar cells utilizing a maskant layer. Solar Energy, 181, 301-307.
48. Guo, Q., Ford, G. M., Yang, W.-C., Hages, C. J., Hillhouse, H. W., Agrawal, R., (2012). “Enhancing the performance of CZTSSe solar cells with Ge alloying” Sol. Energy Mater. Sol. Cells 105, 132.
49. Gupta, A. K. S., Farhad, S. F. U., Habib, M. S., Hossan, M. R., Hossain, K., Das, N. K., Amin, N. (2023). Characterizations of extrinsically doped CZTS thin films for solar cell absorbers fabricated by sol-gel spin coating method. Applied Surface Science Advances, 13, 100352.
50. Gupta, G.K., Dixit, A., (2018). Theoretical studies of single and tandem $Cu_2ZnSn(S/Se)_4$ junction solar cells for enhanced efficiency, Opt. Mater. 82, 11–20.
51. Gupta, I., & Mohanty, B. C. (2019). Eliminating secondary phases: Understanding kesterite phase evolution of Cu_2ZnSnS_4 thin films grown from ethanol based solutions with high photosensitivity. Solar Energy, 181, 214-221.
52. Hages, C. J., Koeper, M. J., Agrawal, R., (2016). “Optoelectronic and material properties of nanocrystal-based CZTSe absorbers with Ag-alloying” Sol. Energy Mater. Sol. Cells 145, 342.
53. Haight, R., Barkhouse, A., Gunawan, O., Shin, B., Copel, M., Hopstaken, M., Mitzi, D.B., (2011). Band alignment at the $Cu_2ZnSn(S_xSe_{1-x})_4$/CdS interface, Appl. Phys. Lett. 98, 253502.
54. Hong, F., Lin, W., Meng, W., & Yan, Y. (2016). Trigonal Cu 2-II-Sn-VI 4 (II= Ba, Sr and VI= S, Se) quaternary compounds for earth-abundant photovoltaics. Physical Chemistry Chemical Physics, 18(6), 4828-4834.
55. Hong, T., Chen, F., & Xia, C. (2015). Barium carbonate nanoparticle as high temperature oxygen reduction catalyst for solid oxide fuel cell. Electrochemistry Communications, 51, 93-97.

56. Houimi, A., Gezgin, S.Y., Mercimek, B., Kılıç, H.S, (2021). Numerical analysis of CZTS/n-Si solar cells using SCAPS-1D. A comparative study between experimental and calculated outputs, Opt. Mater. 121, 111544.

57. Ichimura, M., Song, Y., (2011). Band alignment at the Cu_2O/ZnO heterojunction. Jpn. J. Appl. Phys. 50 (5R), 051002.

58. Islam, M. M., Halim, M. A., Sakurai, T., Sakai, N., Kato, T., Sugimoto, H., & Akimoto, K. (2015). Determination of deep-level defects in $Cu_2ZnSn(S, Se)_4$ thin-films using photocapacitance method. Applied Physics Letters, 106(24).

59. Johnson, Melissa C., Cody Wrasman, Xin Zhang, Michael Manno, C. Leighton, and Eray S. Aydil. (2015). Self-regulation of Cu/Sn ratio in the synthesis of Cu_2ZnSnS_4 films. Chemistry of Materials 27, 7, 2507-2514.

60. Kangsabanik, M., Sinha, S., Maity, P., Chowdhury, J., Manna, S., & Gayen, R. N. (2025). Partial Substitution of Copper with Silver in Cu_2ZnSnS_4: An Efficient Strategy to Boost the Performance of Self-Powered Broadband Photodetectors in Superstrate Configuration. ACS Applied Materials & Interfaces.

61. Kassim, S.T., Hadi, H.A., Ismail, R.A., (2010). Fabrication and characterization of high photosensitivity CuS/porous silicon heterojunction photodetector, Optik 221, 165339.

62. Kaur, K., Kumar, N., Kumar, M., (2017). Strategic review of interface carrier recombination in earth abundant Cu-Zn-Sn-S-Se solar cells: current challenges and future prospects. J. Mater. Chem. A 5 (7), 3069–3090.

63. Kerr, M. J., & Cuevas, A. (2002). General parameterization of Auger recombination in crystalline silicon. Journal of Applied Physics, *91*(4), 2473-2480.

64. Khadka, D. B., Kim, J. H., "Band Gap Engineering of Alloyed Cu_2 $ZnGe_xSn_{1-x}Q_4$ (Q = S,Se) Films for Solar Cell" J. Phys. Chem. C, 119, 1706 (2015).

65. Khattak, Y. H., Baig, F., Toura, H., Beg, S., & Soucase, B. M. (2019). Efficiency enhancement of Cu_2BaSnS $_4$ experimental thin-film solar cell by device modeling. Journal of Materials Science, 54, 14787-14796.

66. Khattak, Y.H., Baig, F., Soucase, B.M., Beg, S., (2018). Efficiency enhancement of Cu_2BaSnS_4 thin film solar cell, Mater. Focus 7, 758–765.

67. Kim, J., Lee, J. Y., Jang, J., He, M., Jeong, W. L., Suryawanshi, M. P., & Kim, J. H. (2017). Influence of selenium doping on the properties of $Cu_2Sn(S_xSe_{1-x})_3$ thin-film solar cells fabricated by sputtering. Solar Energy Materials and Solar Cells, 172, 154-159.

68. Kim, S., Kim, K. M., Tampo, H., Shibata, H., Matsubara, K., Niki, S., (2016). Ge-incorporated Cu2ZnSnSe4 thin-film solar cells with efficiency greaterthan10%", Sol. Energy Mater. Sol. Cells 144, 488.

69. Kim, Y., Hempel, H., Levcenco, S., Euvrard, J., Bergmann, E., Gunawan, O., & Mitzi, D. B. (2021). Optoelectronic property comparison for isostructural $Cu_2BaGeSe_4$ and Cu_2 $BaSnS_4$ solar absorbers. Journal of Materials Chemistry A, *9* (41), 23619-23630.

70. Kobayashi, T., Jimbo, K., Tsuchida, K., Shinoda, S., Oyanagi, T., & Katagiri, H. (2005). Investigation of Cu_2ZnSnS_4-based thin film solar cells using abundant materials. *Japanese Journal of Applied Physics*, *44*(1S), 783.

71. Kumar, M. S., Madhusudanan, S. P., & Batabyal, S. K. (2018). Substitution of Zn in Earth-Abundant Cu_2ZnSn (S, Se)$_4$ based thin film solar cells–A status review. Solar Energy Materials and Solar Cells, 185, 287-299.

72. Kumar, M. S., Mohanta, K., & Batabyal, S. K. (2017). Solution processed Cu_2CdSnS_4 as a low-cost inorganic hole transport material for polymer solar cells. Solar Energy Materials and Solar Cells, 161, 157-161.

73. Le Formal, F., Tetreault, N., Cornuz, M., Moehl, T., Gratzel, M., & Sivula, K. (2011). Passivating surface states on water splitting hematite photoanodes with alumina overlayers. Chemical Science, 2(4), 737-743.

74. Levcenko, S., Teymur, B., Mitzi, D. B., & Unold, T. (2021). Photoluminescence study of solution-deposited Cu2BaSnS4 thin films. APL Materials, 9(11).

75. Li, J., Wang, D., Li, X., Zeng, Y., "Cation Substitution in Earth-Abundant Kesterite Photovoltaic Materials" Adv. Sci. 5, 1700744 (2018).

76. Liang, X., Wang, P., Huang, B., Zhang, Q., Wang, Z., Liu, Y., & Dai, Y. (2018). Effects of Ag Incorporation on the Band Structures and Conductivity Types of $(Cu_{1-x}Ag_x)_2ZnSnS_4$ Solid Solutions. Chem Photo Chem, 2(9), 811-817.

77. Lie, S., Tan, J. M. R., Li, W., Leow, S. W., Tay, Y. F., Bishop, D. M., Wong, L. H. (2018). Reducing the interfacial defect density of CZTSSe solar cells by Mn substitution. Journal of Materials Chemistry A, 6(4), 1540-1550.

78. Liu, F., Huang, J., Sun, K., Yan, C., Shen, Y., Jongsung, P., Pu, A., Zhou, F., Liu, X., Stride, J.A., Green, M.A., Hao, X., (2017). Beyond 8% ultrathin kesterite Cu_2ZnSnS_4 solar cells by interface reaction route controlling and self-organized nanopattern at the back contact. NPG Asia Mater. 9, 401.

79. Liu, X., Feng, Y., Cui, H., Liu, F., Hao, X., Conibeer, G., & Green, M. (2016). The current status and future prospects of kesterite solar cells: a brief review. Progress in Photovoltaics: Research and Applications, 24(6), 879-898.

80. Liu, X., Guo, J., Hao, R., Zhao, Q., Chang, F., Wang, L., & Gu, K. (2019). Cliff-like conduction band offset at CdS/Cu_2ZnSnS_4 heterojunction prepared by sputtering CuSn alloy target using different stacking order. Solar Energy, *183*, 285-292.

81. Lu, X., Xu, B., Qin, X., Chen, Y.e., Yang, P., Chu, J., Sun, L., (2020). Modification of back contact in Cu2ZnSnS4 solar cell by inserting Al-doped ZnO intermediate layer. ACS Appl. Mater. Interfaces 12 (52), 58060–58071.

82. Lundberg, O., Bodegard, M., Malmström, J., & Stolt, L. (2003). Influence of the Cu (In, Ga)Se_2 thickness and Ga grading on solar cell performance. Progress in Photovoltaics: Research and Applications, 11(2), 77-88.

83. Luo, H., Chen, J., Zhang, X., Wang, S., Gu, H., Wang, W., & Li, H. (2020). Controlled synthesis of high efficiency Cu_2BaSnS_4 solar cells via a solution processed method. Materials Letters, 270, 127750.

84. Luo, H., Zhang, Y., & Li, H. (2021). Effect of MoS_2 interlayer on performances of copper-barium-tin-sulfur thin film solar cells via theoretical simulation. Solar Energy, 223, 384-397.

85. Malani, R., Pansuriya, T., & Kheraj, V. (2022). A study on influence of potential defects and optimization of device structure for $CuSbS_2$ based thin film solar cell using SCAPS–1D simulator. Optical Materials, 133, 112910.

86. Mandelkorn, J., Lamneck, J.H., (1975). Advances in the theory and application of BSF cells. In: Record of 11th Photovoltaic Specialists Conference, 75CH0948-OED.

87. Mazumder, S., Senthilkumar, K., (2022). Device study and optimisation of CZTS/ZnS based solar cell with CuI hole transport layer for different conduction band offset, Sol. Energy 237, 414–431.

88. McCandless, B. E., Bishop, D., & Lloyd, M. (2019). Majority carrier properties of single crystal Cu_{2-x} $ZnSnSe_4$ with varying copper composition. physica status solidi (b), 256(11), 1900180.

89. McCarthy, C. L., & Brutchey, R. L. (2018). Solution Deposited $Cu_2BaSnS_{4-x}Se_x$ from a Thiol–Amine Solvent Mixture. Chemistry of Materials, 30(2), 304-308.

90. Meyer, B.K., Polity, A., Reppin, D., Becker, M., Hering, P., Klar, P.J., Sander, T.h., Reindl, C., Benz, J., Eickhoff, M., Heiliger, C., Heinemann, M., Bl¨asing, J., Krost, A.,

Shokovets, S., Müller, C., Ronning, C., (2012). Binary copper oxide semiconductors: from materials towards devices. Phys. Status Solidi B 249 (8), 1487–1509.

91. Miller, D. W., Warren, C. W., Gunawan, O., Gokmen, T., Mitzi, D. B., & Cohen, J. D. (2012). Electronically active defects in the Cu_2ZnSn (Se, $S)_4$ alloys as revealed by transient photocapacitance spectroscopy. *Applied Physics Letters*, *101*(14).
92. Miller, D. W., Warren, C. W., Gunawan, O., Gokmen, T., Mitzi, D. B., & Cohen, J. D. (2012). Electronically active defects in the Cu_2ZnSn (Se, $S)_4$ alloys as revealed by transient photocapacitance spectroscopy. Applied Physics Letters, 101(14).
93. Minbashi, M., Omrani, M.K., Memarian, N., Kim, D. H., (2017). Comparison of theoretical and experimental results for band-gap-graded CZTSSe solar cell, Curr. Appl. Phys. 17, 1238–1243.
94. Minemoto, T., & Murata, M. (2015). Theoretical analysis on effect of band offsets in perovskite solar cells. Solar Energy Materials and Solar Cells, *133*, 8-14.
95. Minemoto, T., Matsui, T., Takakura, H., Hamakawa, Y., Negami, T. Y. Hashimoto, T. Uenoyama, M. Kitagawa, (2001). Theoretical analysis of the effect of conduction band offset of window/CIS layers on performance of CIS solar cells using device simulation, Sol. Energy Mater. Sol. Cells 67, 83–88.
96. Mitzi, D. B., Gunawan, O., Todorov, T. K., & Barkhouse, D. A. R. (2013). Prospects and performance limitations for Cu–Zn–Sn–S–Se photovoltaic technology. Philosophical Transactions of the Royal Society A: Mathematical, Physical and Engineering Sciences, 371(1996), 20110432.
97. Mitzi, D. B., Gunawan, O., Todorov, T. K., Wang, K., & Guha, S. (2011). The path towards a high-performance solution-processed kesterite solar cell. Solar Energy Materials and Solar Cells, 95(6), 1421-1436.
98. Mitzi, D.B., Gunawan, O., Todorov, T.K., Wang, K., Guha, S., (2011). The path towards a high-performance solution-processed kesterite solar cell. Sol. Energy Mater. Sol. Cells 95 (6), 1421–1436.
99. Mohanty, B.C., Jyoti, (2021). Improving performance of Cu_2ZnSnS_4 solar cell via back contact interface engineering, Sol. Energy 230, 986–995.
100. Mostefaoui, M., Mazari, H., Khelifi, S., Bouraiou, A., Dabou, R., (2015). Simulation of high efficiency CIGS solar cells with SCAPS-1D software. Energy Procedia 74, 736–744.
101. Moustafa, M., Al Zoubi, T., & Yasin, S. (2022). Exploration of CZTS-based solar using the ZrS_2 as a novel buffer layer by SCAPS simulation. Optical Materials, *124*, 112001.

102. Nagoya, A., Asahi, R., Wahl, R., & Kresse, G. (2010). Defect formation and phase stability of Cu 2 ZnSnS 4 photovoltaic material. *Physical Review B—Condensed Matter and Materials Physics*, *81*(11), 113202.

103. Neuschitzer, M., Sanchez, Y., López-Marino, S., Xie, H., Fairbrother, A., Placidi, M., & Saucedo, E. (2015). Optimization of CdS buffer layer for high-performance $Cu_2ZnSnSe_4$ solar cells and the effects of light soaking: elimination of crossover and red kink. Progress in Photovoltaics: Research and Applications, *23*(11), 1660-1667.

104. Nguyen, T. H., Kawaguchi, T., Chantana, J., Minemoto, T., Harada, T., Nakanishi, S., & Ikeda, S. (2018). Structural and solar cell properties of a Ag-containing Cu_2ZnSnS_4 thin film derived from spray pyrolysis. ACS applied materials & interfaces, 10(6), 5455-5463.

105. Olgar, M. A., Erkan, S., & Zan, R. (2023). Dependence of CZTS thin film properties and photovoltaic performance on heating rate and sulfurization time. Journal of Alloys and Compounds, 963, 171283.

106. Omrani, M.K Minbashi, M.,, Memarian, N., Kim, D. H., (2018). Improve the performance of CZTSSe solar cells by applying a SnS BSF layer, Solid-State Electron. 141, 50–57.

107. Padhy, S., Mannu, R., & Singh, U. P. (2021). Graded band gap structure of kesterite material using bilayer of CZTS and CZTSe for enhanced performance: A numerical approach. Solar Energy, 216, 601-609.

108. Pandey, K., & Mohanty, B. C. (2022). Facile single step synthesis of Cu_2ZnSnS_4 thin films by sputtering from a single target and their electrical characterization. Journal of Alloys and Compounds, 925, 166657.

109. Park, J., Huang, J., Sun, K., Ouyang, Z., Liu, F., Yan, C., Sun, H., Pu, A., Green, M., Hao, X., (2018). The effect of thermal evaporated MoO3 intermediate layer as primary back contact for kesterite Cu_2ZnSnS_4 solar cells. Thin Solid Films 648, 39–45.

110. Patil, S. S., Khot, K. V., Mali, S. S., Hong, C. K., & Bhosale, P. N. (2020). Investigating the Role of Selenium-Ion Concentration on Optoelectronic Properties of the Cu_2ZnSn $(S_{1-x}$ $Se_x)_4$ Thin Films. Industrial & Engineering Chemistry Research, 59(23), 10868-10881.

111. Polizzotti, A., Repins, I. L., Noufi, R., Wei, S. H., & Mitzi, D. B. (2013). The state and future prospects of kesterite photovoltaics. Energy & Environmental Science, *6* (11), 3171-3182.

112. Raju, C., Falmbigl, M., Rogl, P., Yan, X., Bauer, E., Horky, J., & Chandra Mallik, R. (2013). Thermoelectric properties of chalcogenide based $Cu_{2+x}ZnSn_{1-x}Se_4$. Aip Advances, 3(3).

113. Ramanujam, J., Bishop, D. M., Todorov, T. K., Gunawan, O., Rath, J., Nekovei, R., & Romeo, A. (2020). Flexible CIGS, CdTe and a-Si: H based thin film solar cells: A review. Progress in Materials Science, 110, 100619.

114. Redinger, A., Berg, D. M., Dale, P. J., & Siebentritt, S. (2011). The consequences of kesterite equilibria for efficient solar cells. Journal of the American Chemical Society, 133(10), 3320-3323.

115. Ren, Y., Ross, N., Larsen, J. K., Rudisch, K., Scragg, J. J., & Platzer-Bjorkman, C. (2017). Evolution of Cu_2ZnSnS_4 during non-equilibrium annealing with quasi-in situ monitoring of sulfur partial pressure. Chemistry of Materials, 29(8), 3713-3722.

116. Roos, V., (1978). A simple theory of back surface field (BSF) solar cells. J. Appl. Phys. 49 (6), 3503–3511.

117. S. Lee, E.S. Lee, T.Y. Kim, J.S. Cho, Y.J. Eo, J.H. Yun, A. Cho, (2015). Effect of annealing treatment on CdS/CIGS thin film solar cells depending on different CdS deposition temperatures, Sol. Energy Mater. Sol. Cells 141, 299–308.

118. Sravani, L., Routray, S., Courel, M., & Pradhan, K. P. (2021). Loss mechanisms in CZTS and CZTSe Kesterite thin-film solar cells: Understanding the complexity of defect density. Solar Energy, 227, 56-66.

119. Scaffidi, R., Brammertz, G., Wang, Y., Zaman, A. U., Sasikumar, K., de Wild, J., & Vermang, B. (2023). A study of bandgap-graded CZTGSe kesterite thin films for solar cell applications. Energy Advances, 2(10), 1626-1633.

120. Schnabel, T., Abzieher, T., Friedlmeier, T. M., & Ahlswede, E. (2015). Solution-based preparation of Cu_2ZnSn (S, Se)$_4$ for solar cells—comparison of $SnSe_2$ and elemental Se as chalcogen source. IEEE Journal of Photovoltaics, 5(2), 670-675.

121. Scragg, J.J., Ericson, T., Kubart, T., Edoff, M., Platzer-Bj¨orkman, C., (2011). Chemical Insights into the Instability of Cu_2ZnSnS_4 Films during Annealing. Chem. Mater. 23 (20), 4625–4633.

122. Scragg, J.J., Kubart, T., Watjen, J.T., Ericson, T., Linnarsson, M.K., Platzer-Bjorkman, C., (2013). Effects of back contact instability on Cu_2ZnSnS_4 devices and processes. Chem. Mater. 25 (15), 3162–3171.

123. Sharma, A., Sahoo, P., Singha, A., Padhan, S., & Thangavel, R. (2021). Visible-light induced photosplitting of water using solution-processed Cu_2BaSnS_4 photoelectrodes

and a tandem approach for development of Pt-free photoelectrochemical cell. Materials Science in Semiconductor Processing, 121, 105433.

124. Shin, B., Bojarczuk, N.A., Guha, S., (2013). On the kinetics of $MoSe_2$ interfacial layer formation in chalcogen-based thin film solar cells with a molybdenum back contact. Appl. Phys. Lett. 102 (9), 091907.
125. Shin, D., Ngaboyamahina, E., Zhou, Y., Glass, J. T., & Mitzi, D. B. (2016). Synthesis and characterization of an earth-abundant $Cu_2BaSn(S,Se)_4$ chalcogenide for photoelectrochemical cell application. The journal of physical chemistry letters, 7(22), 4554-4561.
126. Shin, D., Saparov, B., Zhu, T., Huhn, W. P., Blum, V., & Mitzi, D. B. (2016). $BaCu_2Sn(S, Se)_4$: earth-abundant chalcogenides for thin-film photovoltaics. Chemistry of Materials, 28(13), 4771-4780.
127. Shin, D., Zhu, T., Huang, X., Gunawan, O., Blum, V., & Mitzi, D. B. (2017). Earth-abundant chalcogenide photovoltaic devices with over 5% efficiency based on a $Cu_2BaSn (S, Se)_4$ absorber. Advanced Materials, 29(24), 1606945.
128. Simmons, J. G., & Taylor, G. W. (1971). Nonequilibrium steady-state statistics and associated effects for insulators and semiconductors containing an arbitrary distribution of traps. *Physical Review B*, *4*(2), 502.
129. Song, J., Teymur, B., Zhou, Y., Ngaboyamahina, E., & Mitzi, D. B. (2021). Porous $Cu_2BaSn(S, Se)_4$ film as a photocathode using non-toxic solvent and a ball-milling approach. ACS Applied Energy Materials, 4(1), 81-87.
130. Song, Y., Sun, H., Yao, B., Li, Y., Ding, Z., Qin, W., & Pan, D. (2020). Modulation of field-effect passivation at the back electrode interface enabling efficient kesterite-type $Cu_2ZnSn(S, Se)_4$ thin-film solar cells. ACS Applied Materials & Interfaces, 12(34), 38163-38174.
131. Sravani, L., Routray, S., Courel, M., Pradhan, K.P., (2021). Loss mechanisms in CZTS and CZTSe kesterite thin-film solar cells: understanding the complexity of defect density, Sol. Energy 227, 56–66.
132. Su, Z., Tan, J. M. R., Li, X., Zeng, X., Batabyal, S. K., & Wong, L. H. (2015). Cation substitution of solution-processed Cu_2ZnSnS_4 thin film solar cell with over 9% efficiency. Advanced Energy Materials, 5(19), 1500682.
133. Swami, S. K., Chaturvedi, N., Kumar, A., Chander, N., Dutta, V., Kumar, D. K., & Upadhyaya, H. M. (2014). Spray deposited copper zinc tin sulphide (Cu_2ZnSnS_4) film as

a counter electrode in dye sensitized solar cells. Physical Chemistry Chemical Physics, 16(43), 23993-23999.

134. Szymanski, H. A., (1967): Raman spectroscopy: Theory and practice, Plenum press New York, 1-251.
135. Taberna, P. L., Simon, P., & Fauvarque, J. F. (2003). Electrochemical characteristics and impedance spectroscopy studies of carbon-carbon supercapacitors. Journal of the Electrochemical Society, 150(3), A292.
136. Tanaka, K., Oonuki, M., Moritake, N., & Uchiki, H. (2009). Cu_2ZnSnS_4 thin film solar cells prepared by non-vacuum processing. Solar Energy Materials and Solar Cells, *93* (5), 583-587.
137. Teske, C., (1976). "Preparation and crystal structure of Cu_2SrSnS_4" Z. Anorg. Allg. Chem, 419, 67.
138. Teymur, B., Choubrac, L., Hempel, H., Gunawan, O., Unold, T., & Mitzi, D. B. (2022). Influence of copper composition on $Cu_2BaSn(S, Se)_4$ solution-deposited films and photovoltaic devices with over 5% efficiency. ACS Applied Energy Materials, 5(9), 10645-10656. b
139. Teymur, B., Kim, Y., Huang, J., Sun, K., Hao, X., & Mitzi, D. B. (2022). Top stack optimization for $Cu_2BaSn(S, Se)_4$ photovoltaic cell leads to improved device power conversion efficiency beyond 6%. Advanced Energy Materials, 12(40), 2201602. a
140. Teymur, B., Levcenco, S., Hempel, H., Bergmann, E., Márquez, J. A., Choubrac, L., Mitzi, D. B. (2021). Optoelectronic and material properties of solution-processed Earth-abundant Cu_2BaSn (S, Se)$_4$ films for solar cell applications. Nano Energy, 80, 105556.
141. Teymur, B., Zhou, Y., Ngaboyamahina, E., Glass, J. T., & Mitzi, D. B. (2018). Solution-processed earth-abundant $Cu_2BaSn(S, Se)_4$ solar absorber using a low-toxicity solvent. Chemistry of Materials, 30(17), 6116-6123.
142. Tiwari, K. J., Chetty, R., Mallik, R. C., & Malar, P. (2017). Solid state synthesis and e-beam evaporation growth of $Cu_2ZnSnSe_4$ for solar energy absorber applications. Solar Energy, 153, 173-180. a
143. Tiwari, K. J., Prem Kumar, D. S., Mallik, R. C., & Malar, P. (2017). Ball mill synthesis of bulk quaternary $Cu_2ZnSnSe_4$ and thermoelectric studies. Journal of Electronic Materials, 46, 30-39. B
144. Toby, B. H., & Von Dreele, R. B. (2013). GSAS-II: the genesis of a modern open-source all purpose crystallography software package, J. Appl. Crystallography, 46 (2), 544-549.

145. Todorov, T. K., Reuter, K. B., & Mitzi, D. B. (2010). High‐efficiency solar cell with earth‐abundant liquid‐processed absorber. Advanced materials, *22*(20), E156.

146. Todorov, T., Hillhouse, H. W., Aazou, S., Sekkat, Z., Vigil-Galán, O., Deshmukh, S. D., & Dale, P. J. (2020). Solution-based synthesis of kesterite thin film semiconductors. Journal of Physics: Energy, 2(1), 012003.

147. Tong, Z., Yan, C., Su, Z., Zeng, F., Yang, J., Li, Y., Liu, F. (2014). Effects of potassium doping on solution processed kesterite Cu_2ZnSnS_4 thin film solar cells. Applied Physics Letters, 105(22).

148. Tumbul, A., Aslan, F., Goktaş, A., & Mutlu, I. H. (2019): All solution processed superstrate type Cu_2ZnSnS_4 (CZTS) thin film solar cell: effect of absorber layer thickness. Journal of Alloys and Compounds, 781, 280-288.

149. Van der Pauw, L.J., (1958): A method of measuring the resistivity and Hall coefficient on lamellae of arbitrary shape, Philips Tech. Rev. 20 (8) 220–224 (b)

150. Van der Pauw, L.J., (1958): A Method of Measuring Specific Resistivity and Hall Effect of Discs of Arbitrary Shape, Philips Res. Rep. 13 (1) 1–9. (a)

151. Wallace, S. K., Mitzi, D. B., & Walsh, A. (2017). The steady rise of kesterite solar cells. ACS Energy Letters, 2(4), 776-779.

152. Walsh, A., Chen, S., Wei, S. H., & Gong, X. G. (2012). Kesterite thin‐film solar cells: Advances in materials modelling of Cu_2ZnSnS_4. *Advanced Energy Materials*, *2*(4), 400-409.

153. Wanda, M.D., Ouedraogo, S., Tchoffo, F., Zougmore, F., Ndjaka, J.M.B., (2016). Numerical investigations and analysis of Cu_2ZnSnS_4 based solar cells by SCAPS-1D. Int. J. Photoenergy, 2152018.

154. Wang, C., Chen, S., Yang, J. H., Lang, L., Xiang, H. J., Gong, X. G., ... & Wei, S. H. (2014). Design of I2–II–IV–VI4 semiconductors through element substitution: the thermodynamic stability limit and chemical trend. Chemistry of Materials, 26(11), 3411-3417. (b)

155. Wang, H., Zhang, L., Chen, Z., Hu, J., Li, S., Wang, Z., Wang, X. (2014). Semiconductor heterojunction photocatalysts: design, construction, and photocatalytic performances. Chemical Society Reviews, 43(15), 5234-5244.

156. Wang, S., Zhang, J., Gharbi, O., Vivier, V., Gao, M., & Orazem, M. E., (2021): Electrochemical impedance spectroscopy, Nature Reviews Methods Primers volume 1, Article number: 41.

157. Wang, W., Winkler, M. T., Gunawan, O., Gokmen, T., Todorov, T. K., Zhu, Y., & Mitzi, D. B. (2014). Device characteristics of CZTSSe thin-film solar cells with 12.6% efficiency. *Advanced energy materials*, *4*(7). (a)

158. Wei, Y., Zhou, K., Meng, X., Sun, X., Ma, Z., Li, Z., & Zhuang, D. (2024). Improving the performance of solution-based CZTSSe absorber by selenization annealing with selenium powder in argon. Journal of Alloys and Compounds, 976, 173123.

159. Wei, Y., Zhuang, D., Zhao, M., Gong, Q., Sun, R., Ren, G., & Wei, J. (2019). An investigation on the relationship between open circuit voltage and grain size for CZTSSe thin film solar cells fabricated by selenization of sputtered precursors. Journal of alloys and compounds, 773, 689-697.

160. Werner, M., Keller, D., Haass, S. G., Gretener, C., Bissig, B., Fuchs, P., & Tiwari, A. N. (2015). Enhanced carrier collection from CdS passivated grains in solution-processed $Cu_2ZnSn(S, Se)_4$ solar cells. ACS applied materials & interfaces, 7(22), 12141-12146.

161. Werner, M., Sutter-Fella, C. M., Romanyuk, Y. E., & Tiwari, A. N. (2015). 8.3% efficient $Cu_2ZnSn(S, Se)_4$ solar cells processed from sodium-containing solution precursors in a closed reactor. Thin Solid Films, 582, 308-312.

162. Wilhelm, H., Schock, H.-W., Scheer, R., (2011). Interface recombination in heterojunction solar cells: influence of buffer layer thickness, J. Appl. Phys. 109.

163. Wong, L.M., Chiam, S.Y., Huang, J.Q., Wang, S.J., Pan, J.S., Chim, W.K., (2010). Growth of Cu_2O on Ga-doped ZnO and their interface energy alignment for thin film solar cells. J. Appl. Phys. 108.

164. Xiao, Z. Y., Li, Y. F., Yao, B., Deng, R., Ding, Z. H., Wu, T., Zhao, H. F. (2013). Bandgap engineering of $Cu_2Cd_xZn_{1-x}SnS_4$ alloy for photovoltaic applications: a complementary experimental and first-principles study. Journal of Applied Physics, 114(18).

165. Xiao, Z., Meng, W., Li, J. V., & Yan, Y. (2017). Distant-atom mutation for better earth-abundant light absorbers: a case study of $Cu_2BaSnSe_4$. ACS Energy Letters, 2(1), 29-35.

166. Xie, M., Zhuang, D. M., Zhao, M., Li, B. J., & Song, J. (2013): The influence of sulfurization time and H_2S concentration on the properties of Cu_2ZnSnS_4 thin films. Advanced Materials Research, 818, 3-8.

167. Yadav, R. K., Pawar, P. S., Nandi, R., Neerugatti, K. E., Kim, Y. T., Cho, J. Y., & Heo, J. (2022). A qualitative study of SnSe thin film solar cells using SCAPS 1D and comparison with experimental results: a pathway towards 22.69% efficiency. Solar Energy Materials and Solar Cells, 2*44*, 111835.

168. Yafang, Q., Qingwen, T., Yuena, M., Dongxing, K., Zhengji, Z., Wenhui, Z., & Sixin, W. (2017). Elemental Precursor Solution Processed $(Cu_{1-x}Ag_x)_2ZnSn(S,Se)_4$ Photovoltaic Devices with over 10% Efficiency.

169. Yan, C., Huang, J., Sun, K., Johnston, S., Zhang, Y., Sun, H., Pu, A., He, M., Liu, F., Eder, K., Yang, L., Cairney, J.M., Daukes, N.J.E., Hameiri, Z., Stride, J.A., Chen, S., Green, M.A., Hao, X., (2018). Cu_2ZnSnS_4 solar cells with over 10% power conversion efficiency enabled by heterojunction heat treatment. Nature Energy 3, 764–772.

170. Yan, C., Sun, K., Huang, J., Johnston, S., Liu, F., Veettil, B. P., & Hao, X. (2017). Beyond 11% efficient sulfide kesterite $Cu_2Zn_xCd_{1-x}SnS_4$ solar cell: effects of cadmium alloying. *ACS Energy Letters*, *2*(4), 930-936.

171. Yanchun, Y., Xiaojiao, K., Lijian, H., & Daocheng, P. (2016). Tuning the Band Gap of $Cu_2ZnSn\ (S, Se)_4$ Thin Films via Lithium Alloying.

172. Yu, W., Li, F., Wang, H., Alarousu, E., Chen, Y., Lin, B., Wang, L., Hedhili, M.N., Li, Y., Wu, K., Wang, X., Mohammed, O.F., Wu, T., (2016). Ultrathin Cu_2O as an efficient inorganic hole transporting material for perovskite solar cells. Nanoscale 8 (11), 6173–6179.

173. Zaki, M. Y., Sava, F., Simandan, I. D., Stavarache, I., Velea, A., & Pintilie, L. (2024). Optimization of CZTSe Thin Films Using Sequential Annealing in Selenium and Tin–Selenium Environments. Inorganic Chemistry, 64(1), 1-10.

174. Zhang, S., Fan, L., Yao, D., Wu, J., Guo, H., Wang, H., Zhang, Y., (2021). Band alignment tuning at Mo/CZTS back contact interface through surface oxidation states control of Mo substrate, Sol. Energy Mater. Sol. Cells 229, 111141.

175. Zhang, X., Shen, J. X., Wang, W., & Van de Walle, C. G. (2018). First-principles analysis of radiative recombination in lead-halide perovskites. ACS Energy Letters, *3*(10), 2329-2334.

176. Zhang, Y., Song, Q., Wu, L., Su, X., Hu, X., Wang, X., Wang, S. (2024). Effects of the Annealing Conditions on the Properties of $Cu_2ZnGeSe_4$ Thin Film Solar Cells. Journal of Inorganic and Organometallic Polymers and Materials, 1-13.

177. Zhao, Y., Han, X., Xu, B., Li, W., Li, J., Li, J., Li, J. (2017). Enhancing open-circuit voltage of solution-processed $Cu_2ZnSn(S, Se)_4$ solar cells with Ag substitution. IEEE Journal of Photovoltaics, 7(3), 874-881.

178. Zhou, J., Xu, X., Wu, H., Wang, J., Lou, L., Yin, K., Meng, Q. (2023). Control of the phase evolution of kesterite by tuning of the selenium partial pressure for solar cells with 13.8% certified efficiency. Nature Energy, 8(5), 526-535.

179. Ziabari, A. A., Zindanlou, N. M., Hassanzadeh, J., Golshahi, S., & Khatibani, A. B. (2020). Fabrication and study of single-phase high-hole-mobility CZTS thin films for PV solar cell applications: Influence of stabilizer and thickness. Journal of Alloys and Compounds, 842, 155741.

180. Zuo, C., Ding, L., (2015). Solution-processed Cu_2O and CuO as hole transport materials for efficient perovskite solar cells. Small 11 (41), 5528–5532.

Jyoti Thesis_BCM

P Singh
24/09/25
(Prabal Pratap Singh Bhadauria)

ORIGINALITY REPORT

15%	7%	13%	5%
SIMILARITY INDEX	INTERNET SOURCES	PUBLICATIONS	STUDENT PAPERS

PRIMARY SOURCES

1	Submitted to Thapar University, Patiala Student Paper	3%
2	Kaushlendra Pandey, Bhaskar Chandra Mohanty. "Facile single step synthesis of Cu2ZnSnS4 thin films by sputtering from a single target and their electrical characterization", Journal of Alloys and Compounds, 2022 Publication	1%
3	Indu Gupta, Kunal J. Tiwari, P. Malar, Bhaskar Chandra Mohanty. "Evaluating the role of precursor concentration in facile conformal coating of sub-micrometer thick Cu2ZnSnS4 films using non-toxic ethanol based solutions", Applied Surface Science, 2019 Publication	1%
4	Meenakshi Sahu, Vasudeva Reddy Minnam Reddy, Chinho Park, Pratibha Sharma. "Review article on the lattice defect and interface loss mechanisms in kesterite materials and their impact on solar cell performance", Solar Energy, 2021 Publication	<1%
5	Md. Sohel Rana, Md. Mazharul Islam, M. Julkarnain. "Enhancement in efficiency of CZTS solar cell by using CZTSe BSF layer", Solar Energy, 2021 Publication	<1%